NTNU – Trondheim
Norwegian University of
Science and Technology

An analysis of tensile strength, fracture initiation and propagation in anisotropic rock (gas shale) using Brazilian tests equipped with high speed video and acoustic emission

Nathaniel Denis John
Simpson

Petroleum Engineering
Submission date: July 2013
Supervisor: Rune Martin Holt, IPT
Co-supervisor: Ida Lykke Fabricius, Technical University of Denmark (DTU)

Norwegian University of Science and Technology
Department of Petroleum Engineering and Applied Geophysics

Abstract

This study attempts to further our knowledge of fracture behaviour by establishing an experimental system that links tensile strength, fracture initiation and propagation of an anisotropic rock (Mancos Shale) using an integrated Brazilian Test Setup equipped with Acoustic Emission and High Speed Video. The unique experimental configuration was applied to an anisotropic gas shale (Mancos Shale) in addition to other petroleum related reservoir rocks (such as sandstone and chalk). The variation in tensile strength, fracture initiation location, propagation time and the failure pattern are examined as a function between the layer plane and the loading direction. A time shift was shown to exist between the time at ultimate tensile stress and the time at fracture initiation. This phenomenon has been dubbed the Naet Shift.

Acknowledgements

This Master Thesis study has been made possible by the financial and technical contributions from SINTEF Petroleum Research, SINTEF Materials and Chemistry, The Technical University of Denmark and The Norwegian University of Science and Technology.

I would firstly like to thank my supervisors Rune Holt and Andreas Bauer for accepting my research opportunity and for their encouraging and ongoing support and offering their constructive advice during the project. A big thankyou to Anna Stroisz, who kindly assisted and offered her time and technical expertise throughout the project period, in addition to keeping me company during the late nights at SINTEF. Anna I wish you all the best finishing your doctorate thesis and I hope that you are extremely satisfied with the results.

I would also like to thank Ida Lykke Fabricius, Robin Vacher and Andre Vervoot who offered external assistance over the project period. In addition I would like to thank Hans Lund who assisted with the sample preparations in the Lab.

To all the friends I have made along the way I would like to say that you have really made this experience an extremely happy and enjoyable chapter of my life. Memories of the people, relationships and contacts I have made in Denmark, (DTU) and in Norway (NTNU) will always remain dear to me.

Finally, I would like to thank my family, in particular Mum and Dad for giving me the financial and moral support since leaving Australia to allow me to explore these opportunities abroad.

"Remember the past, plan for the future, but ***LIVE FOR TODAY****"*

(N.Simpson 1st day at DTU 29.08.11)

Contents

1 Experimental Setup **1**
- 1.1 Introduction . . . 2
- 1.2 Rock Properties . . . 2
  - 1.2.1 Gas Shale . . . 3
  - 1.2.2 Mancos Shale Gas Play Information . . . 4
  - 1.2.3 Mancos Shale Geological Description . . . 4
  - 1.2.4 Mancos Shale Resource Estimate . . . 4
  - 1.2.5 Sandstone . . . 5
  - 1.2.6 Chalk . . . 5
  - 1.2.7 Shale . . . 5
- 1.3 Experimental Procedure . . . 5
  - 1.3.1 Sample Orientation . . . 5
  - 1.3.2 Sample Preparation . . . 7
  - 1.3.3 Acoustic Velocities . . . 7
  - 1.3.4 Sample Surface Preparation . . . 8
  - 1.3.5 The Brazilian Test . . . 8
  - 1.3.6 Acoustic Emission . . . 9
  - 1.3.7 High Speed Camera . . . 9
  - 1.3.8 Camcorder Camera . . . 9
- 1.4 Discussion . . . 10
  - 1.4.1 Acoustic Emission . . . 10
  - 1.4.2 High Speed Camera . . . 10
  - 1.4.3 Camcorder Camera . . . 10
  - 1.4.4 Digital Image Correction (DIC) . . . 11
  - 1.4.5 Image Subtraction . . . 11
  - 1.4.6 Crack Lengths . . . 12
- 1.5 Conclusion . . . 12

2 Acoustic Velocities **13**
- 2.1 Introduction . . . 13
  - 2.1.1 Anisotropy . . . 13
  - 2.1.2 Acoustic Waves . . . 14
- 2.2 Experimental Procedure . . . 15
- 2.3 Results and Observations . . . 15
- 2.4 Discussion and Conclusions . . . 16

3 Tensile Strength **17**
3.1 Introduction . . . 18
3.1.1 Tensile Strength . . . 18
3.1.2 The Brazilian Test . . . 18
3.2 Experimental Procedure . . . 19
3.2.1 Sample Preparation . . . 19
3.2.2 Test Apparatus . . . 19
3.2.3 Experimental Method . . . 19
3.3 Results and Observations . . . 21
3.4 Discussion . . . 21
3.5 Conclusion . . . 23

4 Stress Distribution **25**
4.1 Introduction . . . 26
4.1.1 Objective . . . 26
4.1.2 Stress . . . 26
4.1.3 The Brazilian Test . . . 26
4.2 Mohr's Circle . . . 27
4.3 Brazilian Disc Stress Fields . . . 28
4.3.1 Analytical Stress Fields . . . 28
4.3.2 Isotropic Stress Components . . . 28
4.3.3 Anisotropic Stress Components . . . 29
4.3.4 Principle Stresses . . . 29
4.4 Discussion and Conclusions . . . 29

5 Fracture Initiation **31**
5.1 Introduction . . . 31
5.1.1 Objective . . . 31
5.1.2 Griffith's brittle fracture theory . . . 32
5.1.3 Mixed Observations . . . 32
5.1.4 Experimental Methods . . . 33
5.2 Experimental Procedure . . . 33
5.2.1 Brazilian Test . . . 33
5.2.2 Acoustic Emission . . . 33
5.2.3 High Speed Camera . . . 33
5.3 Results and Discussion . . . 35
5.3.1 Fracture Initiation Location . . . 35
5.3.2 The Strain Criterion . . . 35
5.3.3 Pre Existing Cracks . . . 36
5.3.4 Fracture Initiation Time . . . 36
5.3.5 Location Map . . . 39
5.4 Conclusions . . . 40

6 Fracture Propagation **41**
6.1 Introduction . . . 42
6.1.1 Propagation Modes . . . 42
6.1.2 Experimental Methods . . . 42

6.1.3 Types of Fractures . . . 43
6.1.4 Objective . . . 43
6.1.5 The Naet shift . . . 43
6.2 Experimental Procedure . . . 44
6.2.1 Brazilian Test . . . 44
6.2.2 High Speed Camera . . . 44
6.3 Results and Discussion . . . 44
6.3.1 Observation of crack propagation . . . 44
6.3.2 Crack Propagation Time . . . 46
6.3.3 Fracture Patterns . . . 48
6.4 Conclusion . . . 48

7 Fracture Modelling & Future Work 51
7.1 Introduction . . . 52
7.2 Numerical Modelling . . . 52
7.2.1 Numerical Methods . . . 52
7.2.2 Boundary Element method (BEM) . . . 53
7.2.3 Finite Element Method (FEM) . . . 54
7.2.4 Finite Difference Method (FDM) . . . 54
7.2.5 Discrete Element Method (DEM) . . . 54
7.3 Brazilian Test Modelling . . . 55
7.3.1 Isotropic Rock Models . . . 55
7.3.2 Anisotropic Rock Models . . . 55
7.4 Model Validation . . . 56
7.5 Experimental Improvements and Future Work . . . 57
7.6 Conclusion . . . 58

Appendix A Shale Gas Outlook 59
A.1 Future Energy Outlook . . . 60
A.1.1 World Energy Demand . . . 60
A.1.2 Economics and Technology . . . 61
A.1.3 World Natural Gas Production . . . 61
A.2 Reservoir Types . . . 61
A.2.1 Conventional Reservoirs . . . 61
A.2.2 Unconventional Reservoirs . . . 61
A.3 Unconventional Gas . . . 62
A.3.1 The Gas Resource Triangle . . . 62
A.3.2 Unconventional Gas Types . . . 63
A.4 Shale Gas . . . 64
A.4.1 Global Supplies . . . 64
A.4.2 Production Forecasts . . . 65
A.5 Conclusion . . . 65

Appendix B P-wave velocity Data 67
B.1 Mancos Shale statistical P-wave velocity data . . . 67
B.2 All Rock Types P-wave velocity data . . . 67

Appendix C Tensile Stength Data **69**
C.1 Mancos Shale Tensile Strength Statistics (All) 69
C.2 Mancos Shale Tensile Strength Statistics (Dry) 69

Appendix D Fracture Initiation Location **71**
D.1 Mancos Shale (dry) $\beta = 0°$ 71
D.2 Mancos Shale (dry) $\beta = 15°$ 72
D.3 Mancos Shale (dry) $\beta = 30°$ 72
D.4 Mancos Shale (dry) $\beta = 45°$ 72
D.5 Mancos Shale (dry) $\beta = 60°$ 73
D.6 Mancos Shale (dry) $\beta = 75°$ 73
D.7 Mancos Shale (dry) $\beta = 90°$ 73
D.8 Castlegate Sandstone (dry) 74
D.9 Mons Chalk (dry) 74
D.10 Mons Chalk (sat) 74

Appendix E Fracture Initiation Time **75**
E.1 Estimated and Observed Time of Fracture Initiation 75
E.2 Mancos Shale (dry) $\beta = 0°$ 76
E.3 Mancos Shale (dry) $\beta = 15°$ 77
E.4 Mancos Shale (dry) $\beta = 30°$ 78
E.5 Mancos Shale (dry) $\beta = 45°$ 79
E.6 Mancos Shale (dry) $\beta = 60°$ 80
E.7 Mancos Shale (dry) $\beta = 75°$ 81
E.8 Mancos Shale (dry) $\beta = 90°$ 82

Appendix F Location Map Results **83**
F.1 Mancos Shale (dry) $\beta = 0°$ 83
F.2 Mancos Shale (dry) $\beta = 15°$ 84
F.3 Mancos Shale (dry) $\beta = 30°$ 85
F.4 Mancos Shale (dry) $\beta = 45°$ 86
F.5 Mancos Shale (dry) $\beta = 60°$ 87
F.6 Mancos Shale (dry) $\beta = 75°$ 88
F.7 Mancos Shale (dry) $\beta = 90°$ 89
F.8 Castlegate Sandstone (dry) 90
F.9 Mons Chalk (dry) 91
F.10 Mons Chalk (sat) 91

Appendix G Fracture Propagation Time **93**
G.1 Mancos Shale (dry) $\beta = 0°$ 93
G.2 Mancos Shale (dry) $\beta = 15°$ 94
G.3 Mancos Shale (dry) $\beta = 30°$ 94
G.4 Mancos Shale (dry) $\beta = 45°$ 94
G.5 Mancos Shale (dry) $\beta = 60°$ 95
G.6 Mancos Shale (dry) $\beta = 75°$ 95
G.7 Mancos Shale (dry) $\beta = 90°$ 95

Appendix H Fracture Patterns Including Images **97**

Bibliography **99**

Chapter 1

Experimental Setup

Nathaniel Simpson

Experimental Description and Methods for *Incorporating a High Speed Camera and the Acoustic Emission technique to a traditional Brazilian Test*

Summary

This Chapter attempts to further our knowledge of fracture behaviour by establishing an experimental system that links tensile strength, fracture initiation and propagation of an anisotropic rock (Mancos Shale) using an integrated Brazilian Test Setup equipped with Acoustic Emission and High Speed Video. The unique experimental configuration was applied to an anisotropic gas shale (Mancos Shale) in addition to other petroleum related reservoir rocks (such as sandstone and chalk). Acoustic emission data may be used to generate an event location map. High-speed video footage (at time of fracture) is used to observe fracture initiation and propagation. Digital image correlation software (7D) can then be applied to assess the local displacement and strain fields at the sample surface. Additional image analyses may be achieved through image subtraction and digital measurements of fracture lengths (using CAD software).

1.1 Introduction

Future energy predictions show that shale gas will play an important role in meeting the increasing energy demands of the future (Appendix A). Despite the large volume of initial gas in place, artificial stimulation treatments (horizontal drilling and hydraulic fracturing) are needed in order to produce shale gas economically.

A gas shale is not a rock type, and a wide variety of minerologies exist amongst different formations. Challenges in producing hydrocarbons from these rocks thereby relates not only to identifying the reservoirs, but also optimization of fracking procedures (Torsaeter et al., 2012).

This has motivated researchers, both in academia and industry, to characterise gas shale rocks in greater detail to provide more reliable predictions and an improved understanding of their behaviour (Torsaeter et al., 2012).

This study attempts to further our knowledge of this behaviour by establishing an experimental system that links tensile strength, fracture initiation and propagation of an anisotropic rock (Mancos Shale) using an integrated Brazilian Test Setup equipped with Acoustic Emission and High Speed Video (Figure 1.1).

This Chapter outlines in detail the aforementioned combined experimental setup with each subsequent chapter separately divided into self contained segments which present the results/investigations for the following topics; Acoustic Velocities, Tensile Strength, Stress Distribution, Fracture Initiation, Facture Propagation and Modelling Implications.

1.2 Rock Properties

There are four different rock types used in this study; Mancos Shale, Castlegate Sandstone, Mons Chalk and Pierre Shale. The main (anisotropic) rock of interest was the Mancos Shale with the Castlegate Sandstone used as the (isotropic) control specimen. As this experimental setup is unique in its nature further tests were also conducted on Mons Chalk and Pierre Shale to establish the applicability of the method to the Petroleum related rock types. The rock types along with their assumed analogues are listed below;

- Mancos Shale (anisotropic): Gas Shale Analogue
- Castlegate Sandstone (isotropic): Sandstone Reservoir Rock Analogue
- Mons Chalk (isotropic): Chalk Reservoir Rock Analogue
- Pierre Shale (anisotropic): Reservoir Cap Rock Analogue

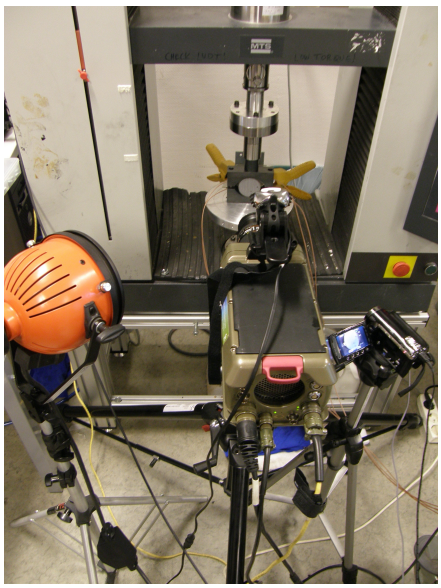

Figure 1.1: *Experimental Setup. The configuration uses a traditional Brazilian test setup with four acoustic sensors mounted to the rear of the sample. The imaging equipment includes a high–speed video camera (centre) and a camcorder camera (right). Lighting was provided through tungsten lamps (left) and a portable LED light (center)*

1.2.1 Gas Shale

The definition of gas shale that best describes the reservoir is "organic-rich, and fine-grained" (Rokosh et al., 2009). However, the term 'shale' is used very loosely and by intent does not describe the lithology of the reservoir. When talking about shale gas, the word shale does not refer to a specific type of rock. Instead, it describes rocks with more fine-grained particles (smaller than sand) than coarse-grained particles, such as (Alberta Geological Survey, 2012);

- shale (fissile) and mudstone (non-fissile)
- siltstone
- fine-grained sandstone interlaminated with shale or mudstone
- carbonate rocks.

Gas-prone shale may be associated with other resources, such as tight gas and coal bed methane (CBM), in areas where shale is interbedded with coal (Alberta Geological Survey, 2012).

Gas shales are source rocks that have not released all of their generated hydrocarbons. In fact, source rocks that are "tight" or "inefficient" at expelling hydrocarbons may be the best prospects for shale gas potential (Alberta Geological Survey, 2012).

In gas shale, shale is a reservoir, source rock and trap for natural gas however, it should not be overlooked that shale still has the potential to be a seal or cap rock and that not all shales are necessarily reservoir rocks (Rokosh et al., 2009).

The lack of a strict definition for shale causes an additional degree of difficulty for resource evaluation. Such a broad spectrum of lithology appears to form a transition with other resources, such as 'tight gas', where the difference between it and gas shale may be that tight gas reservoirs generally contain no organic matter (Rokosh et al., 2009), a differentiation which is also followed in this study.

The variety of rock types observed in organic-rich 'shale' implies the presence of a range of different types of 'shale gas' reservoirs. Each reservoir may have distinct geochemical and geological characteristics that may require equally unique methods of drilling, completion, production and resource and reserve evaluation (Nash, 2010).

The Gas Shale analysed in this study is the Mancos Shale. There are a number of sources which have collected information regarding the properties for the Mancos Shale (McLennan et al., 1983) (EIA, 2011a) (Torsaeter et al., 2012).

The Average General Properties for Mancos "B" Shale given below is from Sarker and Batzle (2010).

Table 1.1: Mancos Shale Properties

Composition	39% quartz, 33% clay minerals[1], 17% carbonates
Total Organic Content (wt %)	1.36
Porosity (%)	6.8
median pore throat radius (micron)	0.0148
Vertical Permeability (nDarcy)	8–20

[1]Illite comprises 70% of the clay minerals.

1.2.2 Mancos Shale Gas Play Information

The Mancos shale gas play is located within the Uinta Basin in Colorado and Wyoming (shaded in red in Figure 1.2).

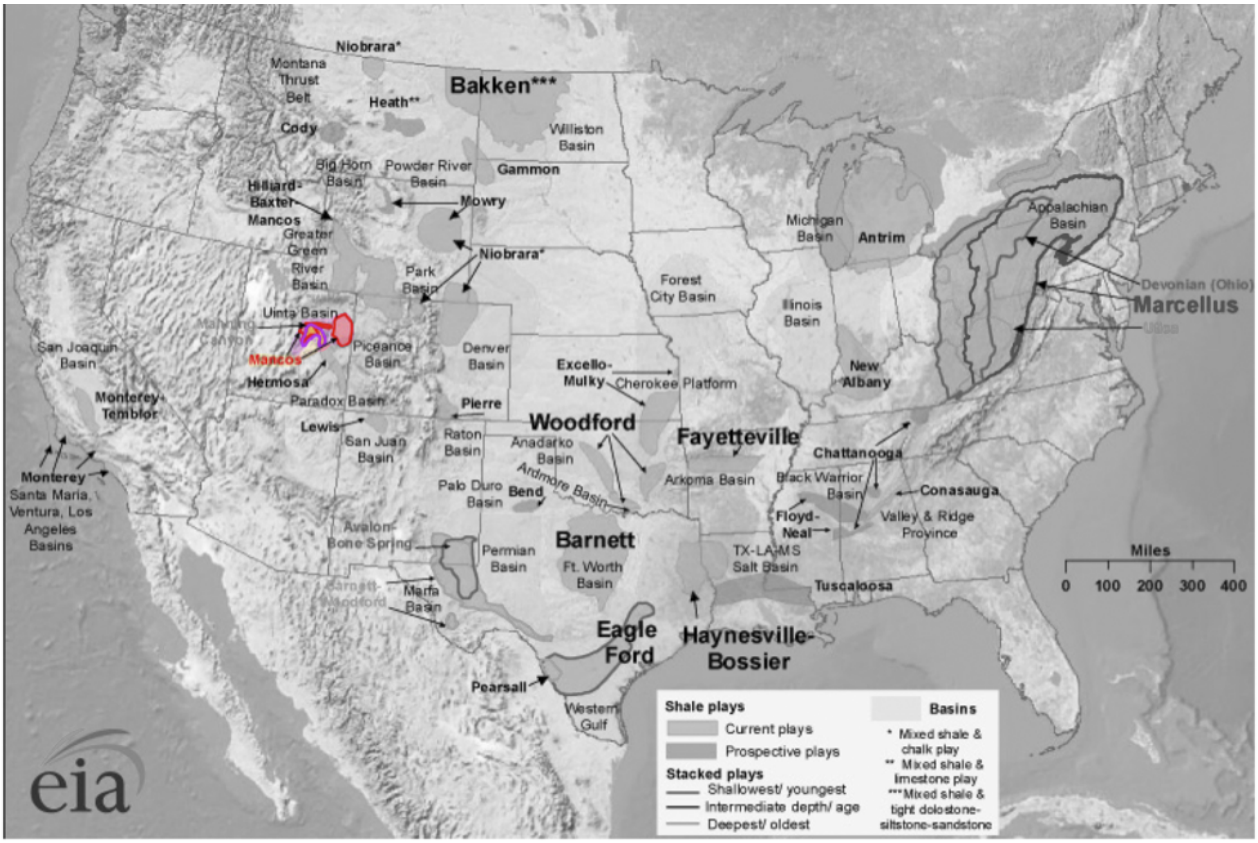

Figure 1.2: *Lower 48 states shale plays. Source (EIA, 2011a)*

1.2.3 Mancos Shale Geological Description

The Mancos Shale is dominantly a grey marine shale that was deposited in the seaway that occupied much of the Western Interior region during most of the Cretaceous. This formation consists of several thousand feet of predominantly dark grey shales at the base and interbedded sands and shale at the top (Mancos "A" above Mancos "B"). The formation generally lies between the Dakota Sandstone and the Mesaverde Group (or their equivalents) (McLennan et al., 1983).

1.2.4 Mancos Shale Resource Estimate

In 2002, the Mancos shale was assessed with a median assessment area of 4,217,000 acres (6,589 square miles) with the EUR for the Mancos reported as approximately 1.0 Bcf per well. The Mancos shale gas play is estimated to have 21.02 Tcf of technically recoverable gas with typical well spacing of 40 to 80 acres (EIA, 2011a).

The shale is estimated to be between 13,000 and 17,500 feet deep and have a thickness of 3,000 feet (EIA, 2011a).

1.2.5 Sandstone

The dominant grain sizes of sandstone are typically 0.01–1 mm. Pore sizes are the same order of magnitude, but slightly smaller. This gives permeabilities ranging from microDarcy to several Darcies. The predominant matrix mineral is quartz (E. Fjaer et al., 2008).

1.2.6 Chalk

Chalk particles originate as skeletons of algae that are called coccospheres, with a typical initial size of 30 μm. During burial the coccospheres are crushed, and most particles (and pores) of present chalk are in the range of a few (1–10) μm, with associated matrix permeabilities between micro- and milliDarcy (E. Fjaer et al., 2008).

The predominant mineral of Chalk is calcite, and it may also contain other minerals such as silica and clay minerals. In North Sea chalk reservoirs, porosities of 15–50% are found at depths of 2500–3500 m due to overpressure. These reservoirs are also naturally fractured, leading to high reservoir scale permeabilities in the 100 milliDarcy range (E. Fjaer et al., 2008).

1.2.7 Shale

From the rock mechanical viewpoint, it is natural to define a shale as a rock in which clay minerals constitute a load-bearing framework. In practice this means that clay content needs to be higher than about 40% (E. Fjaer et al., 2008).

Because of the large abundance of clay minerals, pore sizes in shale are very small; typically between 5 and 25 nm. The nanometre size pores lead to laboratory-measured permeabilities in the nano-Darcy range. North Sea shales typically display porosities of 30–55% (E. Fjaer et al., 2008).

1.3 Experimental Procedure

1.3.1 Sample Orientation

The experimental arrangement for the Brazilian tests is illustrated in Figure 1.3 with respect to the orientation of the bedding planes. Let x, y, z be a global Cartesian coordinate system with the z-axis defining the longitudinal axis of the disc. The surface forces are assumed to be in equilibrium. The angle β is defined as the inclination angle between the loading direction (y) and bedding (on the x-y plane). The angle ψ is defined as the inclination angle between the loading direction (y) and bedding (on the z-y plane). A complete list of possible configurations can be seen on Figure 1.4.

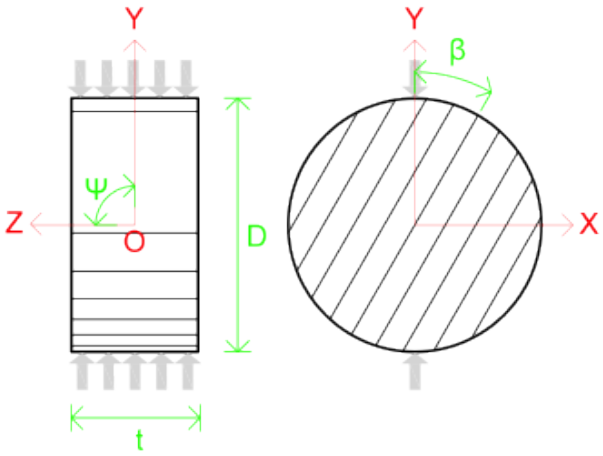

Figure 1.3: *Disc-shaped sample and configuration of layers in Brazilian tests. β varies between 0° and 90°. Set of inclined parallel lines symbolizes average layer direction (bedding). This setup has $\beta = 30°$ and $\psi = 90°$*

The Brazilian test is an (indirect) way of determining the tensile strength of a material. It is important to create a simple labelling convention, which allows simple comparisons to other test types (i.e. direct tensile strength tests, Unconfined Compressive Strength tests etc.). Figure 1.5 displays bedding inclination angles for a range of different mechanical tests.

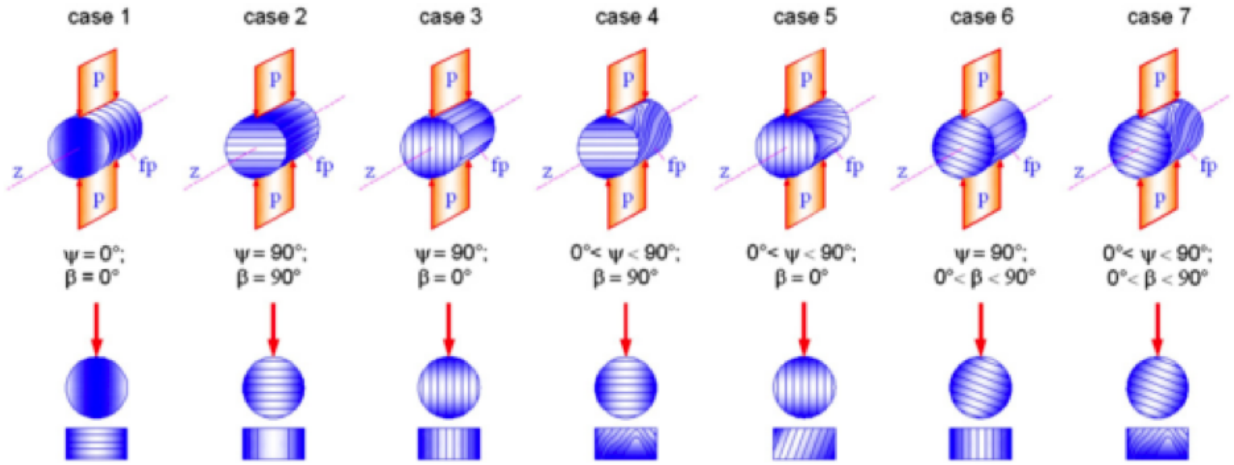

Figure 1.4: *Experimental arrangement for testing rock anisotropy relative to ψ (the inclination angle between the loading direction (y) and bedding on the z-y plane) and β (the inclination angle between the loading direction (y) and bedding on the x-y plane) using the Brazilian test Modified from (Quoc et al., 2013).*

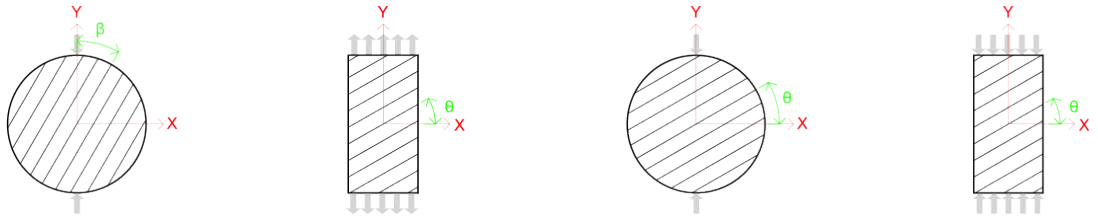

(a) BTS (b) TS (c) AV (d) UCS

Figure 1.5: *Inclination angle (to bedding) for a range of mechanical tests (a) Brazilian Tensile Strength, (b) direct Tensile Strength, (c) Acoustic Velocity and (d) Unconfined Compressive Strength. θ is defined as the angle between the x-axis and the bedding plane, whereas β is defined as the angle between the y-axis and the bedding plane. The Brazilian test is an indirect method for determining tensile strength of a material. Due to the disc geometry, the tensile stresses are applied perpendicular to the applied load. BTS values measured at $\beta°$ are designed to be analogous to direct TS values measured at $\theta°$. This setup has $\beta = \theta = 30°$.*

1.3.2 Sample Preparation

The sample preparations and tests followed the procedures as given by the International Society for Rock Mechanics (ISRM, 1978). The specimens were all disc-shaped with a diameter, D to thickness, t ratio of 2 and the following approximate dimensions.

Table 1.2: Sample Dimensions

Sample	Diameter [mm]	Thickness [mm]
Mancos Shale	48	24
Castlegate Sandstone	48	24
Mons Chalk	48	24
Pierre Shale	38	19

At the beginning of the sample preparations, cylindrical cores with the diameters defined above were drilled out of each of the larger rock blocks and cut into test specimens of suitable thickness.

Castlegate Sandstone and selected Mons Chalk Samples were then dried in a sample oven (set to 60°Celsius) for over 48 hours. The remaining Mons Chalk samples were marked (Section 1.3.4) then saturated with water under vacuum with the use of a pump.

The shale samples were cored so that the axis of the cylindrical cores had a predefined direction to the bedding planes of $\psi = 90°$ (i.e. drilled parallel to bedding). The cores were then cut into test specimens of suitable length and the end faces ground and hand polished (using Norton T489 Sheet P320 sandpaper). Afterwards, specimens were marked at measured predefined increments in relation to bedding planes ($\beta = 0°$, 15°, 30°, 45°, 60°, 75°, 90°). The adjacent stencil (Figure 1.6) was customized to assist with marking the samples at the various increment angles.

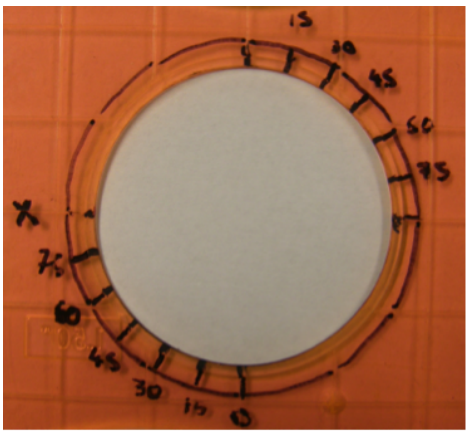

Figure 1.6: *Customised Stencil, with* 15° *increments to assist with sample markings*

The shale specimens were stored in inert oil to avoid desiccation effects.

1.3.3 Acoustic Velocities

The ultrasonic P-wave velocities for selected samples were recorded at 15°increments along the loading direction and centrally through the middle of the sample (C).

The diameter and thickness of all samples were measured prior to acoustic measurement. All experiments were carried out at atmospheric conditions.

The velocity was derived by transmitting an ultrasonic P-wave on one end of the sample and receiving it on the other end. This was done using a Tektronix TDS 3012B Oscilloscope, Agilent Technologies 33220A Generator and a Hewlett Packard 34970A Switch Unit with a 1MHz transmitter.

The P-wave velocities were determined with the programs MATLAB (The MathWorks Inc., 2013) and Speedy (SINTEF Petroleumsforskning AS, 2013), using the first zero crossing and PEEK measurements as reference points.

The coupling fluid and the number of samples are summarized In Table 1.3.

Table 1.3: Sample Dimensions

Sample	Coupling Fluid	Num. Tested
Mancos Shale (oil)	Inert oil	24
Castlegate Sandstone (dry)	Golden Syrup	1
Mons Chalk (dry)	Golden Syrup	1
Mons Chalk (sat)	Water	1
Pierre Shale (oil)	Inert oil	1

1.3.4 Sample Surface Preparation

Selected samples were then prepared further prior to Brazilian testing. Surface preparation was required for the digital image correction analysis (Section 1.4.4).

Note: A list of seven samples marked at 15° increments in relation to the bedding planes (i.e. $\beta = 0°$, 15°, 30°, 45°, 60°, 75°, 90°) is referred to here as a 'set'.

5 sets of Mancos Shale Samples were tested in this study. The specifics of preparation for each set are described below.

- Mancos Set 1 (painted): A specimen is removed from the inert oil, wiped using a paper towel and sanded on the face which has not been marked. The sanded face is then lightly sprayed with some low-cost mat spray paints. First, a fine thin white coat is applied such that the pre-existing markings are not visible, then after a few minutes a thin speckle of black spray paint is applied (Figure 1.7a). The sample is then measured, photographed and weighed prior to the Brazilian test.

- Mancos Set 2 – 4 (dry): A specimen is removed from the inert oil, wiped using a paper towel and sanded on the face which has not been marked (Figure 1.7b). The sample is then measured, photographed and weighed prior to the Brazilian test.

- Mancos Set 5 (oil): A specimen is removed from the inert oil, wiped using a paper towel and then measured, photographed and weighed. The sample is then coated with oil prior to the Brazilian test (Figure 1.7c).

(a) painted (b) dry (c) oil

Figure 1.7: *Specimen surfaces*

To soften the steel rock contacts, the discs were wrapped by a layer of paper masking tape and placed inside the curved steel jaws of the Brazilian frame within 30 minutes of initially being removed from the inert oil.

The Pierre Shale (dry) samples follow a similar procedure as what was described for the Mancos Shale (dry) samples. Only a thin speckle of black spray paint was required for the Mons Chalk Samples to create identifiable markers for the Digital Image Correction (DIC) analysis (Section 1.4.4).

1.3.5 The Brazilian Test

The rock mechanics test system MTS 2/M was employed for the indirect tensile tests. MTS 2/M is a computer-controlled machine with a maximum load capacity of 10kN. The TestWorks-4 System Software was used to conduct computer-controlled tests. The load and displacement were measured by the load cell. An analog output channel was created so

the data could be transferred to the acoustic system with a synchronized time stamp.

The disc sample was preloaded to 400N at a loading rate of 0.05mm/s and the acoustic emission sensors mounted (Section 1.3.6). The test was then loaded up to failure with an unchanged loading rate of 0.003mm/s.

1.3.6 Acoustic Emission

Acoustic Emission (AE) was measured using an AMSY-5 System by Vallen GmbH. Each signal was amplified by a preamplifier with an amplification of 34 dB. Four wide band sensors were used of type B1025 (Digital Wave Corp., USA), which have a radius of 4.5mm and a frequency range from 50kHz to 2MHz. The minimum threshold to measure signals was set to 23.8dB. The Disc specimens were first pre loaded to 400 N using the MTS frame. The sensors were then mounted on the rear side of the disc specimen in a square configuration 20mm apart using a custom made sensor holder (Figure 1.8) and the sensor thresholds tested. The disc was then loaded until failure, and acoustic events (hits) stored within the acoustic system.

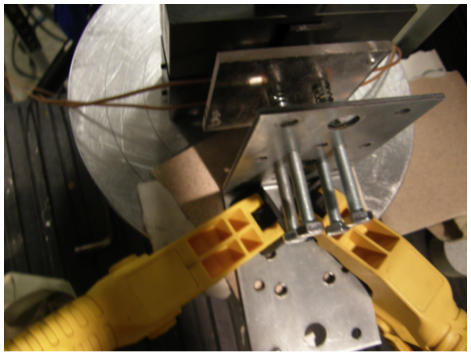

Figure 1.8: *Acoustic sensors mounted to the rear of the disc specimen with the assistance of a customised frame and clamps.*

1.3.7 High Speed Camera

Digital images were recorded during the deformation process at a rate of 5,000 frames per second using a Phantom v12 high speed camera and PCC software (Vision Research). The camera's memory can store approximately 4 seconds of footage (at 5,000 fps) after it is manually triggered (in this case after the main fracture). An analog output channel from the high-speed camera was linked into the acoustic emission system to time stamp the point at which the trigger was initiated. The image resolution was set to 704×704 pixels with an exposure time of 190μs. Up to two 1000 watt tungsten lamps and a Magicshine (MJ-880E) 2200 lumen LED bike lamp were utilized to supply sufficient lighting when required.

1.3.8 Camcorder Camera

As the time period of the high-speed camera was limited to 4 seconds an additional JVC Everio Camcorder camera was used to capture images at 25 frames per second in HD 720p (1280×720 pixels) for the full length of the test. A primitive (but effective) technique was used to time stamp the camcorder to the acoustic emission system. Prior to the continuation of the Brazilian test (after the acoustic emission sensors had been mounted) a spring was used to hit the surface of the specimen and create an acoustic emission event that could later be used to link the two systems.

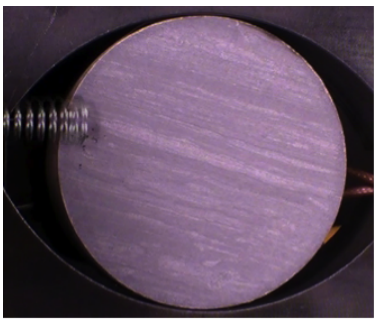

Figure 1.9: *A spring is used to timestamp the camcorder video footage with the acoustic system.*

1.4 Discussion

1.4.1 Acoustic Emission

By specifying the sensor positions, an event location map can be generated using the Vallen Software (assuming an isotropic medium and using a value for the acoustic velocity). The location algorithms assume an isotropic material and work on an iterative basis, approximating the source location. For a 2D solution, the iterative location algorithm needs at least data from 3 measurement channels.

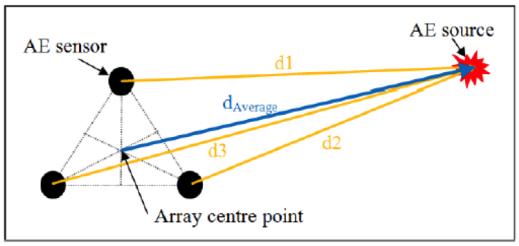

Figure 1.10: *Sensor to Source distance. Source (Aljets et al., 2010)*

1.4.2 High Speed Camera

One of the hurdles when filming at high speeds is the considerable amount lighting and illumination that is required. Beyond illumination, the largest issue in high-speed lighting is flicker (Love High Speed, 2013). When powered by alternating current (AC) electricity, lamps have a power cycle of 50 or 60 times per second (depending on the country and its power system). During the down cycle the lamp filament can dim slightly. When filming at a high rate, the alternation in the lamp becomes visible and a flicker appears on the footage. The amount of flicker is related to the type of bulb, wattage and type of filament used. In this study, up to two 1000–watt lamps with tungsten filaments were utilized to minimise flicker (in these lamps, the filaments have a reduced time to cool and dim before the power cycles back up again). Additionally, a battery powered LED light was used to improve lighting when required. The colour difference in the images below highlight the different effects the various lighting configurations may have.

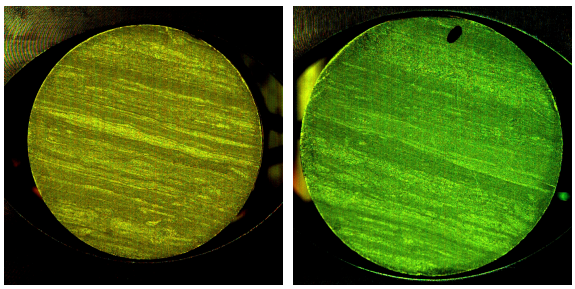

(a) Tungsten light (b) LED Light

Figure 1.11: *Samples filmed with different lighting configurations*

Generally LED fixtures designed for filming will not flicker as long as they are not dimmed. An ideal lighting configuration would be to use DC power that would eliminate flicker entirely, or to utilise bigger lights (i.e. 5000 watts or larger) to further reduce the effect of the tungsten cooling between cycles (Love High Speed, 2013).

1.4.3 Camcorder Camera

It was hoped that the camcorder footage could be used to visualise the elastic strain map prior to fracture; however this was not possible due to minor movement of the samples in the test frame.

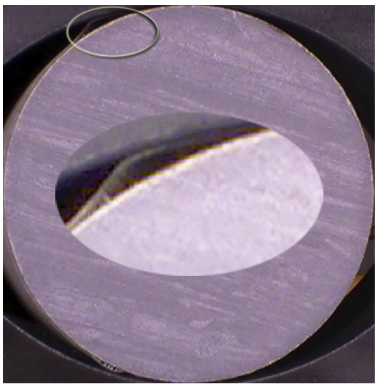

Figure 1.12: *Evidence of movement (or rocking) during the Brazilian test.*

Current HD cameras typically capture video at around 2 mega pixels (MP) when filming in high definition, whereas many inexpensive digital (still) cameras are capable of capturing images in excess of 10 MP. If movement could be minimised then it is suggested that a digital camera used together with a time–lapse remote controller could be an effective alternative for measuring pre fracture strain development (compared to using a camcorder video camera). An increased quantity of pixels may provide further accuracy when performing the digital image correction analysis.

1.4.4 Digital Image Correction (DIC)

The Digital Image Correlation (DIC) method was used to assess the local displacement and strain fields at the sample surface with "7D" correlation software (Vacher et al., 1999). For each test, the initial image is split in square elements that create a virtual grid upon the sample surface (Figure 1.13). The resolution of this grid (extensiometric base) is set to 10×10 pixels.

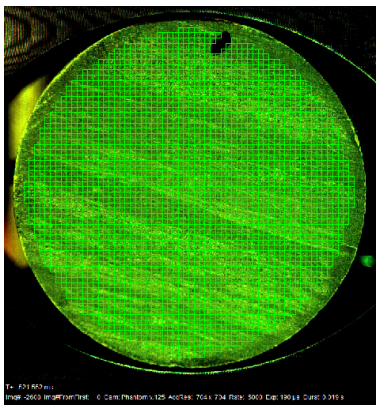

Figure 1.13: *Virtual grid on the sample surface*

The correlation process consists in looking for the most probable deformed pattern in the neighbourhood of each node of this grid in terms of colour level. The displacement fields of each element are then assessed by the means of a bi–linear interpolation and the strain field calculated using Green–Lagrange's tensor (E) (Vacher et al., 1999).

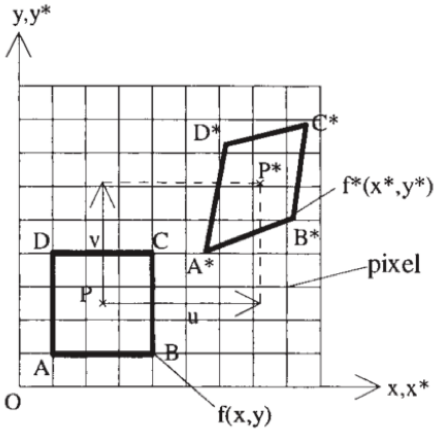

Figure 1.14: *Displacement field u(x,y) and v(x,y) between an initial image and a deformed image. Source (Vacher et al., 1999)*

This strain measurement tool in a plane makes it easy to obtain the biaxial strains on a sheet after a deep drawing operation (Toussaint et al., 2008). The measurement field available is wide, and possible measured values are (Vacher et al., 1999):

1. elastic strains with a 0.01 per cent precision,
2. large strains > 200 per cent and
3. any rigid body displacements and rotations

Note: It was discovered during testing that the natural markers of Mancos Shale were sufficient for the DIC method and so only one set of samples were painted.

1.4.5 Image Subtraction

For this analysis, an image (post fracture) is subtracted from an initial image (pre fracture) to obtain the result in Figure 1.15. The freeware software Handbrake (The Handbrake

Team, 2013) was used to convert video footage into a readable format. Afterwards, QuickTime 7 (Apple Inc., 2013) was used to export the video into an image sequence. Finally the program Photoshop C6 (Adobe, 2013) was utilised to subtract one image from the other.

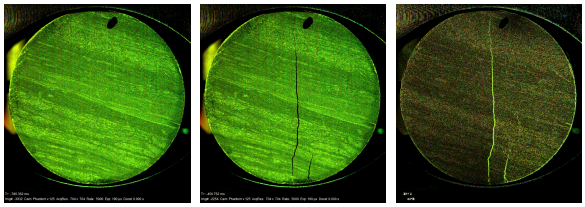

(a) initial (b) deformed (c) subtracted

Figure 1.15: *An initial image (a) is subtracted from a deformed image (b) to create the subtracted image (c)*

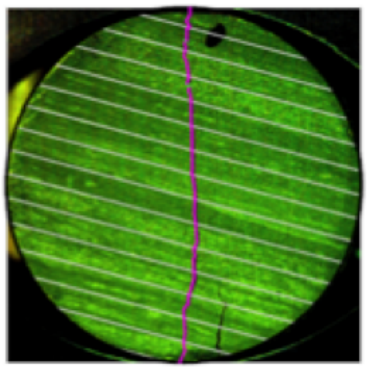

Figure 1.16: *The fracture patterns of the 'central region' after diametrical loading of disk shaped Mancos Shale sample at* $\beta = 75°$*. The parallel thin grey lines indicate the layer direction; Layer Activation is represented in green and central fractures in magenta. Note that non-central fractures were not investigated in this analysis.*

1.4.6 Crack Lengths

Crack lengths may be accurately measured with the use of CAD software. AutoCAD (AutoDesk, 2013) was the chosen software for this study. In order to determine the appropriate fracture lengths of a sample, an image from the video footage is taken (after fracture propagation), and appropriately cropped and resized to the measured diameter length, D. The line and measure features within AutoCAD may then be used to accurately measure the fracture crack lengths within the sample digitally (Figure 1.16).

1.5 Conclusion

In this chapter, an experimental procedure that links fracture development, initiation and propagation, through Mancos Shale (an anisotropic gas shale) was presented through using an integrated Brazilian test setup equipped with acoustic emission and high speed video. This unique experimental configuration was applied to an anisotropic gas shale (Mancos Shale) in addition to other petroleum related reservoir rocks (such as sandstone and chalk) in order achieve an improved understanding of the fracture process. Acoustic emission data may be used to generate an event location map. High-speed video footage (at time of fracture) is used to observe fracture initiation and propagation. Digital image correlation software (7D) can then be applied to assess the local displacement and strain fields at the sample surface. Additional image analyses may be achieved through image subtraction and digital measurements of fracture lengths (using CAD software). The subsequent chapters of this study discuss how this integrated information may be used to develop further insights into the fracturing process.

Chapter 2

Acoustic Velocities

Nathaniel Simpson

Statistical analysis on *The P-wave velocity distribution of Mancos Shale*

Summary

P-wave velocity measurements taken at 15 increment angles to bedding indicate that the Mancos Shale has moderate acoustic anisotropy. This suggests that the elastic moduli may differ at various directions within the rock. Specimens were drilled parallel to bedding which correlates to a transversely isotropic material with a horizontal axis of symmetry (TIH). Statistical analysis revealed variances between measured velocities from the same sample of rock. The factors, which may explain these results, include natural variations in; micro-cracks and jointing, fabric, rock joints, interbedding and faults in addition to any damage that might occur during sample preparation. The P-wave velocities will be used further in the tensile strength and fracture initiation chapters of the report.

2.1 Introduction

2.1.1 Anisotropy

Anisotropy is the property of being directionally dependent, as opposed to isotropy, which implies identical properties in all directions (E. Fjaer et al., 2008). Anisotropic materials can be homogeneous (uniform composition) and the term should not be confused with Heterogeneity. Anisotropy describes variations of the physical properties with direction at a given point, whereas heterogeneity describes variations of physical properties between two or more points (Petroleum Seismology Network, 2013).

A material as a result of anisotropy may exhibit inconsistent physical and mechanical properties (i.e. absorbance, refractive index, conductivity, tensile strength etc.) when measured along different axes.

Waves can also travel through some rocks with different velocities in different directions.

This phenomenon, called spatial elastic anisotropy, occurs if there is spatial ordering of crystals, grains, cracks bedding planes, joints or fractures essentially an alignment of strengths or weaknesses on a scale smaller than the length of the wave. This alignment causes waves to propagate fastest in the stiffest direction (Armstrong et al., 1994). Thus the elastic moduli of anisotropic materials may be different for various directions in the material (E. Fjaer et al., 2008).

There are two types of alignment in earth materials and they give rise to two types of anisotropy. Such materials are called transversely isotropic with a vertical (TIV) or horizontal (TIH) axis of symmetry (Figure 2.1).

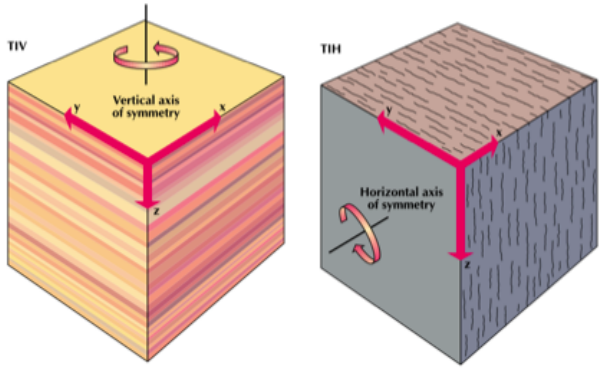

Figure 2.1: *Transversely Isotropic rocks with a vertical (left) and horizontal (right) axis of symmetry. Source (Armstrong et al., 1994)*

The Mancos Shale samples in this study were drilled parallel to bedding which corresponds to a material with aligned vertical weaknesses such as cracks or fractures, or with unequal horizontal stresses. Elastic properties vary in the direction crossing the fractures, but not along the plane of the fracture. Such a material is called transversely isotropic with a horizontal axis of symmetry (TIH). Waves travelling along the fracture direction but within the competent rock generally travel faster than waves crossing the fractures (Armstrong et al., 1994).

Identifying and measuring this type of anisotropy yields information about rock stress and fracture density and orientation. These parameters are important for the design of hydraulic fracture jobs (Armstrong et al., 1994).

2.1.2 Acoustic Waves

Waves come in three styles (Figure 2.2), all of which involve tiny motion particles relative to the undisturbed material (Armstrong et al., 1994).

- **Compressional or P, waves:** have particle motion in the direction of wave propagation (top).
- **Shear, or S, waves:** have particle motion orthogonal to the direction of wave propagation. S-wave particle is polarized in two directions, one horizontal (middle), one vertical (bottom).

This chapter analyses the measured P-wave velocities of Mancos Shale samples at various angles to bedding.

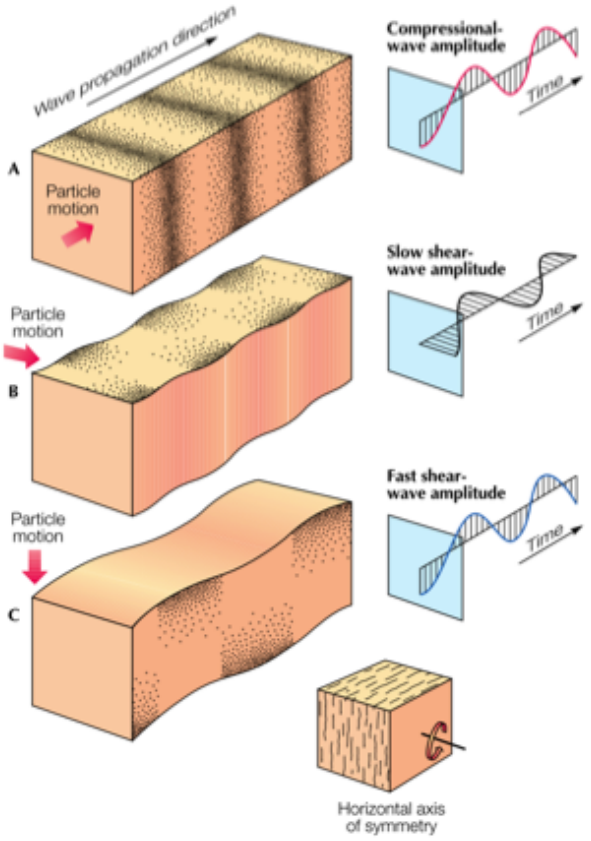

Figure 2.2: *Compressional and Shear waves. Source (Armstrong et al., 1994)*

2.2 Experimental Procedure

The ultrasonic P-wave velocities for selected samples were collected at various angles prior to Brazilian testing. Velocities were recorded at 15°increments along the loading direction and centrally through the middle of the sample (C) (Figure 2.3).

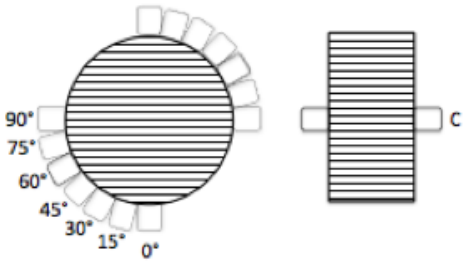

Figure 2.3: *P–wave velocity measurements*

The diameter and thickness of all samples were measured prior to acoustic measurement. All experiments were carried out at atmospheric conditions.

The velocity was derived by transmitting an ultrasonic P-wave on one end of the sample and receiving it on the other end. This was done using a Tektronix TDS 3012B Oscilloscope, Agilent Technologies 33220A Generator, Hewlett Packard 34970A Switch Unit with a 1MHz transmitter.

The P-wave velocities were determined with the programs MATLAB (The MathWorks Inc., 2013) and Speedy (SINTEF Petroleumsforskning AS, 2013), using the first zero crossing and PEEK measurements as reference points.

2.3 Results and Observations

Figure 2.4 shows how P-wave velocities vary with inclination for Mancos Shale. As generally observed on shales, velocities and moduli are largest parallel to bedding, decreasing gradually when approaching inclinations perpendicular to bedding (Torsaeter et al., 2012).

The 90°velocity measurements are approximately the same as the C measurements. This is expected as the samples were cored parallel to bedding.

Figure 2.5 shows the measured P-wave distribution of Pierre shale, Castlegate Sandstone and Mons Chalk measured at 15°increments around the sample. The Pierre shale displays a similar velocity trend as to what was witnessed in the Mancos Shale. It is interesting to note that the samples in this study which are assumed to be isotropic (namely the Castlegate Sandstone and Mons Chalk) also show signs of p-wave velocity variation.

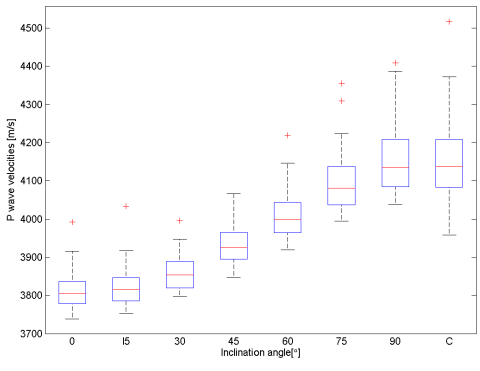

Figure 2.4: *Box and whisker plot of 24 Mancos Shale P-wave velocity measurements*

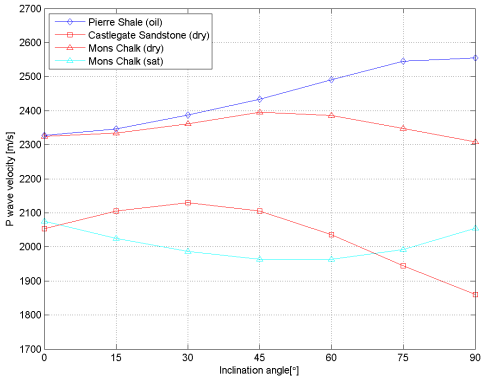

Figure 2.5: *P-wave velocity measurements at various angles around the samples*

Outliers are displayed by red + symbols on Figure 2.4. It is suspected that the outliers originate from samples with pre-existing cracks (Figure 2.6).

The spacings between the different parts of the box plot help indicate the degree of dispersion (spread) and skewness in the data. It appears that there can be variability of ±100 m/s between samples that were all cored from the same block. Figure 2.7 shows the natural variation that may exist within a sample. Although the cores were prepared so that they drilled parallel to bedding, it is important to recognise that natural variances do exist, which may effect the velocity measurements.

A statistical summary of all the P-wave measurements can be found in Tables B.1 and B.2.

2.4 Discussion and Conclusions

There are a number of various factors which can be a reason for velocity anisotropy. These include; micro-cracks and jointing, fabric, rock joints, interbedding and faults (Barton, 2007) in addition to any damage which might occur during sample preparation.

The P-wave velocity measurements are in agreement with the velocities as reported by Torsaeter et al. (2012). In the same paper they report that the Thomsen's anisotropy parameters for Mancos Shale are estimated as $\varepsilon \sim 0.09$ and $\delta \sim 0.06$, i.e. moderate acoustic anisotropy.

Although Castlegate Sandstone and Mons Chalk samples will be used as the Isotropic samples in this study, it is important to recognise that they also appear to exhibit anisotropic wave characteristics.

There are studies which link the P-wave velocity measurements to some mechanical properties for sedimentary rocks (Altindag, 2012). These measurements are important for location mapping (Section 5.3.5), and possible tensile strength relationships (Chapter 3).

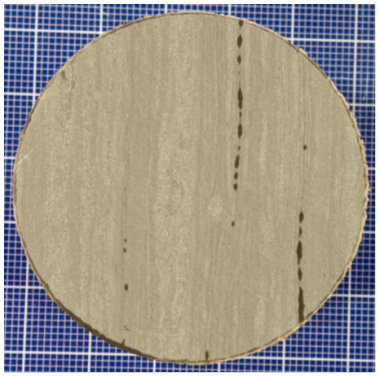

Figure 2.6: *Evidence of pre-existing cracks. During sample preparation, after the shale has been sanded, oil is still present.*

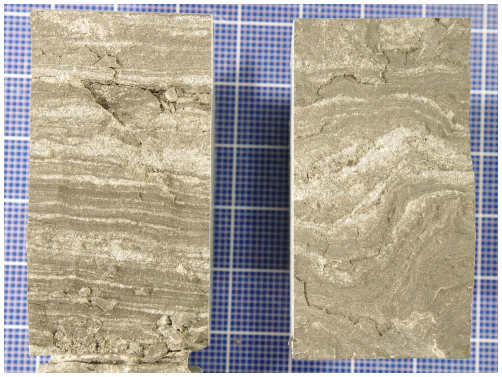

Figure 2.7: *Evidence of natural occurring variations within samples. The sample (left) displays an ideal value of* $\psi = 90°$*, the sample (right) displays unwanted variation of* $0° \leq \psi \leq 90°$

Chapter 3

Tensile Strength

Nathaniel Simpson

Experimental analysis on *The (indirect) Tensile Strength of Mancos Shale*

Summary

In this Chapter Brazilian tests are used to determine the effects of bedding angle on the ultimate tensile strength of an anisotropic rock (Mancos Shale). Tests were carried out in accordance with the ISRM- recommendations with cylindrical samples cored parallel to bedding with diameter, D=48 mm and thickness to diameter ratio t/D=0.5. Laboratory tests show that the degree of anisotropy has an influence on the measured peak strength, decreasing slightly with decreasing bedding angles, whereas the orientation of the sample in relation to the loading direction is relatively unimportant for nearly isotropic materials. The results from this study also suggest that the application of a thin paint layer increases the peak strength of Mancos Shale, possibly due to the change in internal stresses within the sample.

3.1 Introduction

3.1.1 Tensile Strength

The recovery of shale gas requires artificial stimulation (often through hydraulic fracturing) in order to attain economic gas flow rates.

Fracturing shales in place entails breaking shale along and across the bedding planes. Since gas shales and most rocks are weaker in tension than compression, practically all fractures across the bedding planes are caused by tension (Chong et al., 1984). Hence, ultimate tensile strengths are important for fracture studies.

The compressive strengths of the Mancos Shale formation have been reported (Torsaeter et al., 2012), however the tensile strength information is still lacking.

The tensile strengths across the bedding planes are relevant to vertical fracture studies with the tensile strengths between the bedding planes becoming increasingly important for horizontal fracture studies (Chong et al., 1984).

Traditionally, a Split Cylinder test (commonly referred to as a "Brazilian Test") has been used to measure the average (indirect) tensile strength across many bedding planes (yielding more representative information than direct tension testing (P.Chong et al., 1982)).

Conversely, uniaxial and biaxial (direct) tensile strengths have traditionally been used to determine the tensile strengths between bedding planes. Hence these strengths indicate the bonding strength between these planes. The early work by Youash (1969) showed how tensile strength is highly affected by the orientation of layering, with the tensile strength decreasing as failure occurs along layering.

Rocks with pronounced directional features such as lamination, foliation, and flow structure have anisotropic strength characteristics. Usually tensile strength perpendicular to bedding is less than tensile strength parallel to the bedding. However there is no guarantee that the tensile strength at an angle to bedding falls between the strengths parallel and perpendicular to bedding (Pariseau, 2011).

Nowadays, direct tensile strength tests on rock are seldom carried out due to the practical problems of applying tensile forces to a cylindrical rock specimen. Sometimes the direct tensile strength test will produce an eccentric force to a great extent, and destroy the specimen by torsion and not by pure tension (Keneti and Wong, 2010). By far the most common tensile strength test is the Brazilian test and its application has been increasingly applied to layered rocks (Chen et al., 1998a), (Keneti and Wong, 2010), (Vervoort et al., 2012), (Cho et al., 2012), (Quoc et al., 2013) (Park and Min, 2013).

3.1.2 The Brazilian Test

The Brazilian test is a simple testing method to obtain the tensile strength of brittle material such as concrete, rock, and rock like materials. In this test, a thin circular disc is diametrically compressed to failure.

The compression induces tensile stresses normal to the vertical diameter, which are essentially constant around the centre. The indirect tensile strength is typically calculated based on the assumption that failure occurs at the point of maximal tensile stress, i.e. at the centre of the disc (Li and Wong, 2012).

The suggested formula for calculating the splitting strength, σ_t (MPa) based on the Brazilian test is (ISRM, 1978).

$$\sigma_t = \frac{2P}{\pi Dt} = 0.636\frac{P}{Dt} \tag{3.1}$$

Where P is the load at failure (N), D is the diameter of the test specimen (mm) and t is the thickness of the test specimen measured at the centre (mm).

3.2 Experimental Procedure

The experimental procedure has been adapted from the standard method of ISRM (ISRM, 1978) and is discussed in full detail in Chapter 1. A summary of the procedure for Mancos Shale is given below;

3.2.1 Sample Preparation

Mancos Shale specimens were all disc shaped with a diameter of D=48 mm and a thickness t=24mm.

At the beginning of the Mancos sample preparations, cylindrical cores with a diameter of 48mm were drilled out of the larger rock blocks parallel to bedding. The cores were then cut into test specimens of suitable length and the end faces ground and hand polished (using Norton T489 Sheet P320 sandpaper). Afterwards, specimens were marked and measured predefined increments in relation to bedding planes (β = 0°, 15°, 30°, 45°, 60°, 75°, 90°) and stored in inert oil to avoid desiccation effects.

Samples were then either tested with the surfaces;

1. Dried with tissues and lightly spray painted (<30 minutes prior to testing)
2. Dried with tissues and main faces lightly sanded (<30 minutes prior to testing)
3. Coated in inert oil

3.2.2 Test Apparatus

The rock mechanics test system MTS 2/M was employed for the indirect tensile tests. MTS 2/M is a computer–controlled machine with a maximum load capacity of 10kN. The TestWorks–4 System Software was used to conduct computer controlled tests. The load and displacement were measured by the load cell.

3.2.3 Experimental Method

The Brazilian tests were carried out in accordance with the ISRM- recommendations (ISRM, 1978) for cylindrical samples with diameter D=48 mm and thickness to diameter ratio t/D=0.5. The experimental arrangement of for the Brazilian tests is illustrated in Figure 3.1 with samples placed with respect to the orientation of the bedding planes.

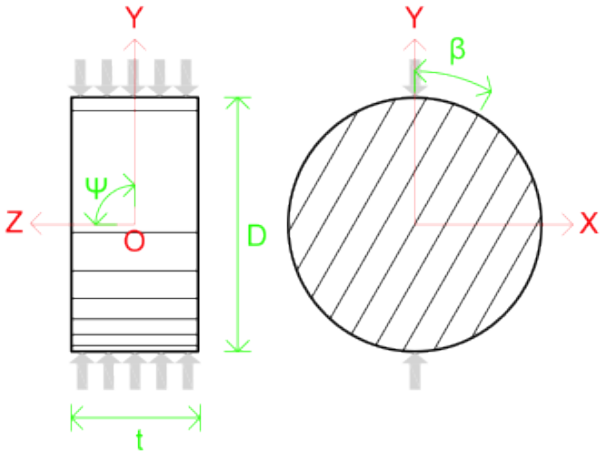

Figure 3.1: *Disc-shaped sample and configuration of layers in Brazilian tests. β varies between 0° and 90°. Set of inclined parallel lines symbolizes average layer direction (bedding). This setup has $\beta = 30°$ and $\psi = 90°$*

The disc was preloaded to 400N at a loading rate of 0.05mm/s. The test was then resumed and loaded up to failure with an unchanged loading rate of 0.003mm/s.

A total of 50 Brazilian tests were carried out. Mancos Shale: 35 specimens, Castlegate Sandstone: 4 specimens, Mons Chalk: 7 specimens, Pierre Shale: 4 specimens.

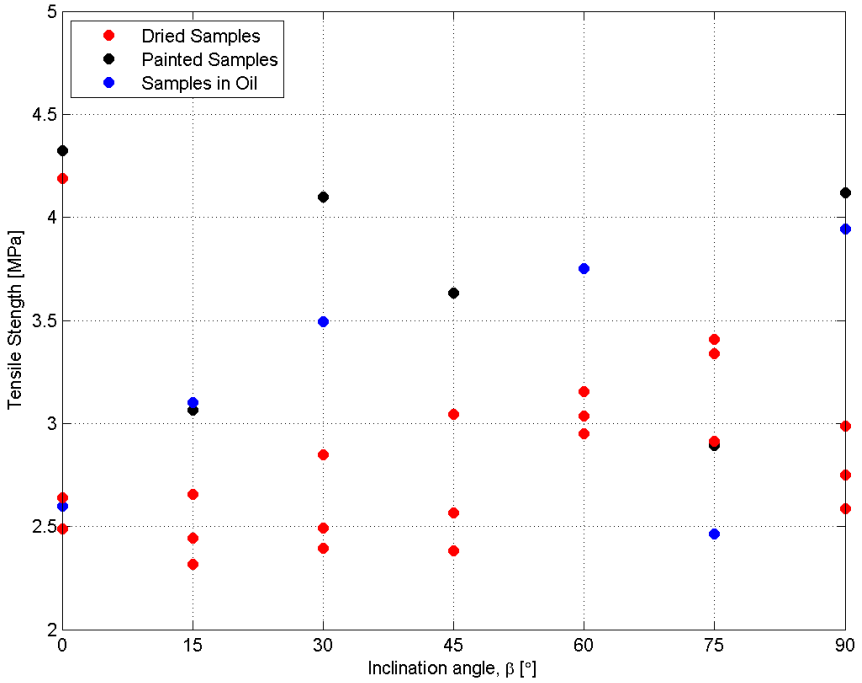

Figure 3.2: *Variation of the failure stress, with the inclination angle β for Mancos Shale*

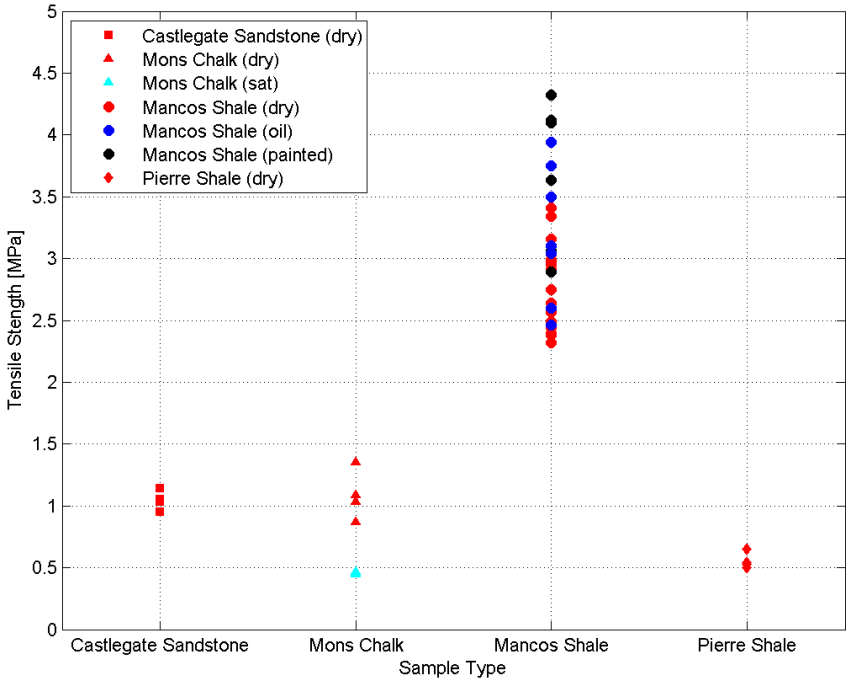

Figure 3.3: *Variation in the failure stress for different rock types*

3.3 Results and Observations

Lab tests were performed on four different rock types with different degrees of anisotropy: Mancos Shale, Castlegate Sandstone, Mons Chalk and Pierre Shale. A full summary of the results can be found in Appendix C.

Brazilian tests were carried out on Mancos Shale in order to determine the tensile strength in directions relative to bedding ranging from 0°to 90°(in incremental steps of 15°), as shown in Figure 3.2. For each orientation 3–5 samples were tested.

The laboratory tests have shown that the degree of anisotropy has a strong influence on the measured peak strength obtained in the Brazilian test. Whereas the orientation of the sample in relation to the loading direction is relatively unimportant for nearly isotropic materials (Figure 3.3), anisotropic materials like Mancos Shale suggest a dependence of the peak strength on the sample orientation in relation to the loading direction (Figure 3.2 and 3.3). These results have also been observed in related studies (Chen et al., 1998a), (Keneti and Wong, 2010), (Vervoort et al., 2012), (Cho et al., 2012), (Quoc et al., 2013).

Table C.1 and C.2 shows the mean value of the tensile strength as a function of the orientation of anisotropy. Of interest is the variation in results that is characterized by the coefficient of variation (standard deviation as a percentage of the mean). A coefficient of variation of 40% is not unusual and seems to be an intrinsic characteristic of rock (Pariseau, 2011). The standard deviation of the mean is obtained by division of the data standard deviation by the square root of the number of tests. To reduce the standard deviation associated with tensile strength, say by 50 %, a quadrupling of test numbers would be required, other factors remaining the same (Pariseau, 2011).

3.4 Discussion

Figure 3.2 suggests that tensile strength for Mancos Shale is changed when the surface environment of the sample is modified. Tensile strength measurements appear to be higher for (painted) samples followed by the (oil) samples and finally the (dry) samples. These findings may be explained through a study by Knudsen et al. (2007) that revealed that that the paint thickness may have a significant effect of the internal stresses of a material. The behaviour of the internal stress is dependant on the type and thickness of coating applied (Knudsen et al., 2007). The results of this study indicate that the application of a thin paint layer increases the tensile strength of the Mancos Shale, possibly due to the change in internal stresses within the sample. It is important that future research attempts to quantify these effects further so to have a better understanding of how sample preparation may affect the calculated tensile strengths when using the Brazilian Test. These findings may also be of interest to borehole stability related reasearch.

Many studies have investigated relationship between Unconfined Compressive Strength (UCS) and Tensile Strength (TS) values. Therefore, it is logical to compare the TS values determined in this study with the UCS values as presented by (Torsaeter et al., 2012) (Figure3.4).

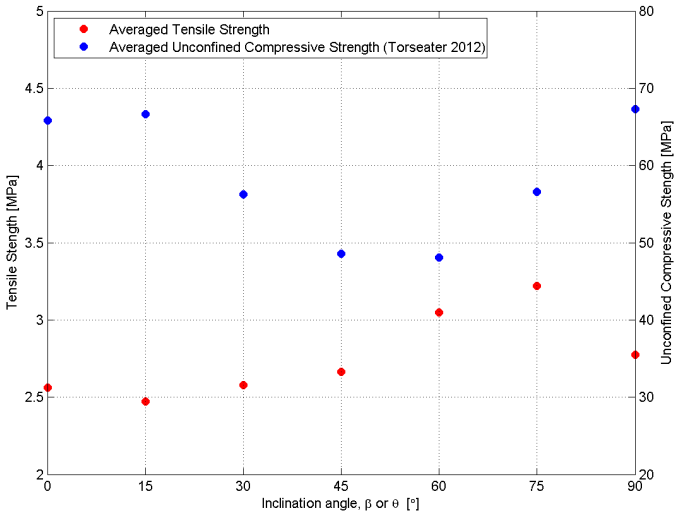

Figure 3.4: *Averaged TS and UCS vs inclination angle for Mancos Shale*

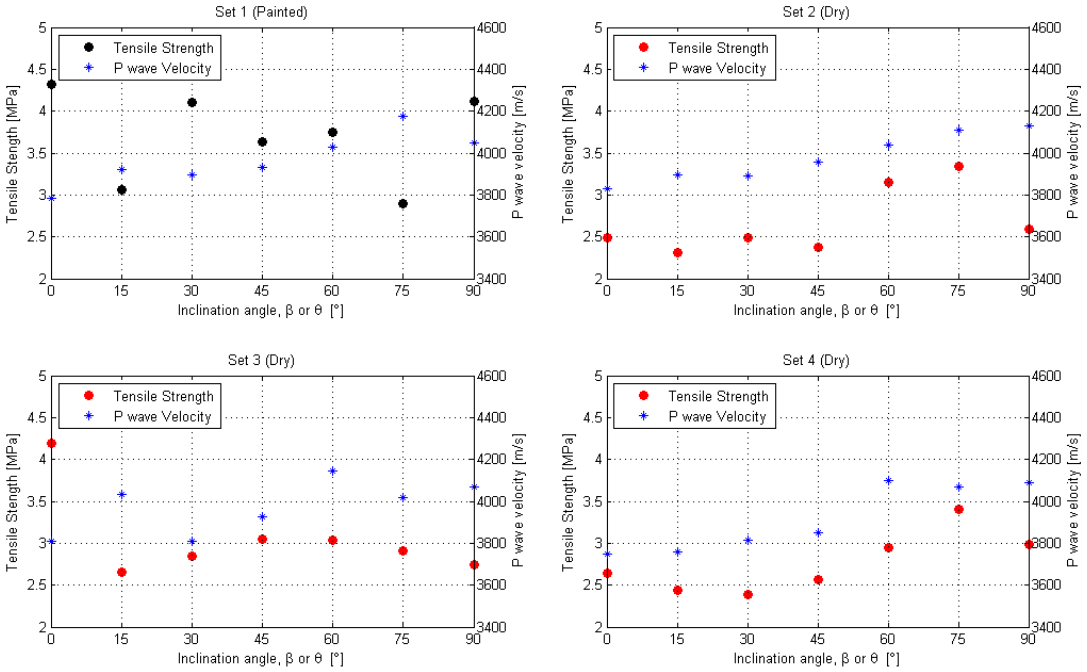

Figure 3.5: *Variation in the failure stress for different rock types*

Both UCS and TS values appear to have an angular dependence on bedding direction, however they do not display similar strength trends in relation to the bedding inclination angle. This may be attributed to the different stress distributions within samples when loaded with an alternate configuration (Figure 1.5). In a related study by Park and Min (2013) they present data trends (for TS and UCS) similar to what is displayed for Mancos Shale in this report.

The variation of the ultimate tensile strength, with the inclination angle β is plotted in Figure 3.2.

Figure 3.2 presents the variation in upper and lower limits of TS for Mancos Shale as a function of the inclination angle. This figure suggests that by decreasing the inclination angle a slight decrease in tensile strength of Mancos Shale results. The failure strength reaches a maximum when $\beta = 75°$, which seems to be consistent with the experimental results of Chen et al. (1998a) and Barla (1974) on sandstone and schist respectively. The minimum failure strength occurs when $\beta = 15°$for Mancos Shale. This trend could be expected, because when the layers are horizontal or semi-horizontal i.e. $90° \leq \beta \leq 60°$, the fracture propagates mainly through the stronger material, while by decreasing the inclination angle the fracturing processes make use of the layers, of which one could expect that they have weaker mechanical properties (Vervoort et al., 2012). It is important to note that the maximum and minimum tensile strengths do not necessarily occur when $\beta = 90°$ and $0°$ respectively.

Also it is possible that for lower values of β, sample failure incorporates a component of shear and does not occur in pure tension. An analysis of the fracture patterns (described in Section 6.3.3) assists in illustrating where tension and shear failure has occurred.

Figure 3.5 was created to investigate whether the variation in tensile strength could also be observed for the acoustic p-wave velocity measurements. However, the acoustic emission measurements did not seem to align with the variations observed in the calculated tensile strengths.

3.5 Conclusion

This Chapter investigated the effects of bedding angle on the ultimate tensile strength of an anisotropic rock (Mancos Shale) using the Brazilian test. The laboratory tests showed that the degree of anisotropy had an influence on the measured peak strength, decreasing slightly with decreasing bedding angles, whereas the orientation of the sample in relation to the loading direction was relatively unimportant for nearly isotropic materials.

The results from this study also suggest that the application of a thin paint layer increases the peak strength of Mancos Shale, possibly due to the change in internal stresses within the sample. It is important that future research aim to quantify these effects further so to have a better understanding of how sample preparation may affect the calculated tensile strengths when using the Brazilian test. These findings may also be of interest to borehole stability related reasearch.

The indirect tensile strength is typically calculated based on the assumption that failure occurs at the point of maximal stress, i.e. at the centre of the disc (Chapter 4).

Chapter 4

Stress Distribution

Nathaniel Simpson

Literature Review on *The Stress Distribution within a Brazilian Disc Sample*

Summary

The stress distribution (normal and shear) differs between isotropic and anisotropic materials. Having an understanding of the stress distributions within the Brazilian disc for the isotropic and anisotropic case are important for understanding the differences in behaviour for the two systems. The calculation of the stress fields of anisotropic rock is possible with the use of the principle elastic constants. This chapter presents the (dimensionless) principle stress fields in diagrams for both isotropic and anisotropic cases.

4.1 Introduction

4.1.1 Objective

A rock fails when the stress exceeds a certain limit, while it remains intact as long as the stress is lower than this limit. The Griffith Theory assumes that fracture initiation is governed by when the maximum tensile stress (σ_3) is equal to the tensile strength of the material (σ_t). This criterion is used together with the specimen dimensions in order to calculate (indirect) tensile strength (Colback, 1966).

The stress distribution (normal and shear) differs between isotropic and anisotropic materials. The objective of this chapter is to provide an insight into the directional stresses that may exist within the two types of Brazilian disc specimens.

4.1.2 Stress

Stress (σ) can be defined as the load per unit area or the force (F) applied per cross sectional area (A) perpendicular to the force as shown in Equation 4.1 below (E. Fjaer et al., 2008);

$$Stress = \sigma = \frac{F}{A} \tag{4.1}$$

Where, σ = stress (Pa), F = applied Force (N), A = cross-sectional area (m^2)

The stress level at which a rock typically fails is commonly called the strength of the rock. The term Ultimate Tensile Strength (UTS) is often used to designate this point.

4.1.3 The Brazilian Test

Consider a thin cylindrical disc of a linearly elastic, homogeneous, continuous, and transversely isotropic medium with the geometry shown in (Figure 4.1). The disc has a thickness, t, and a diameter, D, and a load (force), P applied in the y direction, i.e. a static Brazilian test.

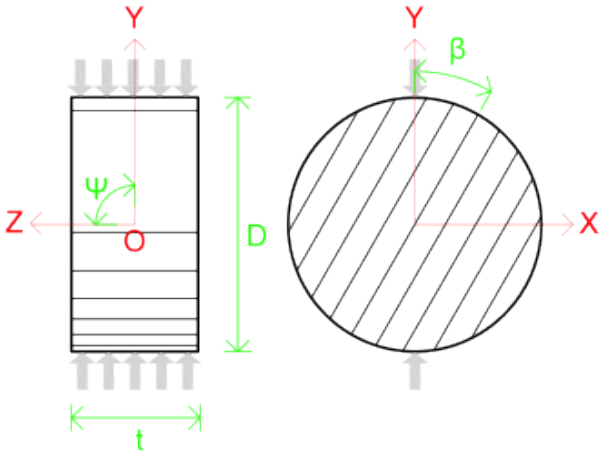

Figure 4.1: *Disc-shaped sample and configuration of layers in Brazilian tests. β varies between 0° and 90°. Set of inclined parallel lines symbolizes average layer direction (bedding). This setup has $\beta = 30°$ and $\psi = 90°$*

Let x, y, z be a global Cartesian coordinate system with the z-axis defining the longitudinal axis of the disc. The surface forces are assumed to be in equilibrium. The angle β is defined as the inclination angle between the loading direction (y) and bedding (on the x-y plane). The angle ψ is defined as the inclination angle between the loading direction (y) and bedding (on the z-y plane).

In the test, a thin circular disc is diametrically compressed until failure. The loading scheme induces normal (σ) and shear (τ) stresses (assuming that the vectors all lay within the x-y plane i.e. there is negligible principal stress is oriented in the z-direction). Note: By sign convention compressive stresses have been classified as positive (E. Fjaer et al., 2008).

4.2 Mohr's Circle

The normal and shear stresses, σ_x, σ_y, and τ_{xy}, can be expressed relative to the coordinates XY, as shown in Figure 4.2 below.

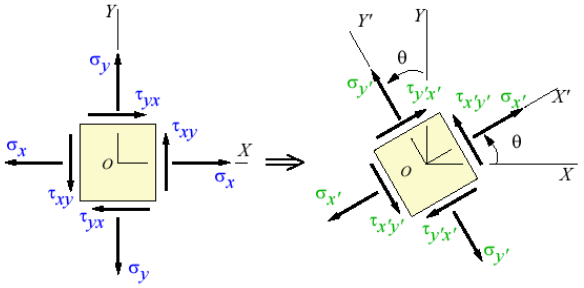

Figure 4.2: *Stresses at given coordinate system (left) and Stresses transformed to another coordinate system (right). Source (Efunda, 2013)*

With the use of Mohr's Circle stresses from one coordinate set can be transformed to another. Mohr's Circle illustrates principal stresses and stress transformations via a graphical format. The two principal stresses are shown in red, and the maximum shear stress is shown in orange. Recall that the normal stresses equal the principal stresses when the stress element is aligned with the principal directions, and the shear stress equals the maximum shear stress when the stress element is rotated 45°away from the principal directions (Efunda, 2013).

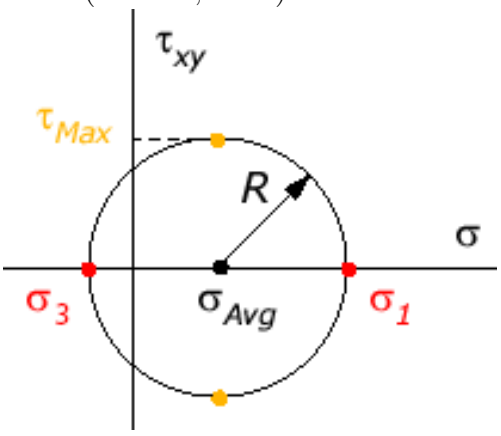

Figure 4.3: *Mohr's Circle. Source (Efunda, 2013)*

As the stress element is rotated away from the principal (or maximum shear) directions, the normal and shear stress components will always lie on Mohr's Circle (Efunda, 2013).

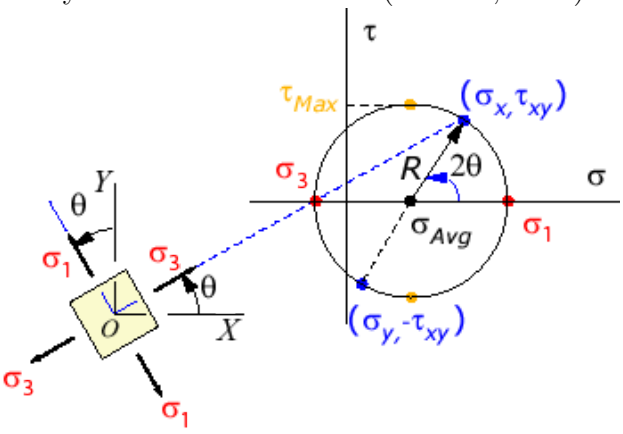

Figure 4.4: *Isotropic rocks with a vertical (left) and horizontal (right). Source (Efunda, 2013)*

Given the stress components σ_x, σ_y, and τ_{xy}, Mohr's Circle can be used to compute the principal stresses σ_1 (compressive), σ_3 (tensile), the principal angle θ, and the maximum shear stress τ_{max} using the equations below (Efunda, 2013).

$$\tan 2\theta = \frac{2\tau_{xy}}{\sigma_x - \sigma_y} \tag{4.2}$$

$$\sigma_{max} = \sigma_1 = \frac{\sigma_x + \sigma_y}{2} + \sqrt{\left(\frac{\sigma_x - \sigma_y}{2}\right)^2 + {\tau_{xy}}^2} \tag{4.3}$$

$$\sigma_{min} = \sigma_3 = \frac{\sigma_x + \sigma_y}{2} + \sqrt{\left(\frac{\sigma_x - \sigma_y}{2}\right)^2 - {\tau_{xy}}^2} \tag{4.4}$$

$$\tau_{max} = \sqrt{\left(\frac{\sigma_x - \sigma_y}{2}\right)^2 + {\tau_{xy}}^2} = \frac{\sigma_1 - \sigma_3}{2} \tag{4.5}$$

4.3 Brazilian Disc Stress Fields

4.3.1 Analytical Stress Fields

Analytical solutions for anisotropic discs subject to the Brazilian test have been presented in the literature by various authors (Lekhnitskii, 1968)(Amadei et al., 1983) (Chen et al., 1998a) (Chen et al., 1998b) (Claesson and Bohloli, 2002). The calculation of the stress and tensile strength of the anisotropic rock sample requires the principle elastic constants E, E', v, v' and G' to be determined ($v/E = v'/E'$).

With the assumptions that; the disc has a plane of elastic symmetry parallel to its middle plane, it is loaded by surface forces that vary negligibly across its thickness and that deformation of the disc is small, then it is possible to use a computer program to determine the stresses at any arbitrary point in a disc of transversely isotropic medium under diametral loading.

The study by Chen et al. (1998a) presents the principle stress fields in diagrams at the centre of the disc for both isotropic and anisotropic cases.

4.3.2 Isotropic Stress Components

Figure 4.7 (a-c) show respectively the distribution of the dimensionless stress components $\sigma_x/(P/\pi Dt)$, $\sigma_y/(P/\pi Dt)$ and $\tau_{xy}/(P/\pi Dt)$ over the disc surface for the isotropic case. In this case, $E/E' = 1$, $v' = v = 0.25$ and $E/G' = E/G = 2(1+v) = 2.5$ (Chen et al., 1998a).

This distribution is also presented in Figure 4.5 where ($\sigma_y = \sigma_1$) and ($\sigma_x = \sigma_3$) for the Isotropic Case. Figure 4.5 shows the comparison of normalized principal stresses along the middle part of the compressed diametral line (Colback, 1966).

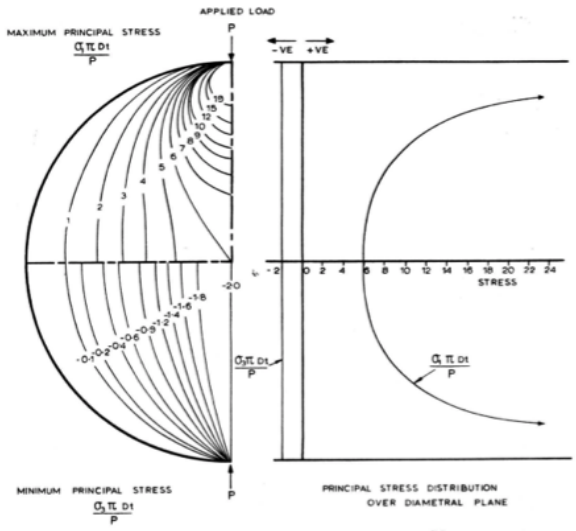

Figure 4.5: *Theoretical stress distribution in a disc subjected to diametral compressive point load P. Source (Colback, 1966)*

It is interesting to also note that a study by Yu et al. (2006) revealed that the tensile stress distribution ($\sigma_3 \pi Dt/P$) is different on the surface to the middle of the specimen, whereas the compressive stress distribution ($\sigma_1 \pi Dt/P$) is almost the same on the two planes (Figure 4.6).

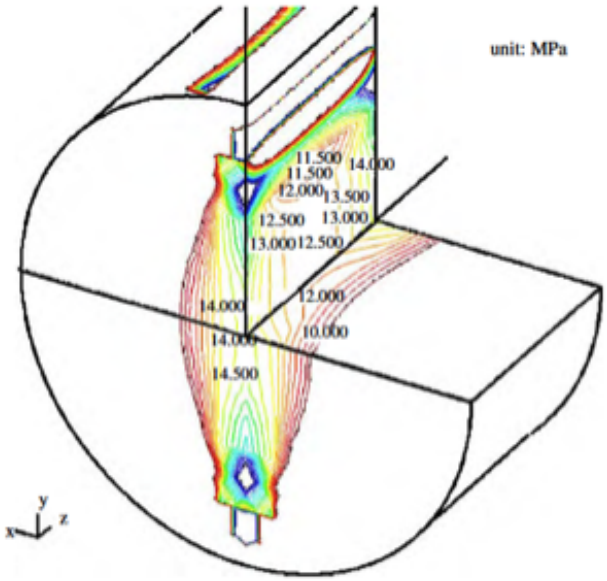

Figure 4.6: *x-axial tensile stress distribution in a specimen whose ratio is 0.5. Source (Yu et al., 2006)*

4.3.3 Anisotropic Stress Components

Figure 4.8 (a-c) show respectively the distribution of the dimensionless stress components $\sigma_x/(P/\pi Dt)$, $\sigma_y/(P/\pi Dt)$ and $\tau_{xy}/(P/\pi Dt)$ over the disc surface for the anisotropic (transversely isotropic) case with an angle of $\beta = 45°$. In this case, $E/E' = 3, v' = 0.25$ and $E/G' = 7.5$ (Chen et al., 1998a).

4.3.4 Principle Stresses

Figure 4.9 (a-c) show the contours of dimensionless in-plane principal stresses $\sigma_1/(P/\pi Dt)$ and $\sigma_3/(P/\pi Dt)$ (with $(\sigma_1 > \sigma_3)$ for $\beta = 0°$, $\beta = 45°$, $\beta = 90°$ (Chen et al., 1998a).

4.4 Discussion and Conclusions

Having an understanding of the stress distributions within the Brazilian disc for the isotropic and anisotropic case are important for understanding the differences in behaviour for the two systems.

Several conclusions can be drawn from the stress distributions as presented in Figures 4.7, 4.8 and 4.9 (Chen et al., 1998a).

1. The anisotropic nature and the angle of β strongly effects the nature and magnitude of the stresses in the disc.

2. The stress distributions indicate that for points along the loaded diameter;

   (a) σ_x is tensile and generally constant,

   (b) σ_y is compressive and varies along the diameter and

   (c) τ_{xy} is not zero (unless $\beta = 0°$ or $90°$).

3. The nonvanishing character of τ_{xy} implies that, the principle stress contours are not symmetric with respect to the x and y axes except when $\tau_{xy} = 0°$ and $90°$.

4. The maximum tensile stress (max σ_3) is located at the centre of the disc. This indicates that the initiation of fracture during diametral loading will be at the centre of the disc if a fracture criterion of maximum principal stress is adopted.

Investigation of fracture initiation is examined further in Chapter 5 with the use of a high speed camera and an acoustic emission system.

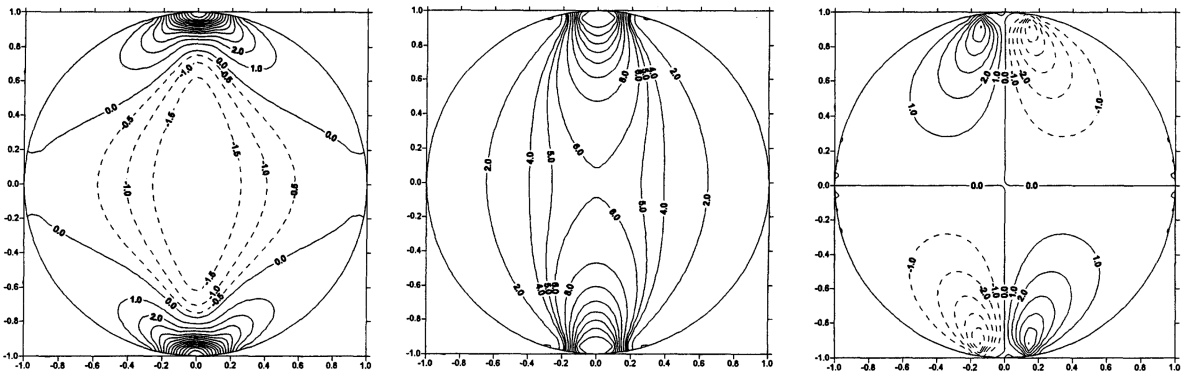

(a) $\sigma_x/(P/\pi Dt)$ (b) $\sigma_y/(P/\pi Dt)$ (c) $\tau_{xy}/(P/\pi Dt)$

Figure 4.7: *Distribution of Stresses in (a), (b) and (c) respectively. Isotropic Case. Source (Chen et al., 1998a)*

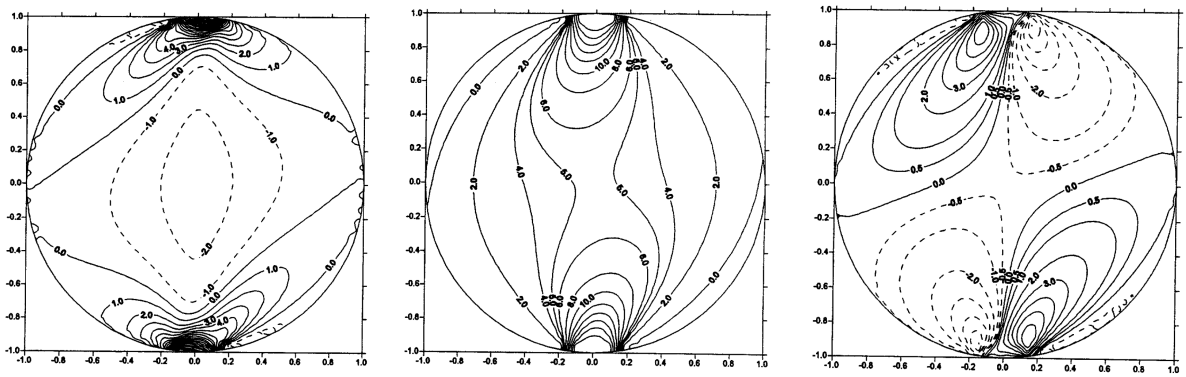

(a) $\sigma_x/(P/\pi Dt)$ (b) $\sigma_y/(P/\pi Dt)$ (c) $\tau_{xy}/(P/\pi Dt)$

Figure 4.8: *Distribution of Stresses in (a), (b) and (c) respectively. Anisotropic (transversely isotropic) Case. Source (Chen et al., 1998a)*

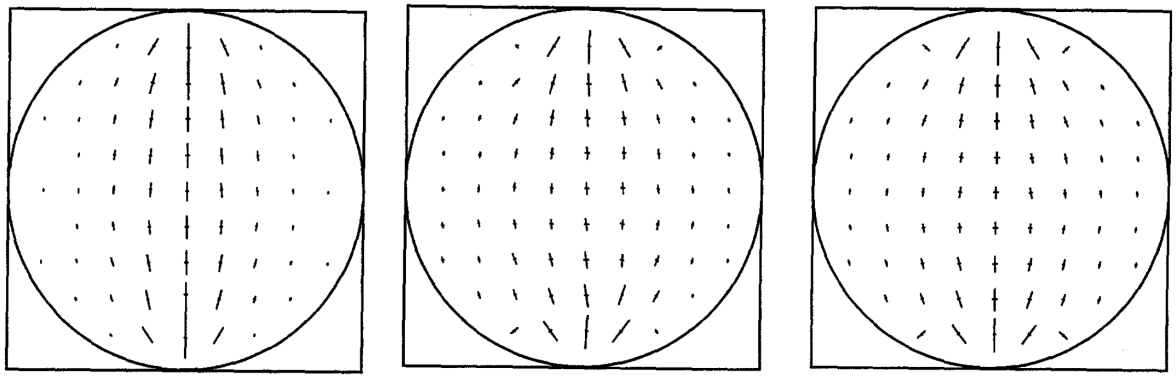

(a) $\beta = 0°$ (b) $\beta = 45°$ (c) $\beta = 90°$

Figure 4.9: *Distribution of dimentionless principle stresses $\sigma_1/(P/\pi Dt)$ and $\sigma_3/(P/\pi Dt)$ (with $(\sigma_1 > \sigma_3)$. Source (Chen et al., 1998a)*

Chapter 5

Fracture Initiation

Nathaniel Simpson

Experimental Observations on *The Fracture Initiation Point of Mancos Shale during the Brazilian Test*

Summary

This chapter investigates the time and location of fracture initiation of an anisotropic material (Mancos Shale) using a synchronised data collection system. A MTS Load Cell and a Phantom high speed camera to are connected a Vallen Acoustic System (using analog channels). Measurements of displacements on the surface of the sample and calculations of strain fields using a DIC method suggest that the first fracture predominantly initiates in the middle area of the sample (even with the existence of minor preexisting cracks). These observations suggest that the strain criterion may therefor not be applicable for Mancos Shale. In this study it was discovered that a time shift exists between the time of ultimate tensile stress and the time of fracture initiation for Mancos Shale. This phenomenon has been dubbed the Naet Shift. Naet shift values may be approximated using data obtained from the traditional Brazilian testing methods.

5.1 Introduction

5.1.1 Objective

Fracture initiation (FI) is the least studied and most uncertain stage of fracture phenomena (Jasarevic et al., 2009). Researchers have long been curious to know where the first crack initiates and how it propagates (Li and Wong, 2012). The objective of this chapter is to determine the time and location of fracture initiation of an anisotropic material (Mancos Shale) at various angles during diametric loading.

5.1.2 Griffith's brittle fracture theory

The indirect tensile strength of a disc sample may be calculated by equation 3.1. The theoretical calculation is based on Griffith's brittle fracture theory with the assumption that the rock material is linearly elastic and homogeneous (i.e. isotropic). Failure starts as a result of tensile stress induced at the tips of inherent cracks or discontinuities orientated at a critical angle to the applied stresses (Colback, 1966).

Theoretically, according to the Griffith criterion, the exact centre of the disc is the only crack initiation point at which the condition for tensile failure at a value equal to the uniaxial strength are met (Li and Wong, 2012).

As was shown in Chapter 4, the maximum principle stress (in both isotropic and anisotropic materials) occurs at the centre of the disc, which means that in order to satisfy the fracture criterion, the initiation of fracture during diametral loading needs to also be at the centre of the disc. It is perceived by some that if the fracture does not initiate in this manner then the test is regarded as exhibiting an invalid failure mode (Fairhurst, 1964).

In general, the original Griffith theory strictly refers to the local tensile failure process. i.e. where fracture initiation, fracture propagation and crack coalescence take place almost instantaneously (Whittaker et al., 1992).

Griffith postulated that typical brittle materials inevitably contain numerous sub microscopic flaws, micro cracks or other discontinuities of heterogeneity, which are distributed in some random orientation throughout the volume of the material. These flaws or cracks are too small to be detected by ordinary means and they serve as stress concentrators and as a consequence fracture initiation is caused by the stress concentrations at the ends of these minute internal cracks (Whittaker et al., 1992).

Failure of a stressed brittle solid involves the two necessary requirements (Whittaker et al., 1992)

- **Stress requirement:** at some point in the solid, the local stress must be high enough to overcome the molecular cohesive strength of the solid. This can be achieved by the stress concentration due to the presence of discontinuities such as pre-existing (Griffith) micro cracks.

- **Energy requirement:** sufficient potential energy must be released to overcome the resistance to crack extension (i.e. surface energy): this can be achieved through increasing the work done by external forces.

5.1.3 Mixed Observations

Based on the stress analysis of the Brazilian disc (Chapter 4) various authors (Chen et al., 2004) (Yanagidani et al., 1978) have shown that the failure of the Brazilian disc begins as an extension fracture in the centre (interior) of the disc and then propagates to the top and bottom surfaces.

However in some laboratory Brazilian tests, the crack initiation points have been observed to be located away from the centre of the test disc (Fairhurst, 1964) (Hooper, 1971) (Hudson et al., 1972) (Swab et al., 2011).

In addition, the stress concentration near the loading platen has shown to occasionally lead to an early shear failure fracture of the rock (Fairhurst, 1964) (Hudson et al., 1972).

Yue et al. (2003) used a Finite Element Modelling method to show the effect of material inhomogeneity on the tensile stress distribution along the vertical loading diameter during a typical Brazilian test.

5.1.4 Experimental Methods

Fracture patterns through the generation of a central dimetral crack provide no "real time" information regarding the crack initiation process. For anisotropic samples when the bedding is inclined to the load axis, i.e. $0° < \beta < 90°$ the fracture initiation between the load points is uncertain (Quoc et al., 2013).

For many years, acoustic emission (AE) monitoring techniques have been used in order to detect the processes that accompany fracture initiation in isotropic material (Jasarevic et al., 2009).

In addition, conventional video cameras have been used in some studies to observe fracturing effects (Debecker and Vervoort, 2009), however depending on the rock type, conventional video (25-100 frames /second) is not sufficient to monitor in detail the FI point and fracture growth (Jasarevic et al., 2009).

In this chapter the fracture initiation point for anisotropic material (Mancos Shale) was captured through the use of a high–speed camera (filmed at 5000 frames per second) and a mounted acoustic emission set up on the rear side of the sample.

5.2 Experimental Procedure

5.2.1 Brazilian Test

The disc specimens were inserted into a test frame (MTS 2/M) and the load applied along the diameter at a displacement rate of 0.003mm/s using (a Brazilian frame with curved loading jaws). A piece of masking tape was placed between the specimen and load platens to reduce friction and promote a uniform stress distribution along the contact surface.

5.2.2 Acoustic Emission

Acoustic Emission (AE) was measured using an AMSY-5 System by Vallen GmbH. Each signal was amplified by a preamplifier with an amplification of 34 dB. Four wide band sensors were used of type B1025 (Digital Wave Corp., USA), which have a radius of 4.5mm and a frequency range from 50kHz to 2MHz. The minimum threshold to measure signals was set to 23.8dB. The Disc specimens were first pre loaded to 400 N using the MTS frame. The sensors were then mounted on the rear side of the disc specimen in a square configuration 20mm apart using a custom made sensor holder and the sensor thresholds tested. The disc was then loaded until failure, and acoustic events (hits) stored within the acoustic system. A location map was generated using Vallen Software (assuming an isotropic medium and using the central p-wave acoustic velocity (C) as measured in Chapter 2).

5.2.3 High Speed Camera

The Digital Image Correlation (DIC) method was used to assess the local displacement and strain fields at the sample surface with "7D" correlation software (Vacher et al., 1999). Digital images were recorded during the deformation process at a rate of 5,000 frames per second using a Phantom v12 high speed camera and PCC software (Vision Research). The camera's memory can store approximately 4 seconds of footage after it is manually triggered (in this case, after the main fracture).The image resolution was set to 704×704 pixels with an exposure time of 190μs. For each test, the initial image was split in square elements to create a virtual grid upon the sample surface. The resolution of this grid (extensiometric base) was set to 10×10 pixels. The correlation process consists in looking for the most probable deformed pattern in the neighbourhood of each node of this grid in terms of colour level. The displacement fields of each element are then assessed by the means of a bi-linear interpolation and the strain field calculated using Green-Lagrange's tensor (E) (Vacher et al., 1999).

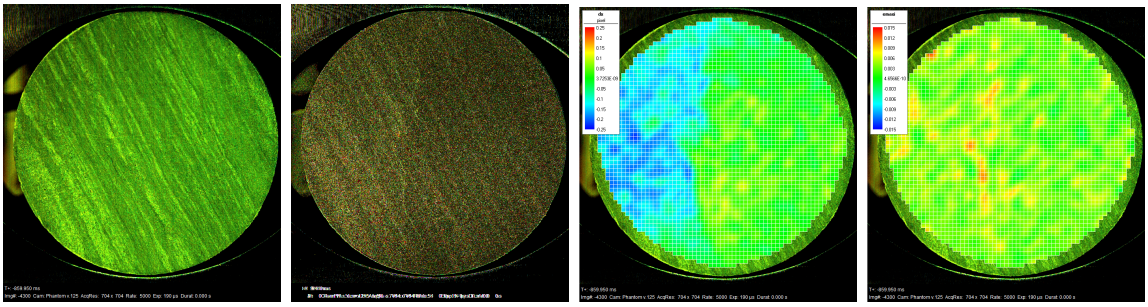

(a) Original image (b) Image subtracted (c) x–displacement (d) Strain tensor (E)

Figure 5.1: *Fracture Initiation point in (a), (b), (c) and (d) for Mancos Shale (dry)* $\beta = 30°$. *(c) scale:* $-0.25 < \Delta p < 0.25$ *with 1 pixel* $(p) = 0.071mm$, *(d) scale:* $-0.015 < E_{maxi} < 0.015$

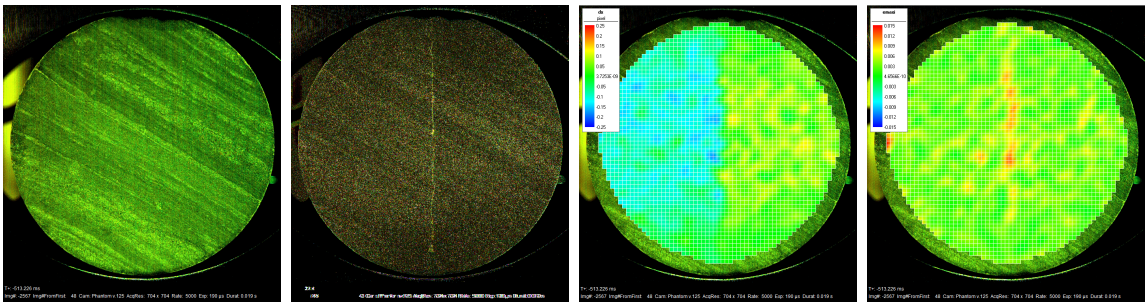

(a) Original image (b) Image subtracted (c) x–displacement (d) Strain tensor (E)

Figure 5.2: *Fracture Initiation point in (a), (b), (c) and (d) for Mancos Shale (dry)* $\beta = 60°$. *(c) scale:* $-0.25 < \Delta p < 0.25$ *with 1 pixel* $(p) = 0.072mm$, *(d) scale:* $-0.015 < E_{maxi} < 0.015$

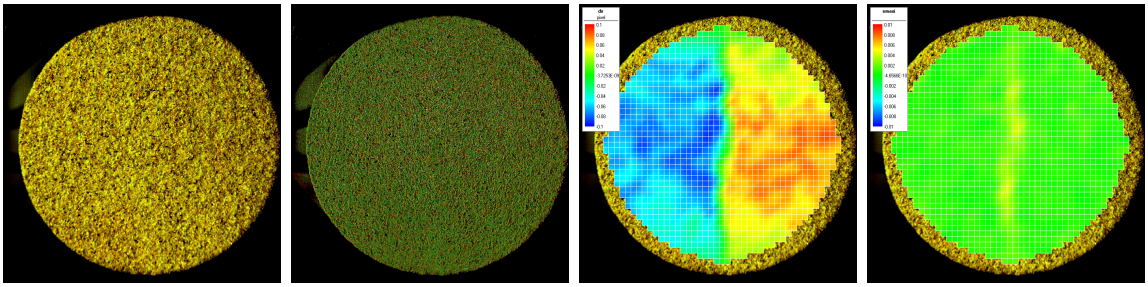

(a) Original image (b) Image subtracted (c) x–displacement (d) Strain tensor (E)

Figure 5.3: *Fracture Initiation point in (a), (b), (c) and (d) for Castlegate Sandstone (dry). (c) scale:* $-0.1 < \Delta p < 0.1$ *with 1 pixel* $(p) = 0.073mm$, *(d) scale:* $-0.01 < E_{maxi} < 0.01$

5.3 Results and Discussion

5.3.1 Fracture Initiation Location

Measurements of displacements on the surface of the sample and calculations of strain fields were performed from the image processing software "7D" whose principle is based on a DIC method (Vacher et al., 1999).

Figures 5.1 to 5.3 display images of Mancos Shale and Castlegate sandstone at the time of initial fracture. The images shown include; the original image, a subtracted image, the x–displacement and the maximum Green-LaGrange's strain tensor (E_{maxi}). A full set of fracture initiation images of Mancos Shale for each bedding angle (β) is also given in Appendix D.

The results from these images suggest that the crack initiates in the middle region for all specimens. A displacement and strain analysis was conducted using the high–speed images of the specimen and tracking the changes in pixel orientation. Images from this test confirm that the highest strains occur in the centre region where the fracture initiates.

Note: there is difficulty using only the original image or the subtracted image to locate the initial fracture point. The DIC software is particularly useful in such a situation.

5.3.2 The Strain Criterion

According to a model presented by Mahabadi et al. (2009) the following observations are expected for layered rocks;

- Similar to the homogeneous rock, the failure mechanism for $\beta = 0°$ and $90°$ is tensile. Cracks initiate at the centre of the disc and propagate towards the loading platens.
- In contrast, for $\beta = 30°$ firstly shear failure occurs at the interface between layers near the platen where high shear stresses are developed, Figure 5.4. This is because, compared to the intact rock material, the layer interfaces have a much lower shear strength.

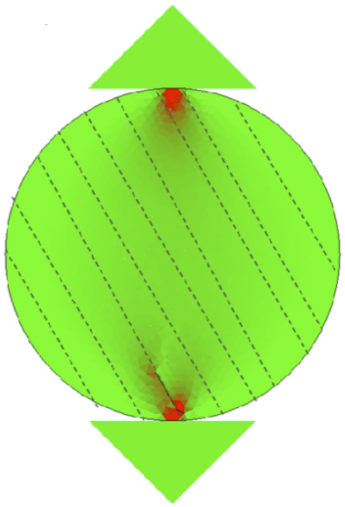

Figure 5.4: *Modelled fracture initiation for* $\beta = 30°$. *Source (Mahabadi et al., 2009)*

This modelled failure mode is linked to the theoretical strain criterion. The local strain criterion associates the first crack initiation position near the loading points, instead of at the centre of the specimen where the maximum extension strain criterion is satisfied.

Li and Wong (2012) mention that investigating the suitability of the strain criterion in modelling 3D crack initiation and propagation of a Brazilian rock disc is an important research task for the future.

The images displayed in Figure 5.5 display three Mancos Shale specimens at $\beta = 30°$ during the time of the first crack appearing. If the greatest values of dx signify the origin for where the first fracture originates, then the results suggest that the strain criterion is not applicable for Mancos Shale.

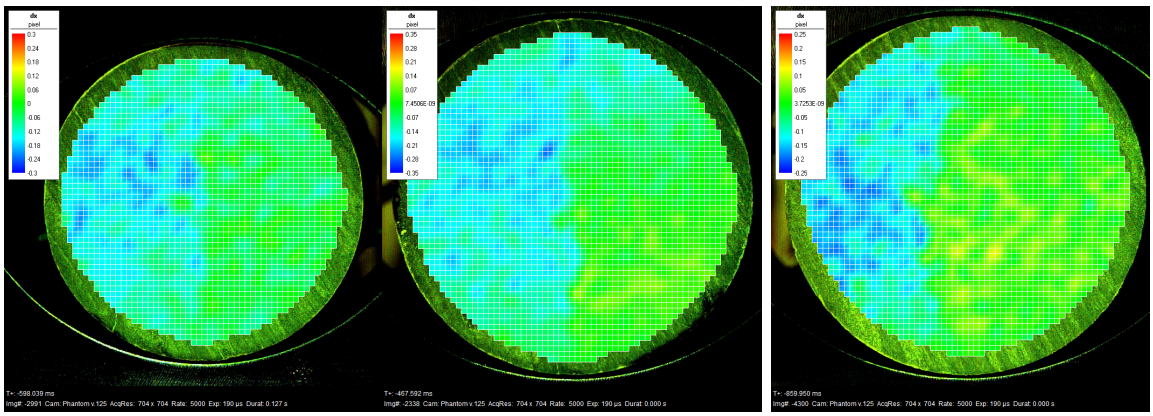

(a) Set 2 $\beta = 30°$ (b) Set 3 $\beta = 30°$ (c) Set 4 $\beta = 30°$

Figure 5.5: *Fracture Initiation point for* $\beta = 30°$ *from three Mancos Shale (dry) samples*

5.3.3 Pre Existing Cracks

The existence of pre existing cracks on certain samples was evident through the presence of oil in the sample during testing. The inert oil appears as a black mark when using the high–speed camera. It is interesting to note that although a few samples contained cracks of various size and positions, the fracture predominately still initiated in the middle area of the sample (as shown in Figure E.21). This supports the assumption that tensile stress is the governing force responsible for fracture initiation during Brazilian testing.

5.3.4 Fracture Initiation Time

The fracture initiation point of interest for this study refers to the local tensile failure process. i.e. where fracture initiation, fracture propagation and crack coalescence take place almost instantaneously. Given the interlinked experimental system, it was possible to determine the time at which fracture initiation starts. Based on the stress analysis (Chapter 4) one might expect fracture initiation to occur at the time of maximal stress, however it was determined that this is not necessarily the case.

A synchronised data collection system was created by connecting a MTS Load Cell and a Phantom high speed camera to a Vallen Acoustic System (using analog channels). This allowed data to be collected at approximately 0.01 second intervals and stored to four decimal places.

Figure 5.6 shows the plots of the applied Load and Acoustic Hits versus Time. Each crack event acts as an impulsive force that causes elastic vibrations of the specimen. During nucleation and growth of micro cracks, high-frequency acoustic emissions (AE) are observable (and recorded as Hits) (Schiavi et al., 2011). Assuming that the highest number of events occurs around time of fracture, then the results suggests that the maximum Load (Stress) occurs prior to fracture initiation. This observation is again supported by high–speed video footage Figure E.21.

A complete set of fracture initiation plots and images (similar to Figures 5.6–5.8) may be located in Appendix E.

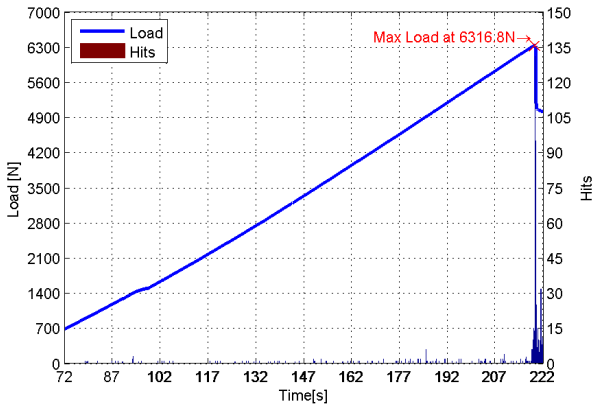

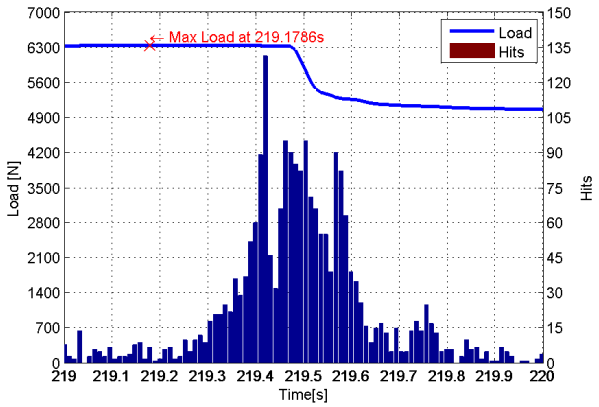

Figure 5.6: *The measured time of Ultimate tensile stress has been defined as the point at maximum Load occurs on the Load vs Time curve (this is marked by a red cross)*

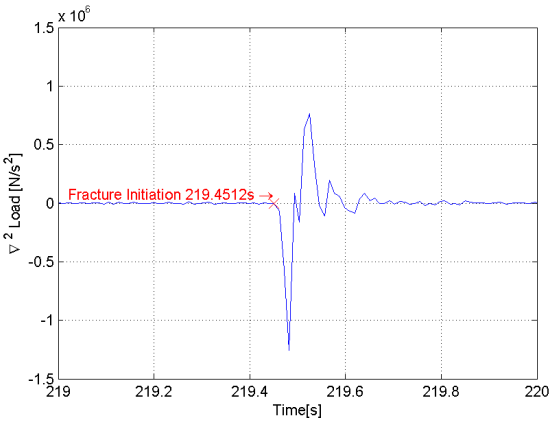

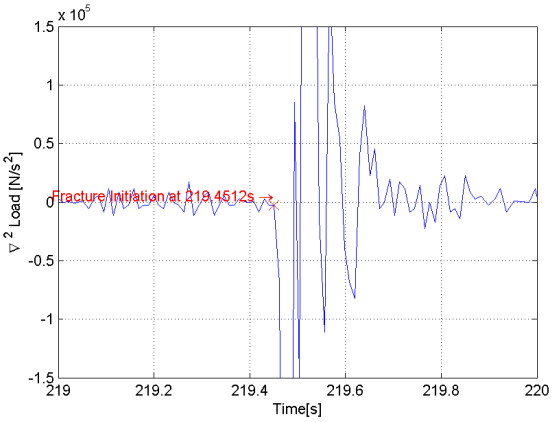

Figure 5.7: *The approximated time at FI may be calculated by the first point at which significant deviation occurs on the $\nabla^2 Load$ vs Time curve (this is marked by a red cross)*

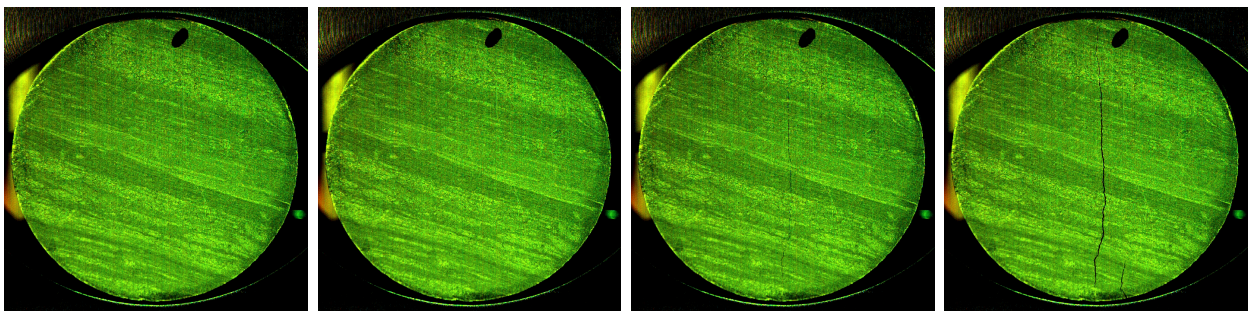

(a) UTS (b) Measured FI (c) Observed Fracture (d) 0.01s after (b)

Figure 5.8: *High speed images taken at (a) Measured Ultimate tensile strength (b) the measured fracture initiation point (c) the observed fracture initiation point and (d) Approx 0.01 s (i.e. the next recorded time value) after (b)*

Further investigation into this phenomenon reveals that fracture initiation may be approximated by using the second derivative of the Load vs Time plot (Figure 5.7). The $\bigtriangledown^2 Load$ vs $Time$ plot may be created using the mathematical relations below.

$$\bigtriangledown Load_{(i)}[N/s] = \frac{Load_{(i+1)} - Load_{(i)}}{Time_{(i+1)} - Time_{(i)}} \quad (5.1)$$

$$avTime_{(i)}[s] = \frac{Time_{(i+1)} + Time_{(i)}}{2} \quad (5.2)$$

$$\bigtriangledown^2 Load_{(i)}[N/s] = \frac{\bigtriangledown Load_{(i+1)} - \bigtriangledown Load_{(i)}}{Time_{(i+1)} - Time_{(i)}} \quad (5.3)$$

$$av^2 Time_{(i)}[s] = \frac{avTime_{(i+1)} + avTime_{(i)}}{2} \quad (5.4)$$

Note: $av^2 Time_{(i)} = Time_{(i)}$

The approximated time at FI may be calculated by the first point at which significant deviation occurs on the $\bigtriangledown^2 Load$ vs $Time$ curve (this is marked by a red cross on Figure 5.7).

A sampling interval of approximately 0.01 seconds, results in a maximum measuremental error of 0.02 seconds (for the synchronised load cell and high speed camera systems). The observed time shift (dubbed: the *"Naet Shift"*) between maximum Load and fracture initiation lies outside the range of measuremental error. Although measurements suggest a time shift does exist, it is important to note that the difference between maximum Load and the Load at time of fracture is typically less than a few Newtons.

Figure 5.7 exhibits minor fluctuations prior to fracture initiation. This noise is caused by the acoustic (hit) events being recorded in the Vallen acoustic system. An analysis of the hit distribution Figure 5.6 reveals that the noise does not have a major contribution to the deviations observed in Figure 5.7.

Further analyses have shown that the described graphical method for fracture initiation determination works best when there is a sudden diametral single fracture through the sample (i.e. Mode I tensile failure).

This technique was also tested with other rock types with the following results;

- **Mons Chalk (dry and sat)** - The behaviour of the $\bigtriangledown^2 Load$ vs $Time$ plot indicates that this graphical method for fracture initiation determination may be applied to chalk, however as the sampling interval was set too low (0.2s) the results could not be accurately verified using high speed video.
- **Castlegate Sandstone (dry)** - A specific point for fracture initiation for Castlegate Sandstone was difficult to obtain due to the gradual decline observed on the $\bigtriangledown^2 Load$ vs $Time$ curve.
- **Pierre shale** - Samples begun to crack (dry out) as soon as they were removed from oil. Further investigations to fracture initiation were therefor not applied.

The results from this investigation indicate that the Brazilian test data (i.e. Load vs time) may also be used to graphically approximate fracture initiation in addition to finding the point of maximal stress. This discovery is both exciting and encouraging as it allows additional data to be obtained using the existing experimental configurations and techniques of the Brazilian test. Note: A small time step (i.e. $< 0.01s$) is recommended for improved accuracy.

5.3.5 Location Map

During this study, an acoustic emission setup was mounted to the rear side of the sample. The micro fractures that develop in rock create elastic strain waves that can be recorded by acoustic emission (AE) sensors.

A location map was generated using Vallen Software. The location algorithms assume an isotropic material and work on an iterative basis, approximating the source location. The iterative location algorithm needs at least data from 3 measurement channels for a "2D" solution.

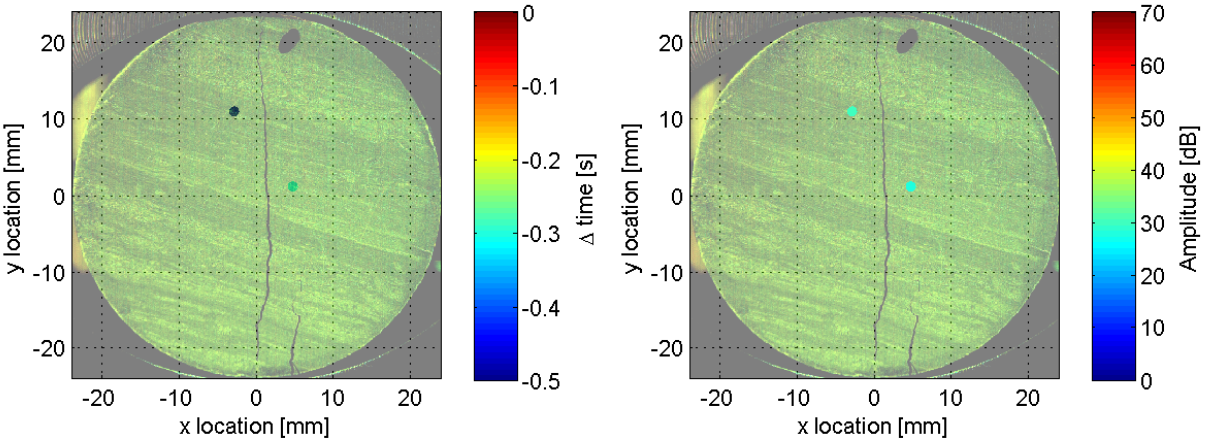

(a) Time Scale (b) Amplitude Scale

Figure 5.9: *Location map at 0.5 seconds prior to UTS for Mancos shale $\beta = 75°$, $\psi = 90°$ (calculated using Vallen Software, isotropic model and a velocity of 3840m/s)*

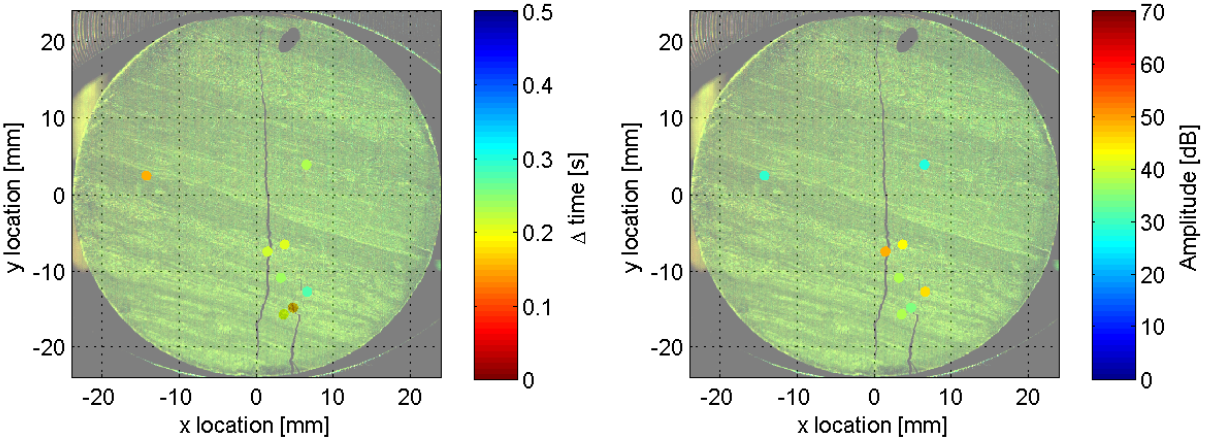

(a) Time Scale (b) Amplitude Scale

Figure 5.10: *Location map at 0.5 seconds after UTS for Mancos shale $\beta = 75°$, $\psi = 90°$ (calculated using Vallen Software, isotropic model and a velocity of 3840m/s)*

Figures 5.9 and 5.10 show the results of a 2D location algorithm for Mancos Shale (assuming isotropic behaviour) at a time of ±0.5 seconds from UTS. Given the anisotropic nature of Mancos Shale it is clear that the isotropic model does not produce reputable results.

If a material is isotropic or quasi-isotropic, waves propagate with the same velocity in all directions. However in anisotropic materials (such as Mancos Shale) the wave velocity depends on the material properties and its orientation. If an isotropic velocity model is applied to an anisotropic case, the source pattern is distorted accordingly as shown in Figures 5.9 and 5.10. In such a case, the estimated locations also fit the data poorly and increase the apparent arrival time uncertainty (Unander, 2002). This problem must be addressed to obtain an accurate source location.

Debecker and Vervoort (2011) present a method for ("2D" and "3D") localization by acoustic emission in transversely isotropic media. The equations as presented by Debecker and Vervoort (2011) may be used to build an improved location algorithm using a least squares analysis.

It should be noted that Debecker and Vervoort (2011) initially derived the velocity by transmitting an ultrasonic P-wave on one end of a sample and receiving it on the other end. However, as the transmitter emitted a pulse, it measured the pulse velocity (not the phase velocity) of the anisotropic medium. The end result was an underestimation of the velocities, and hence a worse localization.

5.4 Conclusions

The fracture initiation point of interest for this study refers to the local tensile failure process. i.e. where fracture initiation, fracture propagation and crack coalescence take place almost instantaneously. Given the interlinked experimental system, it was possible to determine (with a high level of accuracy) the time and location of fracture initiation for an anisotropic material (Mancos Shale) at various angles during diametric loading.

Measurements of displacements on the surface of the sample and calculations of strain fields using a DIC method suggest that the first fracture predominantely initiates in the middle area of the sample (even with the existence of minor preexisting cracks). These observations suggest that the strain criterion may therefor not be applicable for Mancos Shale.

A location map was generated using Vallen Software (assuming an isotropic medium and using the central p-wave acoustic velocity (C), however this did not produce reputable results. Debecker and Vervoort (2011) present a method for ("2D" and "3D") localization by acoustic emission in transversely isotropic media.

In this study it was discovered that a time shift exists between the time of ultimate tensile stress and the time of fracture initiation for Mancos Shale. This phenomenon has been dubbed the *Naet Shift*.

The Naet shift is defined below;

$$NaetShift[s] = Time_{(UTS)}[s] - Time_{(FI)}[s] \tag{5.5}$$

where: UTS is the ultimate tensile strength of the rock and FI is the fracture initiation point of the sample.

For this analysis the time of UTS has been defined as the point at which the maximum Load occurs on the $Load$ vs $Time$ curve and the approximated time at FI may be calculated by the first point at which significant deviation occurs on the $\bigtriangledown^2 Load$ vs $Time$ curve. This enables Naet shift values to be determined using data obtained from the traditional Brazilian testing methods.

Chapter 6 investigates how Naet Shift values relate to crack propagation of rock materials.

Chapter 6

Fracture Propagation

Nathaniel Simpson

Experimental Observations on *The Fracture Propagation of Mancos Shale during the Brazilian Test*

Summary

This chapter investigates the relationship between fracture initiation and fracture propagation of an anisotropic material (Mancos Shale) using Naet shift values. A MTS Load Cell and a Phantom high speed camera to are connected a Vallen Acoustic System (using analog channels) to create a synchronised data collection system. Propagation times are approximated using video footage and image subtraction. Crack lengths are digitally measured with the use of CAD software. Results indicate that fractures are related to their Naet shift value; propagating at different time lengths depending on the layer orientation. The central fracture propagates first (starting from the middle of the sample) and progresses towards the loading platens. The central fracture paths are fairly straight for $90° \leq \beta \leq 60°$ *&* $\beta = 0°$ *and may be zigzagged for* $45° \leq \beta \leq 15°$*. The fracture mode is among others, highly dependent on the relative orientation of weak planes to the applied stress.*

6.1 Introduction

6.1.1 Propagation Modes

Based on the loading type, there are three basic crack propagation modes in a fracture process, namely: Mode I (tension, opening), Mode II (Shear, sliding) and Mode III (shear, tearing). Accordingly, a crack can propagate according to any of these modes or a combination of them (Ke et al., 2009). In fact the combination of mode I and mode II (i.e. mixed mode I–II) is more common in rocks (Ke et al., 2009).

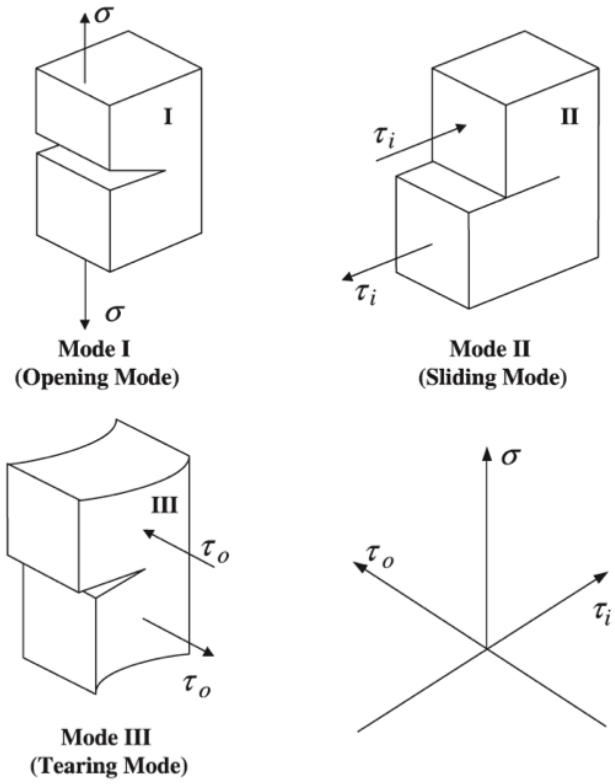

Figure 6.1: Basic Modes of Fracture. *Source (Ke et al., 2009)*

In the Brazilian Experiment we assume that failure only occurs through Mode I and Mode II. Until now, about eleven theoretical criteria for crack initiation and propagation under mixed–mode I–II loading have been proposed; they are presented by Whittaker et al. (1992).

6.1.2 Experimental Methods

Fracture propagation for anisotropic rock has been investigated (experimetally and numerically) using diametrical compression tests on notched Brazilian disk specimens as listed below;

- Al-Shayea (2005) experimentally used Centrally Straight-Notched Brazilian Disk (CSNBD) specimens, with various crack inclinations, to study the crack propagation behaviour under mixed mode I–II loading.
- Chen et al. (1998b) present numerical examples of determination of the mixed mode Stress Intensity Factors (SIF's) for a Cracked Straight Through Brazilian Disc (CSTBD) specimen for both isotropic and anisotropic media.
- Ke et al. (2009) present a model (using the boundary element method) that predicts the crack initiation angles and simulates the crack propagation paths for an anisotropic homogeneous CSTBD specimen under mixed-mode I–II loading.

The study of fracture mechanics consists of five important stages: the initiation of rapid crack propagation, the ensuing crack path, crack speed, crack branching, and crack arrest. These phenomena can be experimentally observed by direct video recording (Hsieh and Wang, 2004).

Imaging techniques have been used in related studies (with mixed results) to study the effect of fracture propagation. A selected sample of these studies are listed below;

- Colback (1966) used high speed photography to capture the photoelastic patterns induced in the birefringent layers to determine the point of fracture initiation and to study its subsequent propagation.

- Hsieh and Wang (2004) used a wedge loading compact tension (WLCT) system with a high speed video device and a high resolution strain gauge system to investigate fracture propagation speeds and crack paths.

- Casem et al. (2007) used a dynamic Brazilian test combined with high speed video to analyse fracture initiation and propagation of SiC using the Digital Image Correlation (DIC) technique.

6.1.3 Types of Fractures

By considering the samples after failure different types of fractures are observed (Tavallali and Vervoort, 2010):

1. Some fractures are parallel to the isotropic layers, which are further called "layer activation".

2. Some fractures are roughly parallel to the loading direction and they are located in the central part of the sample between the two loading lines. The central part is arbitrarily defined as 10 % of the diameter on both sides of the central line. These fractures are further called "central fractures".

3. Fractures outside the central part are also observed. If they do not correspond to layer activation, they are further called "non-central fractures". The latter are often curved lines, starting at or around the loading platens.

In most cases, two or three different fracture types occur in the same experiment (Tavallali and Vervoort, 2010).

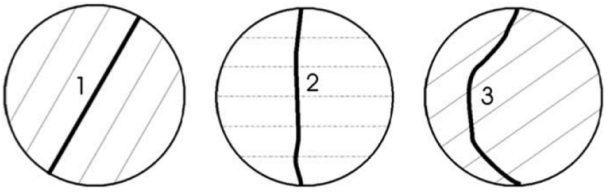

Figure 6.2: *Schematic representation of different fracture types in Brazilian test. (1) Layer activation, (2) central fracture, and (3) Non–central fracture. Source (Tavallali and Vervoort, 2010)*

6.1.4 Objective

This chapter attempts to establish an experimental system that relates crack initiation to crack propagation of rock materials using the Naet shift values defined in Chapter 5. A Brazilian test combined with a high–speed video device has been adopted for this analysis.

6.1.5 The Naet shift

In Chapter 5 it was discovered that a time shift exists between the time of ultimate tensile stress and the time of fracture initiation for Mancos Shale. This phenomenon has been dubbed the *Naet Shift*.

The Naet shift is defined below;

$$NaetShift[s] = Time_{(UTS)}[s] - Time_{(FI)}[s] \tag{6.1}$$

where: UTS is the ultimate tensile strength of the rock and FI is the fracture initiation point of the sample.

For this analysis the time of UTS has been defined as the point at which the maximum Load occurs on the $Load$ vs $Time$ curve and the approximated time at FI may be calculated by the first point at which significant deviation occurs on the $\bigtriangledown^2 Load$ vs $Time$ curve. This enables Naet shift values to be approximated using data obtained from the traditional Brazilian testing methods.

6.2 Experimental Procedure

A synchronised data collection system was created by connecting a MTS Load Cell and a Phantom high speed camera to a Vallen Acoustic System (using analog channels). This allowed data to be collected at approximately 0.01 second intervals and stored to four decimal places.

6.2.1 Brazilian Test

The disc specimens were inserted into a test frame (MTS 2/M) and the load applied along the diameter at a displacement rate of 0.003mm/s using (a Brazilian frame with curved loading jaws). A piece of masking tape was placed between the specimen and load platens to reduce friction and promote a uniform stress distribution along the contact surface.

6.2.2 High Speed Camera

Digital images were recorded during the deformation process at a rate of 5,000 frames per second using a Phantom v12 high speed camera and PCC software (Vision Research). The camera's memory can store approximately 4 seconds of footage after it is manually triggered (in this case, after the main fracture).The image resolution is set to 704×704 pixels with an exposure time of 190μs.

Image subtraction was performed with the use of the program Photoshop C6 (Adobe, 2013).

Crack lengths were digitally measured with the use of the CAD software, AutoCAD (AutoDesk, 2013).

6.3 Results and Discussion

6.3.1 Observation of crack propagation

This study used a high–speed video system to monitor the fracture process during a Brazilian test. Figures 6.3 and 6.6 show the typical results of the observation. Although images captured at 5000 fps were apparently not sufficient to capture in detail the crucial steps of fracture for samples that propagated in Mode I (tension) (namely $90° \leq \beta \leq 60°$ & $\beta = 0°$) the footage provided useful insights for the propagation process for mixed mode I–II (tension and shear) propagation (namely $45° \leq \beta \leq 15°$).

A full set of propagation images may be found in Appendix G.

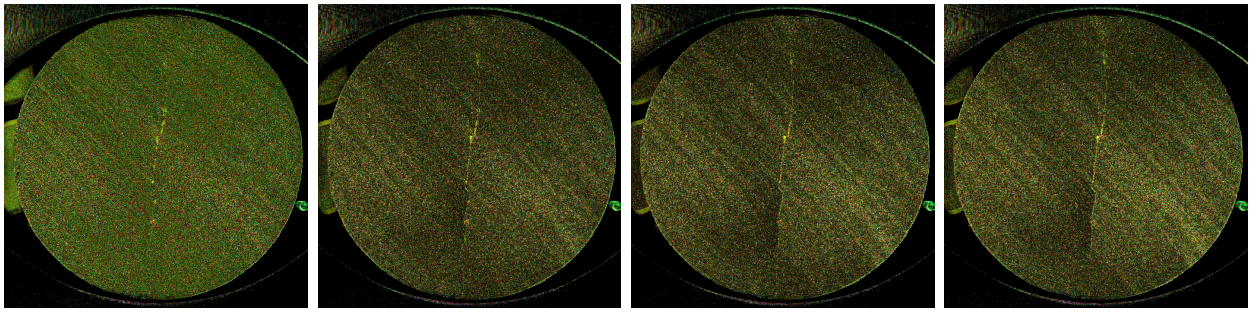

(a) t=0.0000s (b) t=0.0022s (c) t=0.0042s (d) t=0.0062s

Figure 6.3: *Fracture propagation sequence for Mancos Shale,* $\beta = 45°$

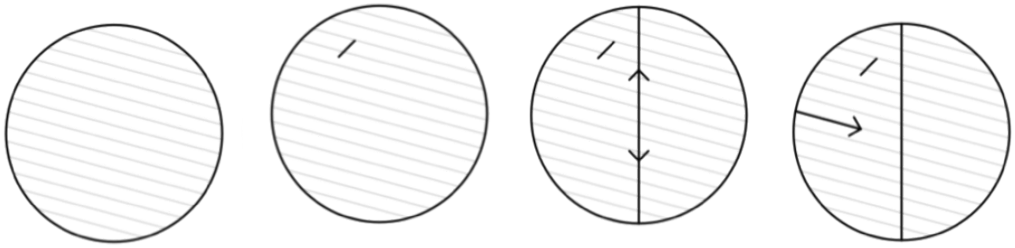

(a) Initial Sample (b) Existing cracks (c) Central Fracture (d) Bedding Plane

Figure 6.4: *Typical fracture propagation sequence for Mancos Shale*

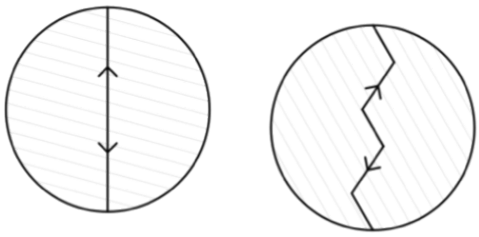

(a) $90° \leq \beta \leq 60°$ & $\beta = 0°$ (b) $45° \leq \beta \leq 15°$

Figure 6.5: *Types of fracturing patterns for the central region*

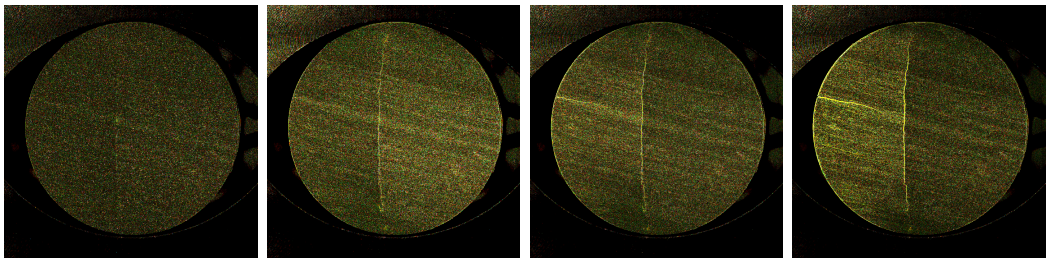

(a) t=0.0000s (b) t=0.0004s (c) t=0.0006s (d) t=0.0008s

Figure 6.6: *Experimentally observed fracture propagation for Mancos Shale,* $\beta = 75°$

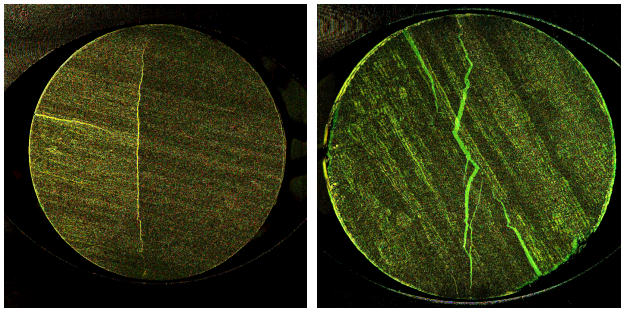

(a) $\beta = 75°$ (b) $\beta = 30°$

Figure 6.7: *Experimentally observed fracturing patterns*

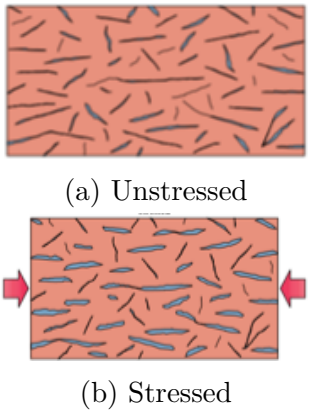

(a) Unstressed

(b) Stressed

Figure 6.8: *In rocks with randomly orientated microcracks (6.8a) cracks at all orientations may be open. When stressed (6.8b), cracks normal to the direction of the maximum compressional stress will close, while cracks parallel to the stress direction will open or remain open. Source (Armstrong et al., 1994)*

It is reasonable to expect that, in uniaxial tension, fractures preferentially initiate from the tips of microcracks lying perpendicular to the direction of principal tensile stress. The resulting crack would propagate in a plane normal to the loading direction, and the specimen would finally separate into two halves (Li and Wong, 2012). An ideal fracture propagation for brittle rock has been presented by (Colback, 1966). Based on the results of this study, a typical fracture sequence in a Brazilian Test on Mancos Shale is illustrated in Figure 6.4 and is further described below;

1. Any Elementary pre–existing cracks within the sample open if they are not perpendicular to the applied load (Figures 6.4b and 6.8).

2. The main diametral central fracture originates in the middle of the specimen (Chapter 5) and grows towards the loading platens (Figure 6.4c).

   (a) Central fracture paths are generally fairly straight for $90° \leq \beta \leq 60°$ & $\beta = 0°$ (Figures 6.5a and 6.7a)

   (b) Central fracture paths may be zigzagged for $45° \leq \beta \leq 15°$ (Figures 6.5b and 6.7b)

3. Secondary fractures may then originate from the edges of the sample and propagate along the bedding towards the centre (Figure 6.4d)

4. Tertiary fractures may then follow a similar sequence as described by Colback (1966)

6.3.2 Crack Propagation Time

Figures 6.3 and 6.6 show that propagation times may vary as a fracture propagates through an anisotropic sample inclined at a certain angle (β) to bedding. The high speed video footage was used to manually estimate the propagation time. Typically, the time interval for Mode I (tension) (namely $90° \leq \beta \leq 60°$ & $\beta = 0°$) is very rapid being less than a few frames (Figure 6.6) with the propagation process for mixed mode I–II (tension and shear) (namely $45° \leq \beta \leq 15°$) taking a longer time to complete (Figure 6.3). In order to confirm the observed measurements a crack-strain-gauge system (similar to the one used byHsieh and Wang (2004)) may be considered for future tests.

The trends from Figures 6.9 and 6.10 suggest that propagation times are related to Naet Shift values. More samples measured at each inclination angle are needed to confirm displayed trends (and values). It is interesting to note how tensile strength, fracture initiation and propagation times appear to be interrelated and dependant on the failure mode (Mode I or Mode I–II).

Fracture pattern measurements within various rock samples can also used as a tool to distinguish between the different failure modes.

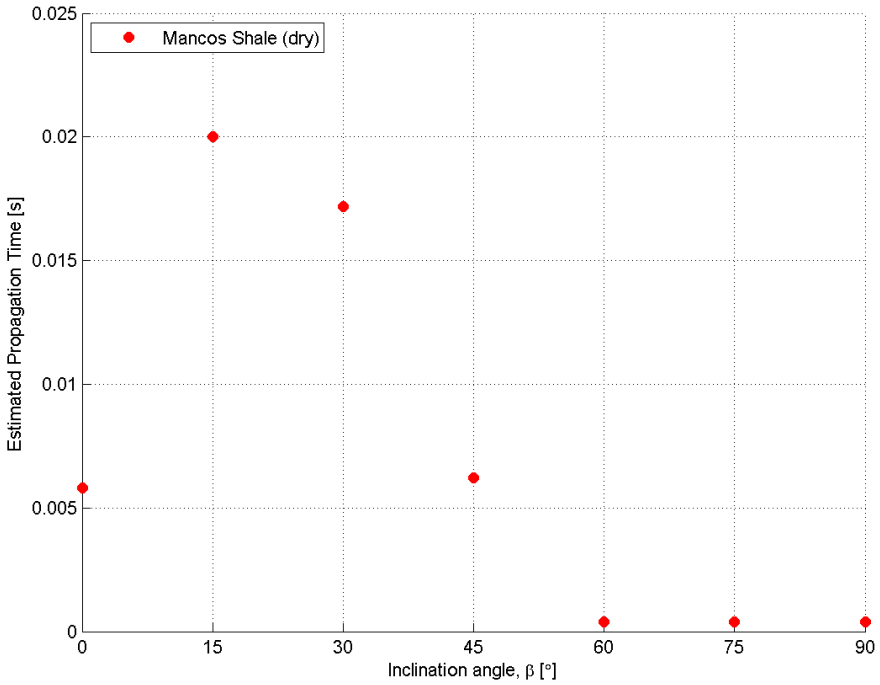

Figure 6.9: *Estimated fracture times from high speed video*

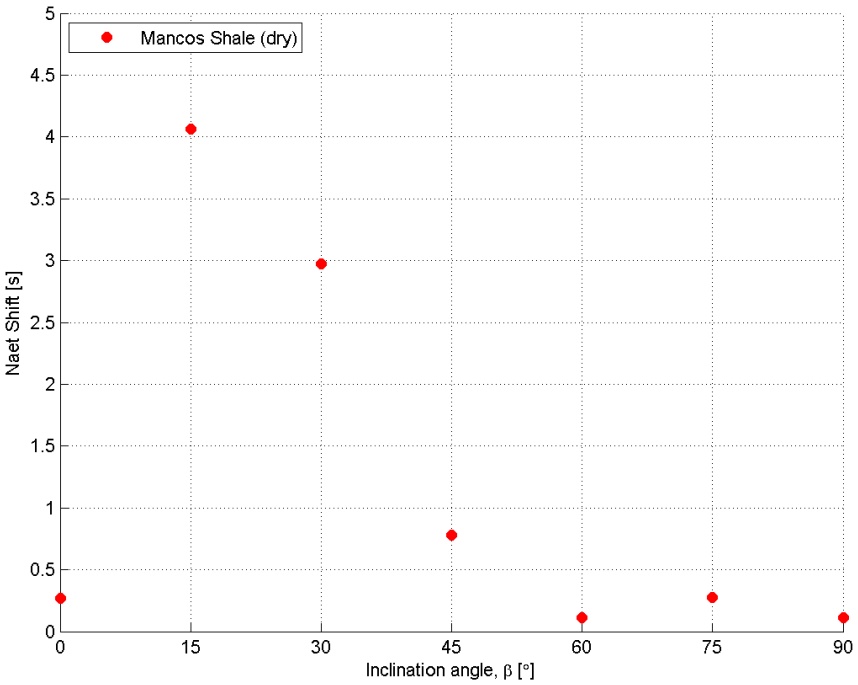

Figure 6.10: *Measured Naet Shift values*

6.3.3 Fracture Patterns

The fracture patterns (including crack initiation and propagation) in the Brazilian test are still a hot issue (Li and Wong, 2012). The fracture patterns in anisotropic rock material are required in many studies however despite its importance, fracture patterns are often poorly discussed and understood (Debecker and Vervoort, 2009).

It was determined in Section 6.3.1 that the diametral central fracture was the first to propagate with secondary and tertiary fractures propagating afterwards. The central fracture was only considered in this fracture pattern analysis as it appears to be directly linked to the ultimate tensile stress of the rock material.

A set of samples after failure are shown in Figure H.1 for Mancos Shale. By observing the fracture patterns in the central region it can be seen that failure occurs by either central fracture(s) only, or a combination of central fractures and layer activation. Note that non–central fractures were not investigated in this analysis. Fracture patterns with images included have been attached in Appendix H.

In Figure 6.12, the layer activation and central fractures in the central region are compared to the total fracture length. It is interesting to note that the total fracture length remains approximately constant for $45° \leq \beta \leq 90°$. The layer activation lengths appear to mirror the relationship from the central fracture lengths.

It can be useful to also consider the percentage of central fracture(s) and layer activation compared to the total fracture length (Figure 6.13). The % of Layer activation may be used to approximate the percentage of shear splitting within the sample. The percentage of shear splitting is less than 10% for $60° \leq \beta \leq 90°$. Note that although $\beta = 0°$ gives a large percentage of apparent layer activation, it is assumed to fail in tension.

Fracture patterns have also been shown to be directly dependent on the degree of strength anisotropy (Debecker and Vervoort, 2009). For a small anisotropy, a limited amount of fractures occur in the weak direction for large inclination angles. However, it becomes the main failure mechanism for small inclination angles (i.e. close to the loading direction). With an increasing degree of anisotropy more fractures in the weak direction occur(Vervoort et al., 2012).

This analysis confirms that, the predominance of a fracture mode, namely axial tensile fractures or shear fracturing along the schistosity or layer direction, is among others, highly dependent on the relative orientation of weak planes to the applied stress direction.

6.4 Conclusion

There are a few key findings that can be observed from the images and are summarized below:

- Fractures propagate at different time lengths depending on the layer orientation
- Naet shift values may be used as a tool to predict variances in propagation times
- The central fracture propagates first (starting from the middle of the sample) and progresses towards the loading platens
- The central fracture paths are fairly straight for $90° \leq \beta \leq 60°$ & $\beta = 0°$ and may be zigzagged for $45° \leq \beta \leq 15°$
- The fracture mode, is among others, highly dependant on the relative orientation of weak planes to the applied stress

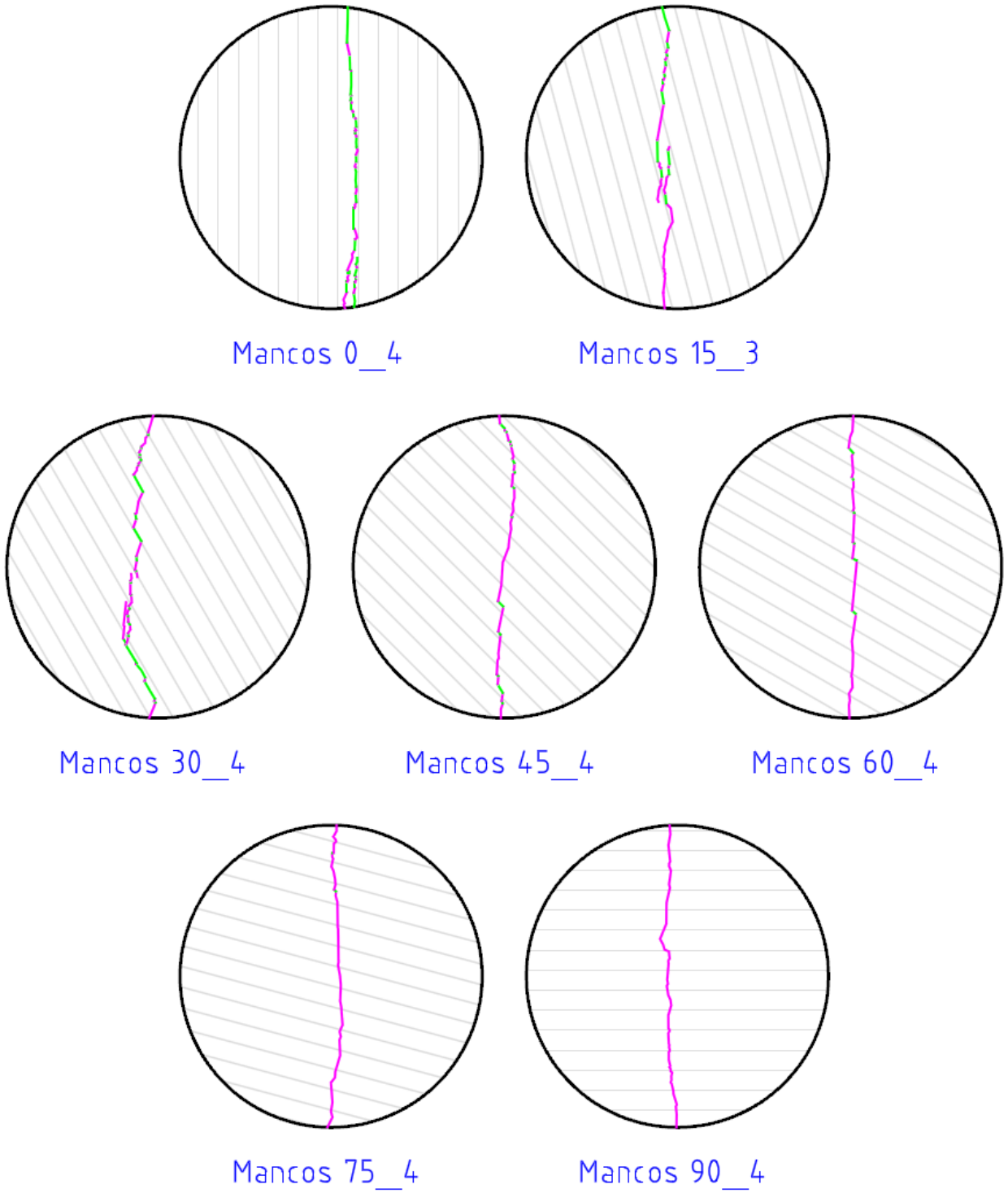

Figure 6.11: *Fracture patterns of the 'central region' after diametrical loading of disk shaped Mancos Shale samples for different inclination angles, β. The parallel thin grey lines indicate the layer direction (D=48mm), Layer Activation is represented in green and central fractures in magenta. Note that non-central fractures were not investigated in this analysis.*

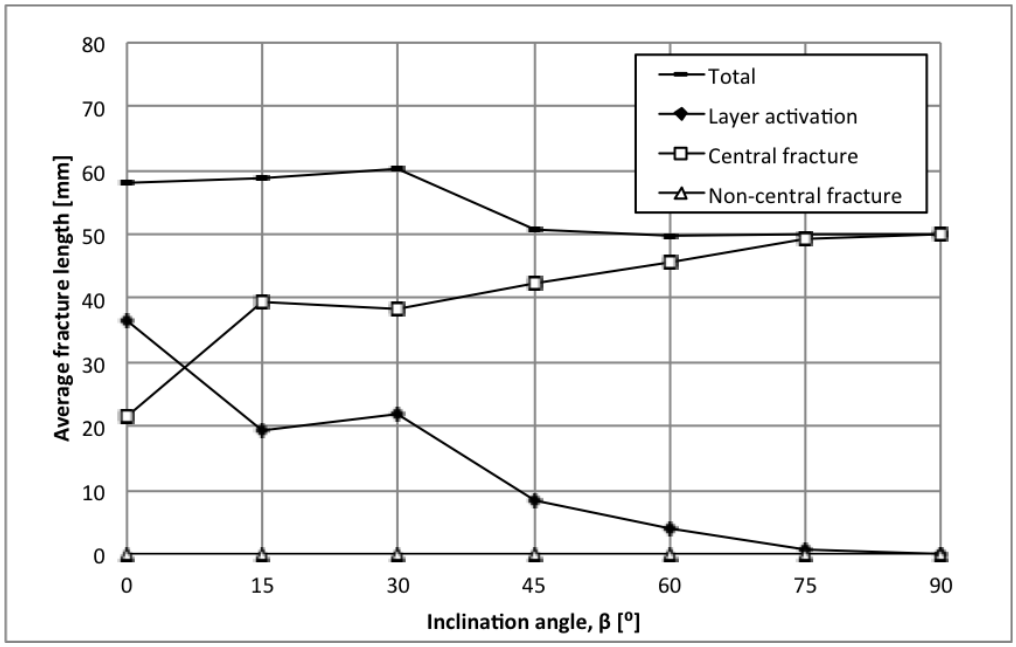

Figure 6.12: *Variation in fracture length as a function of the inclination angle β for Mancos Shale. Note that non-central fractures were not investigated in this analysis.*

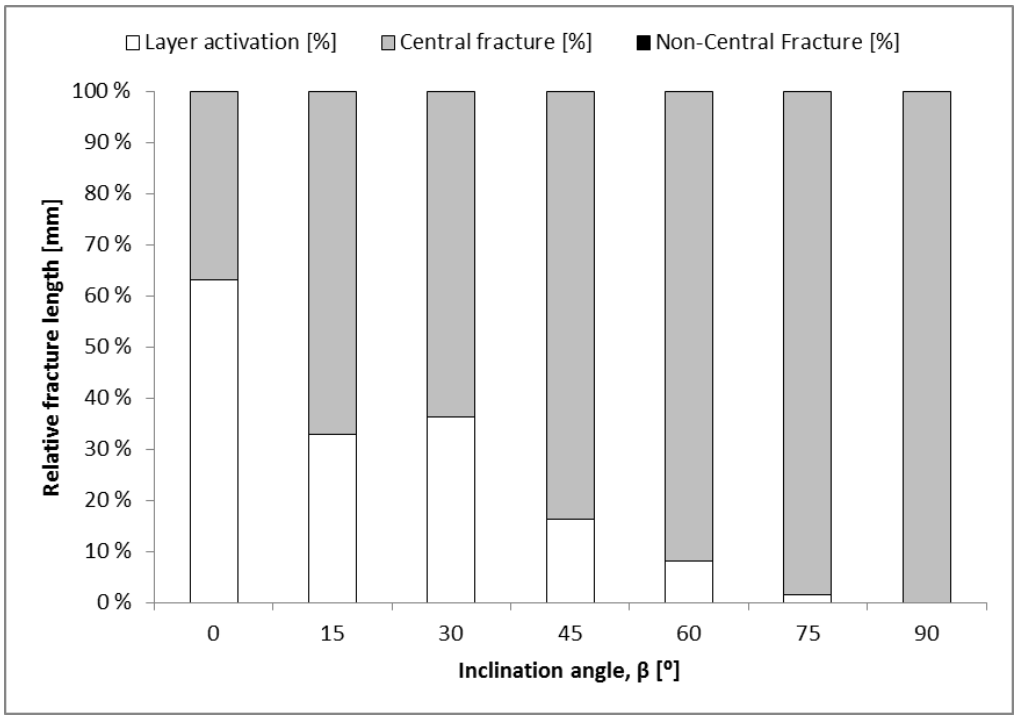

Figure 6.13: *Variation in fracture length percentage corresponding to layer activation and central fracture(s) for Mancos Shale. Note that non-central fractures were not investigated in this analysis.*

Chapter 7

Fracture Modelling & Future Work

Nathaniel Simpson

Literature Review on *The Applicability of Numerical Modelling Methods for Mancos Shale during the Brazilian Test*

Summary

Models may be used as an appropriate tool to assist in understanding the processes occurring for Mancos shale for the following analyses; the anisotropic tensile strength, an altered stress distribution, time of fracture initiation and the crack propagation time. Experimental observations suggest that the applicability of the strain criterion to Mancos Shale should be reviewed as fracture initiation was observed to occur at the centre of the disc. The interlinked experimental system may be improved by using alternate camera and lighting equipment and by building an anisotropic acoustic location map.

7.1 Introduction

This study has presented a number of strength and fracture observations for the Mancos Shale using a unique experimental method with a high speed camera and a mounted acoustic emission system incorporated to a Brazilian test. For the past few decades, many researchers have contributed to developing numerical models in order to give a better understanding for behaviours of rock. Once validated, these models may then be used as an appropriate tool to assist with hydraulic fracture simulations for shale gas production and wellbore stability analysis (Park and Min, 2013).

7.2 Numerical Modelling

In general, numerical design methods are derived from the fundamental laws of force, stress and elasticity (Balasubrahmanyam, 2011). The speed, memory and efficiency of these codes render them well suited to quick design analysis. Numerical models can represent complex geometries with a high degree of accuracy (Balasubrahmanyam, 2011).

The approach adopted in all numerical models is to "divide the problem into small physical and mathematical components and then sum the influence of the components to approximate the behaviour of the whole system". The series of complete mathematical equations formed in this process are then solved approximately (Balasubrahmanyam, 2011).

7.2.1 Numerical Methods

The most commonly applied numerical methods for rock mechanics problems are (Jing, 2003);

- Continuum methods
  - Boundary Element Method (BEM)
  - Finite Element Method (FEM)
  - Finite Difference Method (FDM)
- Discontinuum methods
  - Discrete Element Method (DEM)
- Hybrid Continuum / Discontinuum methods
  - Hybrid FEM/BEM
  - Hybrid BEM/DEM
  - Hybrid FEM/DEM and
  - Other hybrid models

The continuum assumption implies that for all point in a problem region; the materials cannot be torn open or broken into pieces. All material points originally in the neighbourhood of a certain point in the problem region remain in the same neighbourhood throughout the deformation or transport process (Balasubrahmanyam, 2011).

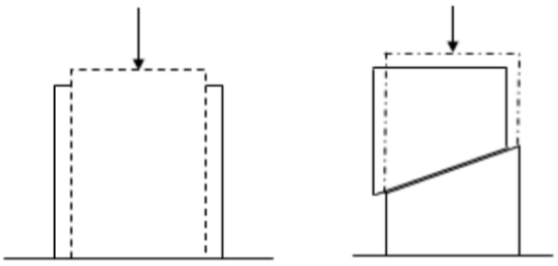

(a) Continuous (b) Discontinuous

Figure 7.1: *Behaviour of uniaxially loaded specimens. Source (Balasubrahmanyam, 2011)*

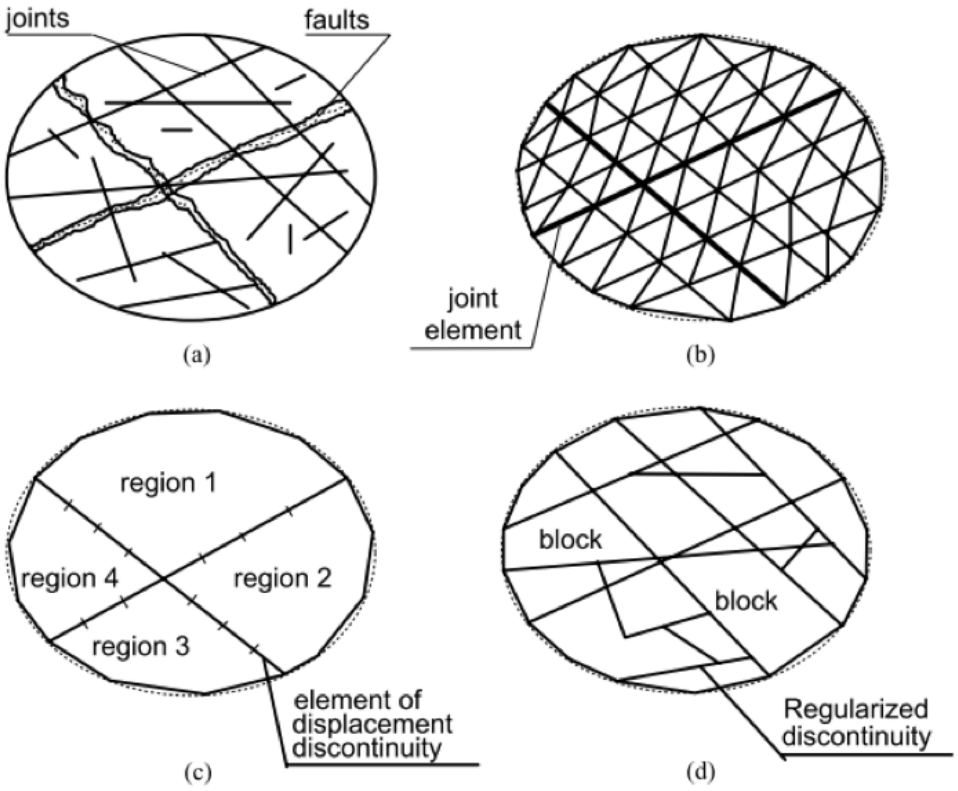

Figure 7.2: *Representation of a fractured rock mass shown in (a), by FDM or FEM shown in (b), BEM shown in (c), and DEM shown in (d). Source (Jing, 2003)*

7.2.2 Boundary Element method (BEM)

This method derives its name from the fact that the user 'discretises', or divides into elements, only boundaries of the problem geometry, thus reducing the problem dimensions by one and greatly simplifying the input requirements (Balasubrahmanyam, 2011).

In this method the conditions on a surface could be related to the state at all points throughout the remaining medium, even to infinity. The information required in the solution domain is separately calculated from the information on the boundary, which is obtained by solution of boundary integral equation (Balasubrahmanyam, 2011).

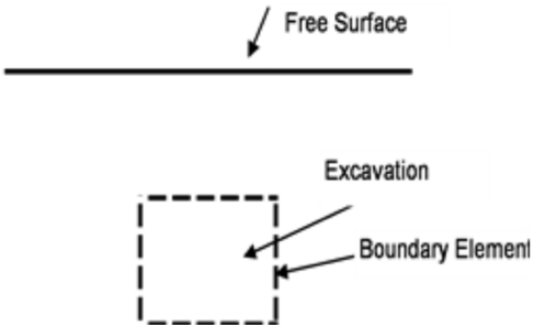

Figure 7.3: *BEM. Source (Balasubrahmanyam, 2011)*

BEMs are simpler and faster, but usually not powerful enough to accommodate complex geometry and excessive variations in rock mass properties (Balasubrahmanyam, 2011).

7.2.3 Finite Element Method (FEM)

The continuum is approximated as a series of discrete elements connected to adjacent elements only at the specific shared points called nodes. The behaviour of each element is then described individually using exact differential equations. The global behaviour of the material is modelled by combining all individual elements (MHSC, 2000).

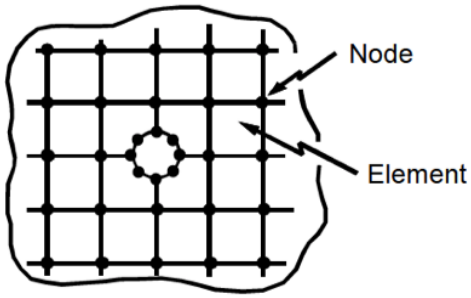

Figure 7.4: *FEM. Source (MHSC, 2000)*

FEM is perhaps the most versatile of all methods and capable of yielding the most realistic results even under complex conditions. Complexity in problem function and requirements of long computer time and large memory space seem to be its major shortcomings (Balasubrahmanyam, 2011).

7.2.4 Finite Difference Method (FDM)

The continuum is represented by a series of discrete grid points at which displacements, velocities and accelerations are calculated. The displacement field is computed by approximating the differential equations for the system as a set of difference equations (central, forward or backward) that are solved discretely at each point (MHSC, 2000).

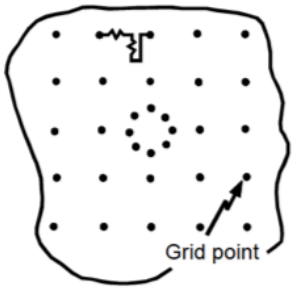

Figure 7.5: *FDM. Source (MHSC, 2000)*

FDM results into conditionally stable solution. That is, convergence of the solution at different stages of iteration to a true solution depends on the size of the elements and size of the load steps. It has also got the advantage of time stepping, which allows for a better understanding of the trend and mode of failure (Balasubrahmanyam, 2011).

7.2.5 Discrete Element Method (DEM)

The DEM for modelling a discontinuum is relatively different compared with BEM, FEM and FDM, and focuses mainly on applications in the fields of fractured or particulate geological media. The essence of DEM is to represent the fractured medium as assemblages of blocks formed by connected fractures in the problem region, and solve the equations of motion of these blocks through continuous detection and treatment of contacts between the blocks. The blocks can be rigid or be deformable with FEM discretizations (Jing, 2003).

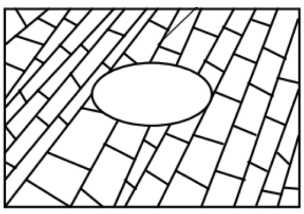

Figure 7.6: *DEM. Source (Jing, 2003)*

The distinct element method is ideally suited to modelling if both large scale geological discontinuities such as faults, dykes and highly fractured assemblages of rock blocks (Jing, 2003).

7.3 Brazilian Test Modelling

Various modelling approaches have been adopted to simulate the stress distributions and fracture process for isotropic and anisotropic rocks subjected to the Brazilian test. Summaries from selected numerical modelling studies are shown in Tables 7.1 and 7.2 below.

7.3.1 Isotropic Rock Models

Table 7.1: Mancos Shale Properties

Authors (year)	Findings	Code	Type
Steen et al. (2005)	It is shown that the influence of the stress gradient on the stress concentration at the tip of mobilised defects lies at the origin of the particular fracturing behaviour in the diametrically loaded disc with a hole.	DIGS	BEM
Yu et al. (2006)	Studies using the 3D FEM and experiments showed that size/shape effects exist in Brazilian tensile strength tests when the disc thickness is increased		FEM
Lanaro et al. (2009)	Discusses the influence of initiated cracks on the stress distribution, and modelling the crack initiation and propagation of Brazilian rock specimens subjected to indirect tensile loading	FRACOD2D	BEM
Li and Wong (2012)	Simulations showed the local concentration of tensile strain to be associated with a first crack initiation position near the loading points, instead of at the centre of the specimen where the maximum extension strain criterion is satisfied.	FLAC	FDM

7.3.2 Anisotropic Rock Models

Table 7.2: Mancos Shale Properties

Authors (year)	Findings	Code	Type
Cai and Kaiser (2004)	It was found that rock anisotropy and pre-existing cracks (length and orientation) play an important role in determining the behaviour of tensile crack initiation and propagation and hence the overall tensile strength of the rocks.	ELFEN	FEM / DEM
Mahabadi et al. (2009)	Demonstrated the suitability of the numerical simulation approach to explicitly model rock deformation and failure for layered rock	Y_GUI	FEM / DEM
Park and Min (2013)	Modelling was performed in order to represent the transversely isotropic rock such as shale, gneiss and schist.	PFC2D	DEM

7.4 Model Validation

This study had a number of key observations (for Mancos Shale) which can be compared with modelled simulations from other rock types. Results from numerical simulations should be compared with laboratory measurements for back calculations and improved input data.

Table 7.3: Mancos Shale Properties

Property	Mancos Experimental Observation	Future Modelling Implications
Anisotropic Tensile Strength (Chapter 3)	The laboratory tests showed that the degree of anisotropy had an influence on the measured peak strength, decreasing slightly with decreasing bedding angles, whereas the orientation of the sample in relation to the loading direction was relatively unimportant for nearly isotropic materials.	The model by Park and Min (2013) presents the Brazilian tensile strength of transversely isotropic rock and seems to have good agreement with the trends that were experimentally determined for Mancos Shale.
Altered Stress Distribution (Chapter 3)	The application of a thin paint layer increases the peak strength of Mancos Shale, possibly due to the change in internal stresses within the sample.	A model similar to the one presented by Yu et al. (2006) may be adapted to investigate the stress distributions of discs with coated surfaces
Fracture Initiation Location (Chapter 5)	Measurements of displacements on the surface of the sample and calculations of strain fields using a DIC method suggest that the first fracture predominantly initiates in the middle area of the sample (even with the existence of minor preexisting cracks). These observations suggest that the strain criterion may therefor not be applicable for Mancos Shale.	Mahabadi et al. (2009) and Li and Wong (2012) incorporate the strain criterion to determine the location of fracture initiation. Given the observations from this study, this criterion may need to be reviewed to assess its applicability to Mancos Shale.
Time of Fracture Initiation (Chapter 5)	In this study it was discovered that a time shift exists between the time of ultimate tensile stress and the time of fracture initiation for Mancos Shale. This phenomenon has been dubbed the *Naet Shift*.	Mahabadi et al. (2009) presents a Load–displacement curve for layered rock. The sample shows a perfect linear behaviour until the peak is reached where the cracks initiate at the centre of the disc. A further analysis should be performed to investigate weather the model also produces the observed time shifts.
Crack Propagation Time (Chapter 6)	Fractures propagate at different time lengths depending on the layer orientation and they are related to their Naet shift values.	Mahabadi et al. (2009) presents fracture propagation at different time steps. Modelling software could be used to develop relationships between propagation time and Naet shift values.

Table 7.3 – continued

Property	Mancos Experimental Observation	Future Modelling Implications
Fracture Patterns (Chapter 6)	The central fracture propagates first (starting from the middle of the sample) and progresses towards the loading platens. The central fracture paths are fairly straight for $90° \leq \beta \leq 60°$ & $\beta = 0°$ and may be zigzagged for $45° \leq \beta \leq 15°$	Cai and Kaiser (2004) state that the crack propagation paths are affected by the bedding orientation and The paths are not straight but zigzagged except when $\beta = 0°$ and $\beta = 90°$. The percentage distributions of central fractures and layer activation are currently not analogous to the observations for Mancos Shale.

7.5 Experimental Improvements and Future Work

A number of experimental improvements and future work ideas have been highlighted throughout this study. They are summarized and listed below;

Elastic Strain analysis (Chapter 1)

A digital camera used together with a time–lapse remote controller could be an effective alternative for measuring pre fracture strain development. Still images could be taken at 0.5 second intervals with an image resolution of 10MP or greater. An increased number of pixels may provide further accuracy when performing the digital image correction analysis.

Tensile Strength (Chapter 3)

The results from this study suggest that the application of a thin paint layer increases the peak strength of Mancos Shale, possibly due to the change in internal stresses within the sample. Further testing is suggested for Mancos Shale at various angles relative to bedding, in order to quantify how surface coatings can affect (indirect) tensile strength values.

Fracture Initiation (Chapter 5)

Debecker and Vervoort (2011) present a method for ("2D" and "3D") localization by acoustic emission in transversely isotropic media. The equations as presented by Debecker and Vervoort (2011) may be used to build an improved location algorithm using a least squares analysis.

The results from this investigation indicate that the Brazilian test data (i.e. Load vs time) may also be used to graphically determine fracture initiation in addition to finding the point of maximal stress. A small time step of $0.01s$ was used in this study. For improved accuracy, future tests may look to reduce the sampling interval even further.

Fracture Propagation (Chapter 6)

Images captured at 5000 fps were apparently not sufficient to capture in detail the crucial steps of fracture for samples that propagated in Mode I (tension) (namely $90° \leq \beta \leq 60°$ & $\beta = 0°$). Filming at higher frame rates may provide a solution to this problem.

Filming at high frame rates requires a significant amount of light. Future experiments may look to employ an improved lighting configuration using DC power, or to utilize bigger lights (i.e. 5000 watts or larger) to reduce the effect of flicker.

The observed crack propagation times should be experimentally confirmed. This may be achieved, for example, by using a crack-strain-gauge system (Hsieh and Wang, 2004).

7.6 Conclusion

Models may be used as an appropriate tool to assist in understanding the processes occurring for Mancos shale for the following analyses; the anisotropic tensile strength, an altered stress distribution, time of fracture initiation and the crack propagation time.

Experimental observations suggest that the applicability of the strain criterion to Mancos Shale should be reviewed as fracture initiation was observed to occur at the centre of the disc.

This study used an experimental system that links tensile strength, fracture initiation and propagation of an anisotropic rock (Mancos Shale) using an integrated Brazilian Test Setup equipped with Acoustic Emission and High Speed Video. This additional information has allowed Mancos Shale to be characterized in greater detail, and has provided information that leads towards an improved understanding of its behaviour.

The interlinked experimental system may be improved by using alternate camera and lighting equipment and by building an anisotropic acoustic location map.

The results of this study are both exciting and encouraging as it allows additional data to be obtained using the existing configurations and techniques of the Brazilian test. Further work may look to assess the applicability of this method to other mechanical rock tests (i.e. the unconfined compression test).

Appendix A

Shale Gas Outlook

Nathaniel Simpson

Literature Review on *The Future Outlook of Shale Gas*

Summary

With the successful marketing of natural gas as an "environmentally friendly" fuel, demand of gas has increased dramatically since the beginning of the 21st century with some experts believing that we may be entering into a "Golden Age of Gas". The combination of two technologies; directional (horizontal) drilling and hydraulic fracturing with increased wellhead prices made it possible to produce unconventional reservoirs economically. Shale gas has been the fastest growing of the unconventional resources in recent years and it is attributed to being the largest contributor to production growth. A gas shale is not a rock type, and a wide variety of minerologies exist amongst different formations. Challenges in producing hydrocarbons from these rocks therby relates not only to identifying the reservoirs, but also optimization of fracking procedures. In order to better identify such reservoirs, estimate their production potential, as well as devise optimum drilling and fracturing strategies, an improved understanding of the fracture behaviour (through anisotropic rock) is needed.

A.1 Future Energy Outlook

A.1.1 World Energy Demand

The world energy demand will continue to rise as we continually strive to meet Earth's demand for energy consumption. Some experts believe that we may be entering into a "Golden Age of Gas" and the International energy agency (IEA) has created a world energy outlook based from this GAS scenario (OECD/EIA, 2011). The Golden Age of Gas Scenario (GAS Scenario) departs from the WEO-2010 New Policies Scenario – the base case – and incorporates a combination of new assumptions that underpin a more positive future outlook for gas. The three scenarios are listed as follows (OECD/IEA, 2013);

- **Current Policies Scenario (2008):** A scenario in the World Energy Outlook that assumes no changes in policies from the mid-point of the year of publication (previously called the Reference Scenario).
- **New Policies Scenario:** A scenario in the World Energy Outlook which takes account of broad policy commitments and plans that have been announced by countries, including national pledges to reduce greenhouse-gas emissions and plans to phase out fossil-energy subsidies, even if the measures to implement these commitments have yet to be identified or announced.
- **GAS Scenario:** A high-gas scenario, examining how natural gas supply and demand could respond to new impetus stemming from both market forces and government policies.

Figure A.1 highlights the various energy demands under 2008 levels, a New Policies Scenario WEO-2010 and under a Gas Scenario (OECD/EIA, 2011). It is interesting to note that the gas demand in 2035 is 13% higher than in the New Policies Scenario, while demand for coal, nuclear & oil declines.

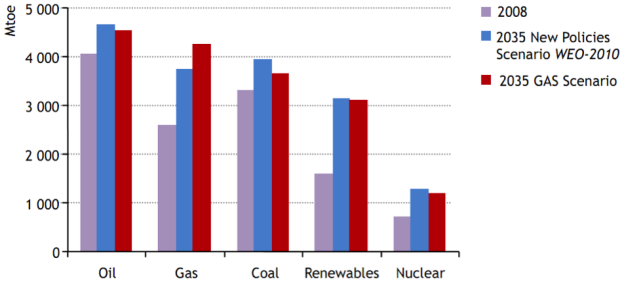

Figure A.1: *World primary energy demand by fuel type and scenario. Source (OECD/EIA, 2011)*

With the successful marketing of natural gas as an "environmentally friendly" fuel, demand of gas has increased dramatically since the beginning of the 21st century. As it is less damaging to the environment, gas may command a premium price over other fossil fuels. Increasingly therefore, a significant percentage of the world's energy demand will be satisfied by natural gas.

Figure A.2 outlines the energy demands under the proposed World Energy Gas scenario (OECD/EIA, 2011). It is interesting to note that gas overtakes coal before 2030 and meets one quarter of global energy demand by 2035. Demand for gas grows by 2% annually, compared with just 1.2% for total energy.

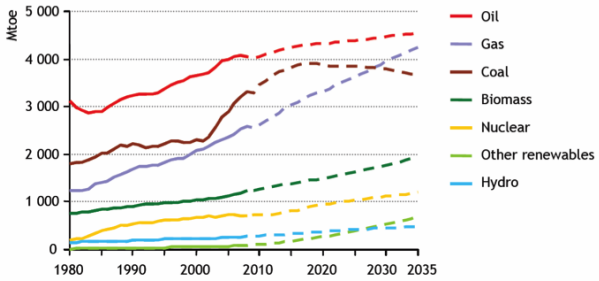

Figure A.2: *World primary energy demand by fuel in the GAS Scenario. Source (OECD/EIA, 2011)*

In the GAS Scenario, demand for gas grows more than 50% by 2035, providing over 25% of world energy "surely a prospect to designate the Golden Age of Gas" (OECD/EIA, 2011).

A.1.2 Economics and Technology

Low prices for natural gas, and ineffective production technology did little to spark interest in unconventional gas in the 1990's, despite publications of the initial gas in place estimates (IGP). The combination of two technologies; directional (horizontal) drilling and hydraulic fracturing (Figure A.5) with increased wellhead prices made it possible to produce unconventional reservoirs economically (Navarro, 2012). Wellhead prices for gas (Figure A.3) have risen from values of less than $2.00 per MCF (thousand cubic feet) in the 1980's to a peak of $10.82 per MCF in the summer of 2008 (U.S. Energy Information Administration, 2013).

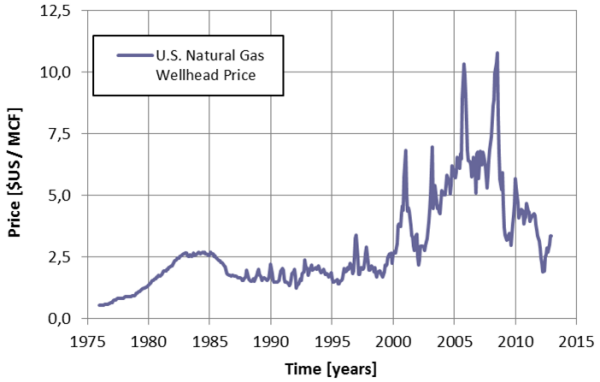

Figure A.3: *U.S. Natural Gas Wellhead Price 1970 – Present. Source (U.S. Energy Information Administration, 2013)*

Although prices have declined recently due to the economic downturn, further increases in unconventional gas production are expected (DOE/EIA, 2012).

A.1.3 World Natural Gas Production

Figure A.4 below describes the World natural gas production by source in the GAS Scenario (OECD/EIA, 2011). Natural gas, and specifically unconventional natural gas, is now a hot topic for the industry and public at large (Bakshi, 2012). It is important to note that unconventional gas supplies (Shale, Coalbed methane and Tight Gas) make up nearly one quarter of total production in the year 2035.

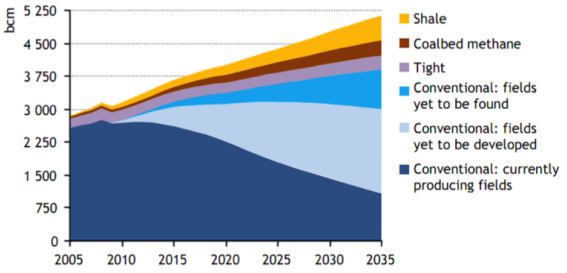

Figure A.4: *World natural gas production by source in the GAS Scenario. Source (OECD/EIA, 2011)*

A.2 Reservoir Types

A.2.1 Conventional Reservoirs

Conventional reservoirs are those that can be produced at economic flow rates and that will produce economic volumes of oil and gas without large stimulation treatments or any special recovery process. A conventional reservoir is easily a high- to medium- permeability reservoir in which one can drill a vertical well, perforate the pay interval, and then produce the well at commercial flow rates and recover economic volumes of oil and gas (Naik, 2002).

A.2.2 Unconventional Reservoirs

An unconventional reservoir is one that cannot be produced at economic flow rates or that does not produce economic volumes of oil and gas without assistance from massive stimulation treatments or special recovery processes and technologies (Naik, 2002).

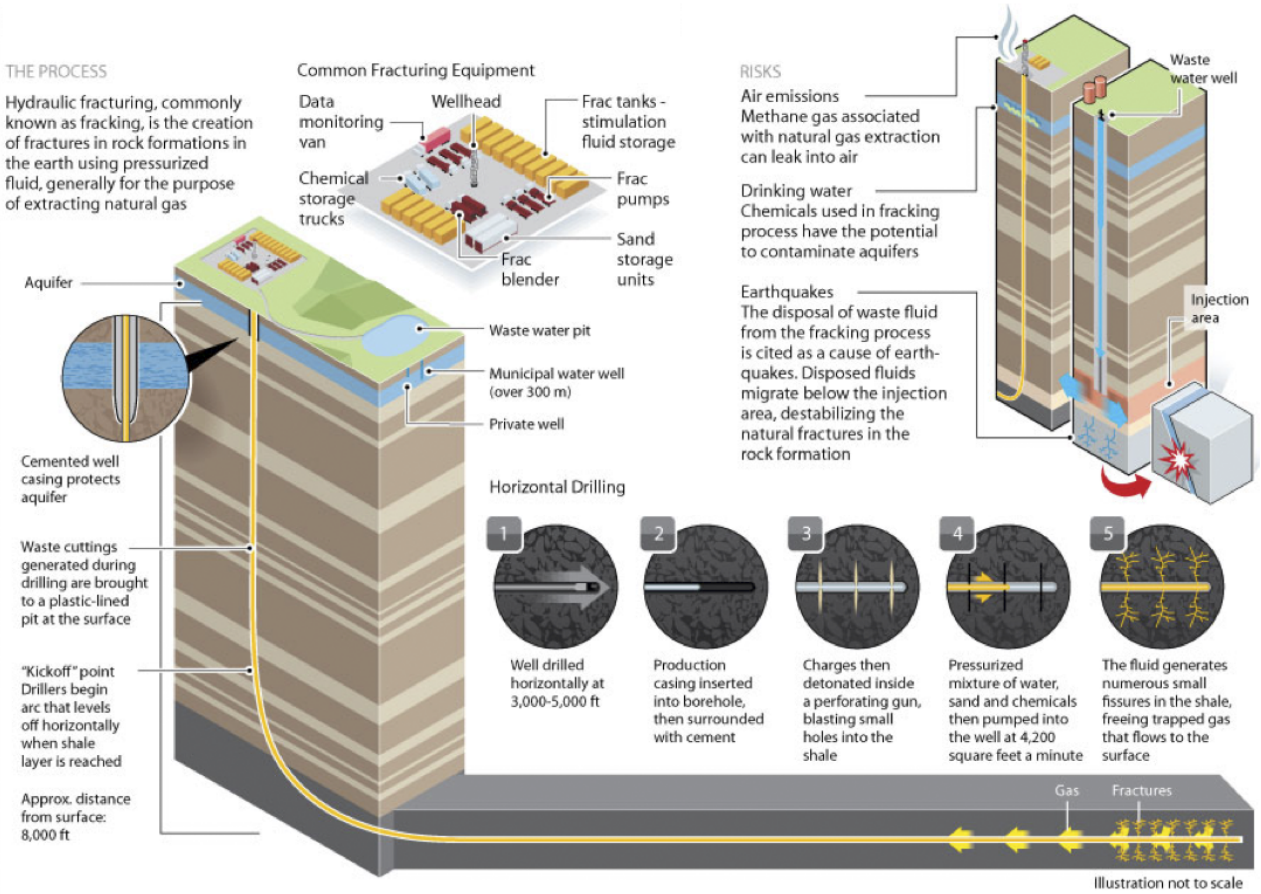

Figure A.5: *Hydraulic Fracturing - How it works. Source (Reuters, 2012)*

A.3 Unconventional Gas

A.3.1 The Gas Resource Triangle

Figure A.6 outlines the gas resource triangle. The underlying concept is that unlike conventional reservoirs, which are small in volume and easy to develop, unconventional reservoirs are large in volume but difficult to develop. Unconventional resources are probably very large, but their character and distribution are not well understood. It is known to exist in large quantity but does not flow easily toward existing wells for economic recovery (Holditch, 2006)

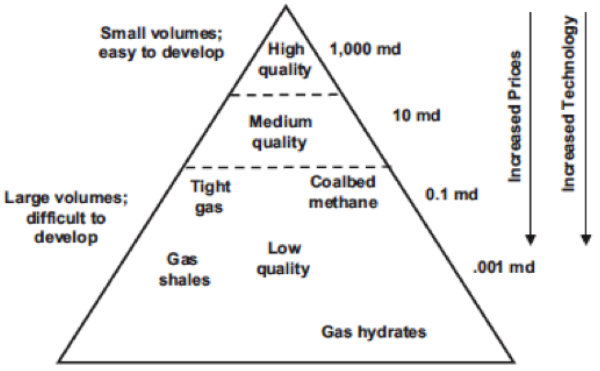

Figure A.6: *Resource Triangle for natural gas. Source (Holditch, 2006)*

A.3.2 Unconventional Gas Types

Essentially, there are six main categories of unconventional natural gas. These include; deep gas, tight gas, gas-containing shales, coalbed methane, geopressurized zones, and Arctic and sub-sea hydrates.

A brief description of each resource type has been adapted from Natural Gas (2011);

- **Deep Gas:** Natural gas that exists in deposits very far underground, beyond 'conventional' drilling depths.
- **Tight Gas:** This is gas that is stuck in a very tight formation underground, trapped in unusually impermeable, hard rock, or in a sandstone or limestone formation that is unusually impermeable and non-porous (tight sand).
- **Shale Gas:** Shale is a very fine-grained sedimentary rock, which is easily breakable into thin, parallel layers. It is a very soft rock, but it does not disintegrate when it becomes wet. These shales can contain natural gas, usually when two thick, black shale deposits 'sandwich' a thinner area of shale. Because of some of the properties of these shales, the extraction of natural gas from shale formations is more difficult and perhaps more expensive than that of conventional natural gas.
- **Coalbed Methane:** Many coal seams also contain natural gas, either within the seam itself or the surrounding rock.
- **Geopressurized Zones:** Are natural underground formations that are under unusually high pressure for their depth.
- **Methane Hydrates:** These interesting formations are made up of a lattice of frozen water, which forms a sort of 'cage' around molecules of methane.

Unconventional natural gas constitutes a large proportion of the natural gas that is left to be extracted within the world and it continues to provide an ever increasing role in supplementing the world's natural gas supply. As our understanding of these resources and technology develops, the resource potential of unconventional natural gas is enormous.

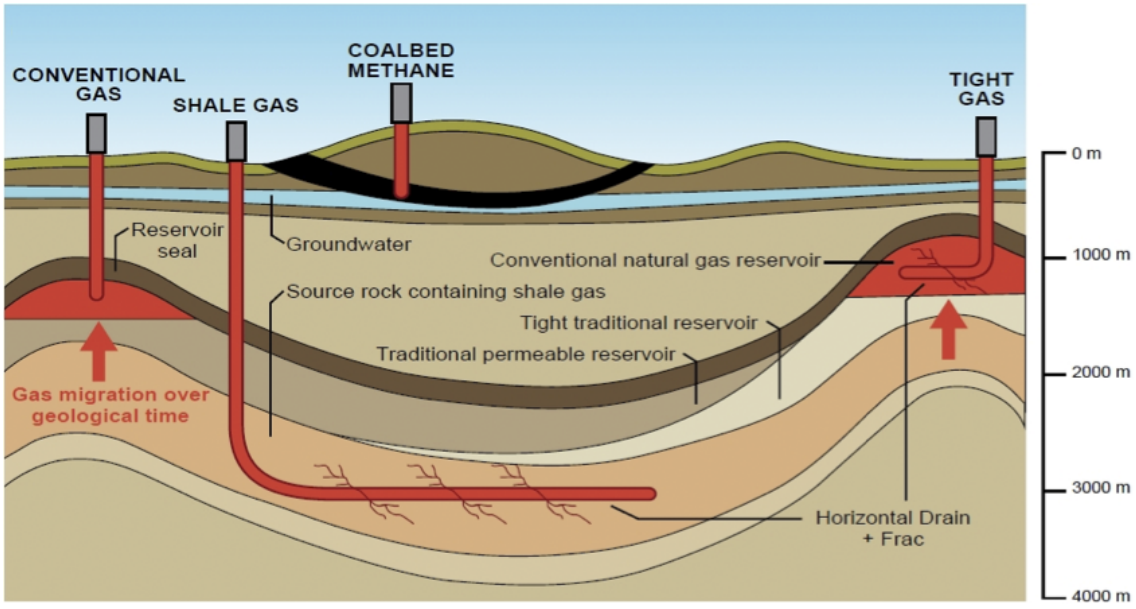

Figure A.7: *Geological Traps. Source (Department of Mines and Petroleum, 2012)*

A.4 Shale Gas

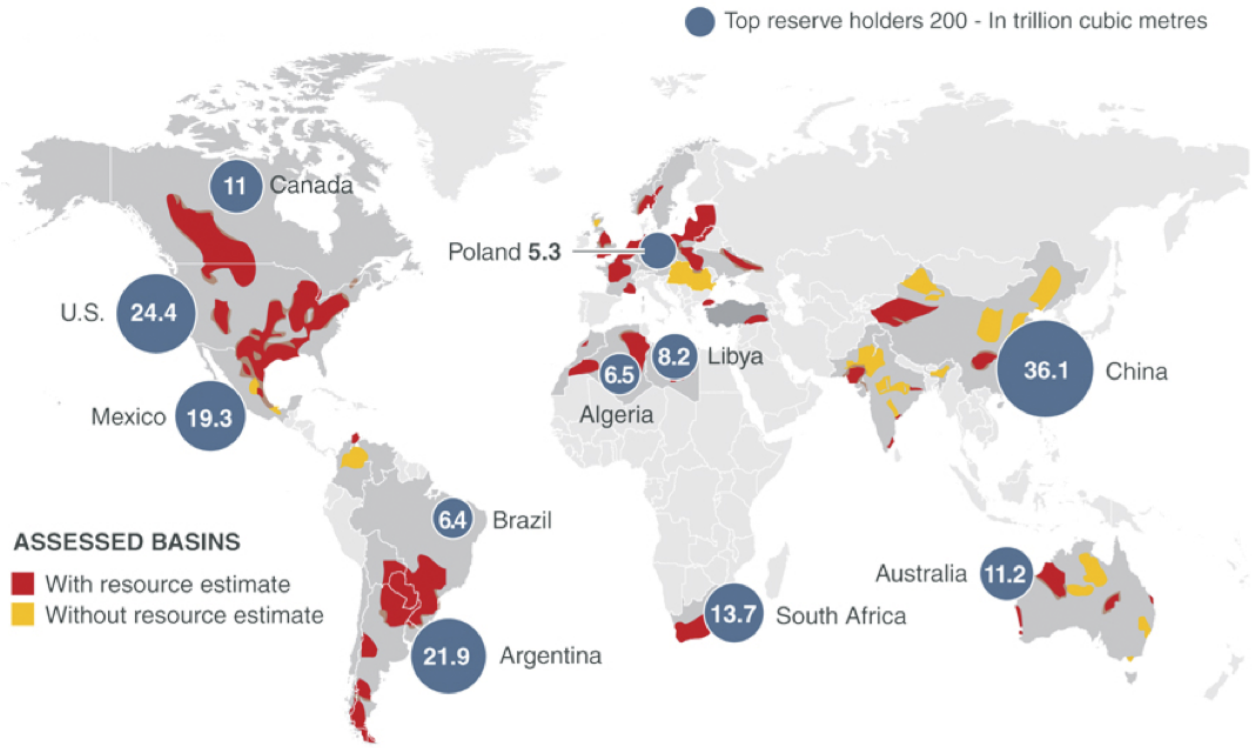

Figure A.8: *Global Shale Gas Basins. Source (Trevethan, 2012)*

A.4.1 Global Supplies

In total, 48 shale gas basins have been assessed in 32 countries, containing almost 70 shale gas formations (EIA, 2011b). These assessments cover the most prospective shale gas resources in a select group of countries that demonstrate some level of relatively near-term promise and for basins that have a sufficient amount of geologic data for resource analysis. Figure A.8 shows the location of these basins and the regions analysed.

Although the shale gas resource estimates will likely change over time as additional information becomes available, the data shows that the international shale gas resource base is vast. The initial estimate of technically recoverable shale gas resources in the 32 countries examined is 5,760 trillion cubic feet (EIA, 2011b).

The estimates of technically recoverable shale gas resources for the 32 countries outside of the United States represents a moderately conservative 'risked' resource for the basins reviewed. These estimates are uncertain given the relatively sparse data that currently exist and the approach the consultant has employed would likely result in a higher estimate once better information is available (EIA, 2011b).

A.4.2 Production Forecasts

Shale gas has been the fastest growing of the unconventional resources in recent years. The international energy agency estimated in 2012 that "remaining technically recoverable resources of shale gas amount to 208 trillion cubic metres (tcm), tight gas 76 tcm and coal bed methane 47 tcm (OECD/IEA, 2012)." This is a total of 331 tcm of unconventional natural gas globally, which compares favourably with the IEA's estimate for conventional gas of 421 tcm (Bakshi, 2012).

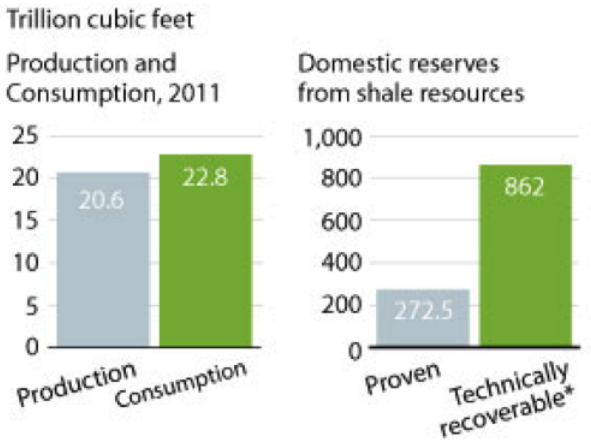

Figure A.9: *U.S. Natural Gas. Source (Reuters, 2012)*

The increase in natural gas production from 2010 to 2035 in the 2008 Reference case results primarily from the continued development of shale gas resources. Shale gas is the largest contributor to production growth (Figure A.9); there is relatively little change in production levels from tight formations, coalbed methane deposits, and offshore fields (Figure A.7) (DOE/EIA, 2012).

Shale gas accounts for 49 percent of total U.S. natural gas production in 2035, more than double its 23-percent share in 2010 (Figure A.10) (DOE/EIA, 2012).

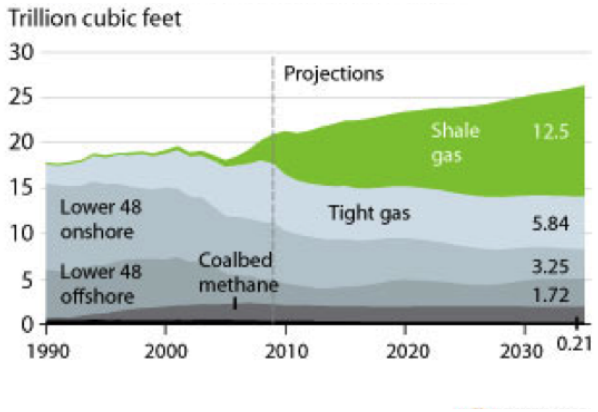

Figure A.10: *U.S. Natural Gas Production by Source. Source (Reuters, 2012)*

A.5 Conclusion

Future energy predictions show that shale gas will play an important role in meeting the increasing energy demands of the future. Despite the large volume of initial gas in place, artificial stimulation treatments (horizontal drilling and hydraulic fracturing) are needed in order to produce shale gas economically.

A gas shale is not a rock type, and a wide variety of minerologies exist amongst different formations. Challenges in producing hydrocarbons from these rocks therby relates not only to identifying the reservoirs, but also optimization of fracking procedures (Torsaeter et al., 2012).

This has motivated researchers, both in acedemia and industry, to characterise gas shale rocks in greater detail to provide more reliable predictions and an improved understanding of their behaviour (Torsaeter et al., 2012).

This study attempts to further our knowledge of this behaviour by establishing an experimental system that links fracture development initiation and propagation, through Mancos Shale.

Appendix B

P-wave velocity Data

B.1 Mancos Shale statistical P-wave velocity data

Table B.1: Mancos P wave velocity statistics

Inclination angle	0	15	30	45	60	75	90	C
Minimum	3738	3754	3797	3848	3919	3995	4038	3958
Lower Quartile	3779	3786	3820	3895	3965	4037	4085	4084
Median	3806	3816	3854	3925	3999	4081	4135	4138
Upper Quartile	3836	3846	3889	3966	4043	4138	4208	4208
Maximum	3992	4033	3996	4066	4220	4355	4409	4517
Mean	3813	3826	3863	3932	4014	4102	4161	4157
St Dev.	55	58	50	53	69	91	103	116

Note: Statistics obtained from 24 Mancos Shale samples at the angle step given above

B.2 All Rock Types P-wave velocity data

Table B.2: P wave velocity measurements of all rock types

Sample Type	0	15	30	45	60	75	90	C
Castlegate Sandstone (dry)	2053	2106	2130	2106	2035	1944	1860	1862
Mons Chalk (dry)	2325	2334	2361	2395	2386	2348	2308	2229
Mons Chalk (sat)	2075	2025	1987	1963	1963	1992	2054	1978
Mancos Shale (oil)	3806	3816	3854	3925	3999	4081	4135	4138
Pierre Shale (oil)	2327	2347	2387	2434	2491	2545	2556	2623

Note: The median values for Mancos Shale are displayed above. Velocity measurements from Castlegate sandstone, Mons Chalk and Pierre Shale were all taken from only 1 sample.

Appendix C

Tensile Stength Data

C.1 Mancos Shale Tensile Strength Statistics (All)

Table C.1: Mancos Shale statistics

Inclination angle, β [°]	Mean TS $[MPa]$	Std. Dev $[MPa]$	No. of tests	Std. Dev of of the mean[MPa]	Coeff. of variation [%]
0	3.25	0.92	5	0.41	28
15	2.72	0.36	5	0.16	13
30	3.07	0.72	5	0.32	24
45	2.93	0.49	5	0.22	17
60	3.33	0.39	5	0.17	12
75	3.00	0.38	5	0.17	13
90	3.28	0.71	5	0.32	22

C.2 Mancos Shale Tensile Strength Statistics (Dry)

Table C.2: Mancos Shale (Dry) statistics

Inclination angle, β [°]	Mean TS $[MPa]$	Std. Dev $[MPa]$	No. of tests	Std. Dev of of the mean[MPa]	Coeff. of variation [%]
00	2.56	0.11	2	0.08	4
15	2.47	0.17	3	0.10	7
30	2.58	0.24	3	0.14	9
45	2.66	0.34	3	0.20	13
60	3.05	0.10	3	0.06	3
75	3.22	0.27	3	0.15	8
90	2.77	0.20	3	0.12	7

Appendix D

Fracture Initiation Location

D.1 Mancos Shale (dry) $\beta = 0°$

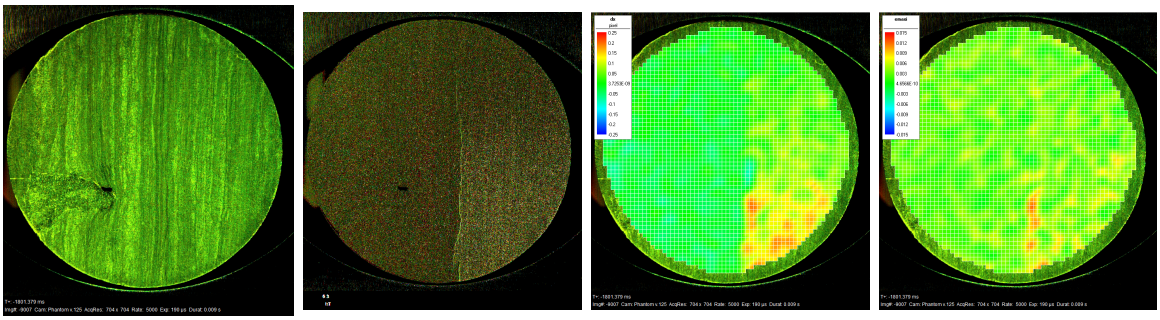

(a) Original image (b) Image subtracted (c) x–displacement (d) Strain tensor (E)

Figure D.1: *Fracture Initiation point in (a), (b), (c) and (d). (c) scale:* $-0.25 < \Delta p < 0.25$ *with 1 pixel* $(p) = 0.072mm$*, (d) scale:* $-0.015 < E_{maxi} < 0.015$

D.2 Mancos Shale (dry) $\beta = 15°$

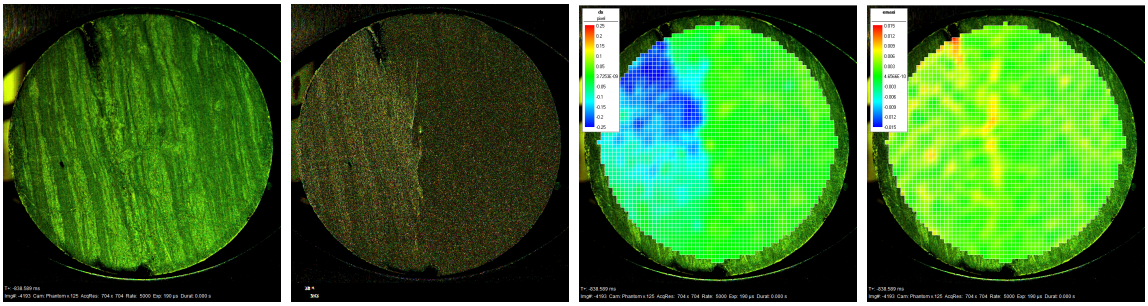

(a) Original image (b) Image subtracted (c) x–displacement (d) Strain tensor (E)

Figure D.2: *Fracture Initiation point in (a), (b), (c) and (d). (c) scale:* $-0.25 < \Delta p < 0.25$ *with 1 pixel* $(p) = 0.072mm$*, (d) scale:* $-0.015 < E_{maxi} < 0.015$

D.3 Mancos Shale (dry) $\beta = 30°$

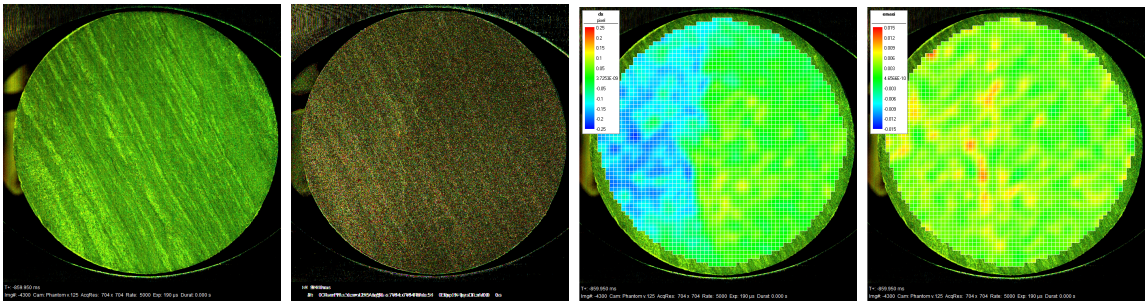

(a) Original image (b) Image subtracted (c) x–displacement (d) Strain tensor (E)

Figure D.3: *Fracture Initiation point in (a), (b), (c) and (d). (c) scale:* $-0.25 < \Delta p < 0.25$ *with 1 pixel* $(p) = 0.071mm$*, (d) scale:* $-0.015 < E_{maxi} < 0.015$

D.4 Mancos Shale (dry) $\beta = 45°$

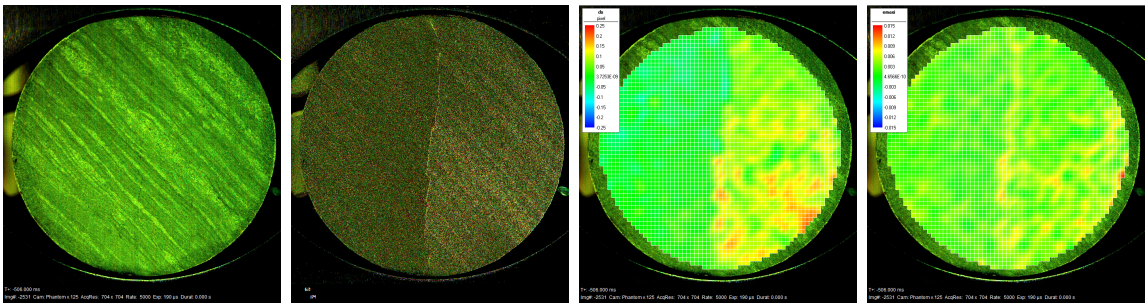

(a) Original image (b) Image subtracted (c) x–displacement (d) Strain tensor (E)

Figure D.4: *Fracture Initiation point in (a), (b), (c) and (d). (c) scale:* $-0.25 < \Delta p < 0.25$ *with 1 pixel* $(p) = 0.072mm$*, (d) scale:* $-0.015 < E_{maxi} < 0.015$

D.5 Mancos Shale (dry) $\beta = 60°$

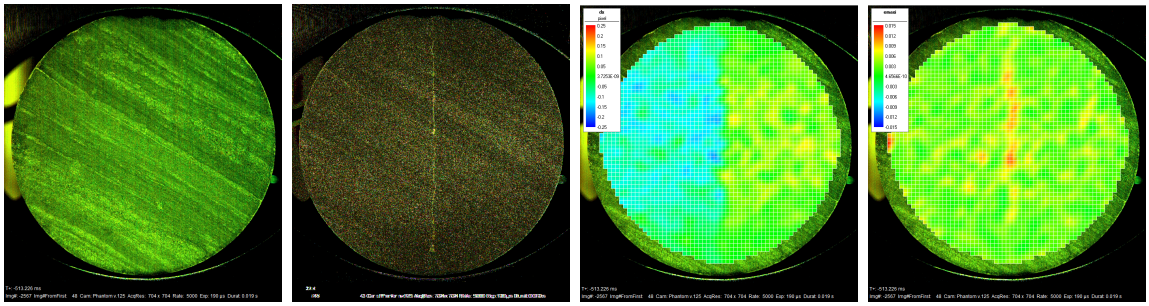

(a) Original image (b) Image subtracted (c) x–displacement (d) Strain tensor (E)

Figure D.5: *Fracture Initiation point in (a), (b), (c) and (d). (c) scale:* $-0.25 < \Delta p < 0.25$ *with 1 pixel* $(p) = 0.072mm$*, (d) scale:* $-0.015 < E_{maxi} < 0.015$

D.6 Mancos Shale (dry) $\beta = 75°$

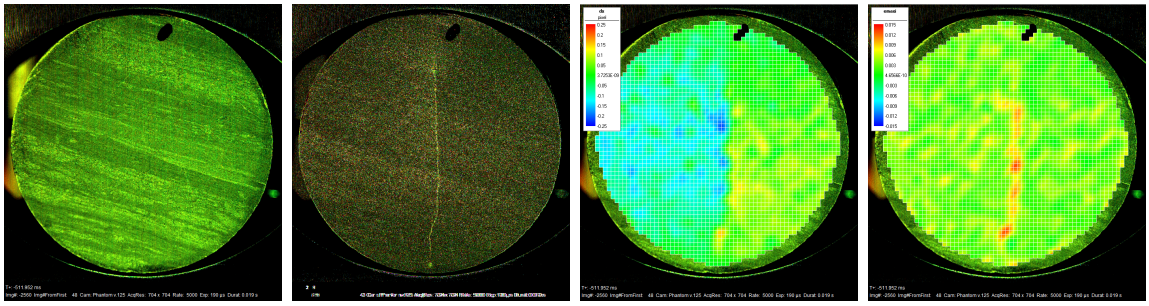

(a) Original image (b) Image subtracted (c) x–displacement (d) Strain tensor (E)

Figure D.6: *Fracture Initiation point in (a), (b), (c) and (d). (c) scale:* $-0.25 < \Delta p < 0.25$ *with 1 pixel* $(p) = 0.072mm$*, (d) scale:* $-0.015 < E_{maxi} < 0.015$

D.7 Mancos Shale (dry) $\beta = 90°$

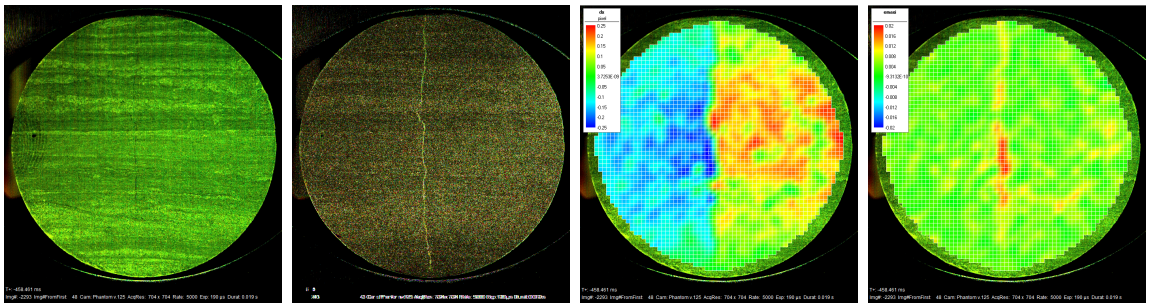

(a) Original image (b) Image subtracted (c) x–displacement (d) Strain tensor (E)

Figure D.7: *Fracture Initiation point in (a), (b), (c) and (d). (c) scale:* $-0.25 < \Delta p < 0.25$ *with 1 pixel* $(p) = 0.072mm$*, (d) scale:* $-0.02 < E_{maxi} < 0.02$

D.8 Castlegate Sandstone (dry)

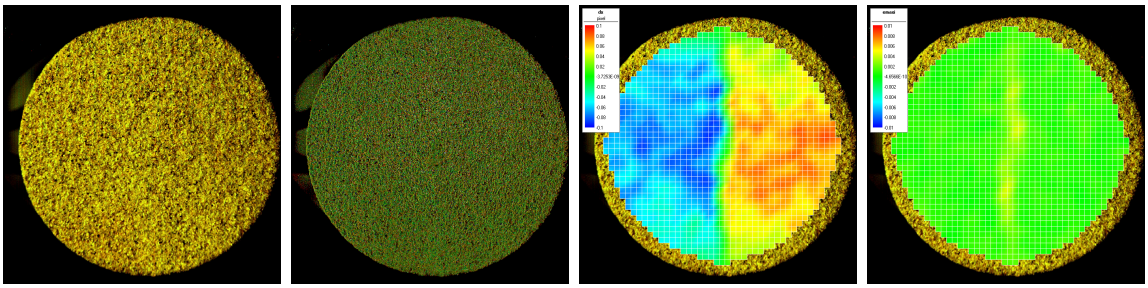

(a) Original image (b) Image subtracted (c) x–displacement (d) Strain tensor (E)

Figure D.8: *Fracture Initiation point in (a), (b), (c) and (d). (c) scale:* $-0.2 < \Delta p < 0.2$ *with 1 pixel* $(p) = 0.008mm$*, (d) scale:* $-0.02 < E_{maxi} < 0.02$

D.9 Mons Chalk (dry)

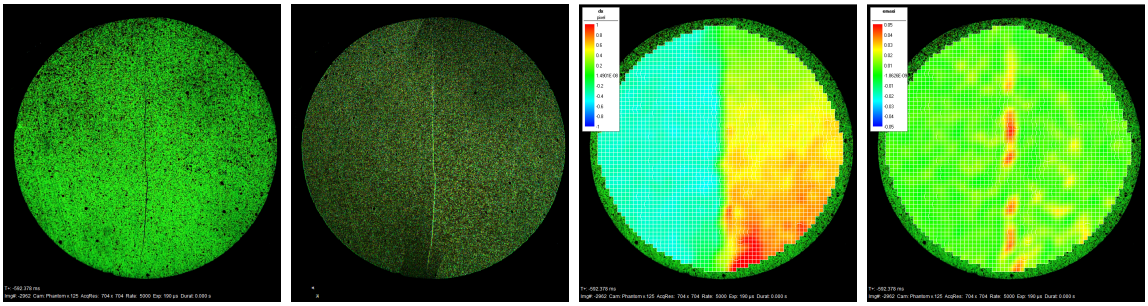

(a) Original image (b) Image subtracted (c) x–displacement (d) Strain tensor (E)

Figure D.9: *Fracture Initiation point in (a), (b), (c) and (d). (c) scale:* $-1.0 < \Delta p < 1.0$ *with 1 pixel* $(p) = 0.072mm$*, (d) scale:* $-0.05 < E_{maxi} < 0.05$

D.10 Mons Chalk (sat)

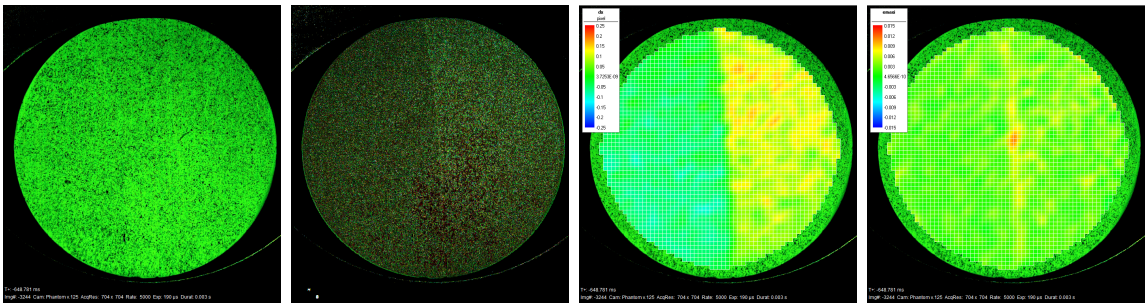

(a) Original image (b) Image subtracted (c) x–displacement (d) Strain tensor (E)

Figure D.10: *Fracture Initiation point in (a), (b), (c) and (d). (c) scale:* $-0.25 < \Delta p < 0.25$ *with 1 pixel* $(p) = 0.072mm$*, (d) scale:* $-0.015 < E_{maxi} < 0.015$

Appendix E

Fracture Initiation Time

E.1 Estimated and Observed Time of Fracture Initiation

Table E.1: Time of Measured and Observed Fracture Initiation

Angle, β [°]	UTS [s]	Measured FI [s]	Observed Fracture [s]	Data point after (b) [s]
0	185.3515	185.6137	185.5110	185.6242
15	197.4102	201.4682	201.4653	201.4786
30	231.9398	234.9072	234.5744	234.9177
45	186.1065	186.8798	186.9202	186.8929
60	189.6507	189.7556	189.7562	189.7660
75	219.1786	219.4512	219.4530	219.4617
90	200.598	200.7027	200.7159	200.7237

E.2 Mancos Shale (dry) $\beta = 0°$

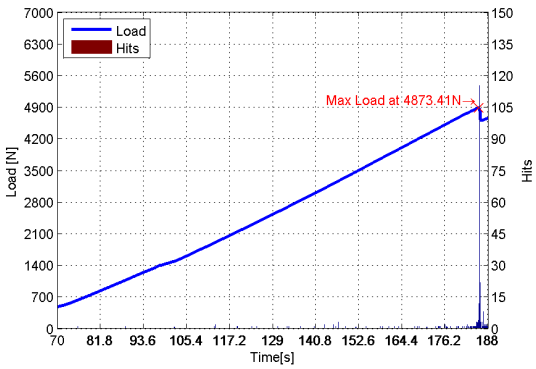

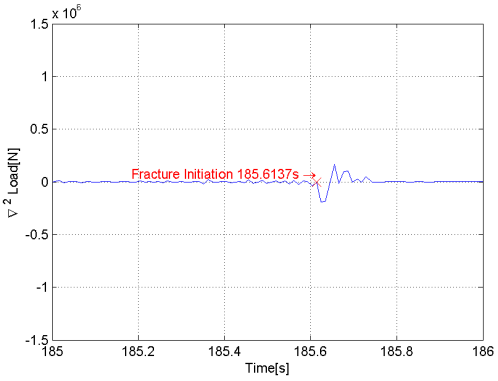

Figure E.1: *The measured time of Ultimate tensile stress has been defined as the point at maximum Load occurs on the Load vs Time curve (this is marked by a red cross)*

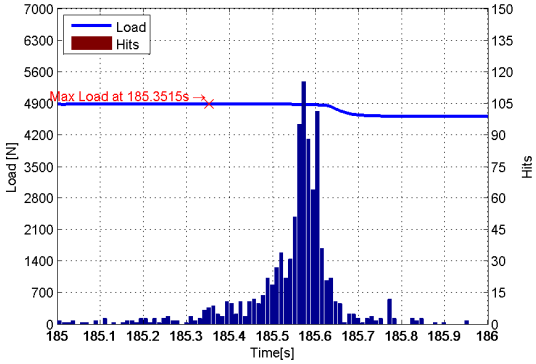

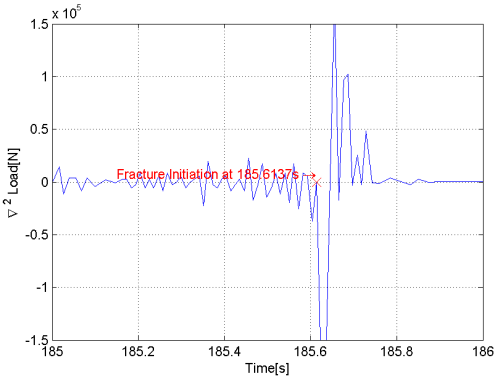

Figure E.2: *The measured time of FI has been defined as the first point at which significant deviation occurs on the $\nabla^2 Load$ vs Time curve (this is marked by a red cross)*

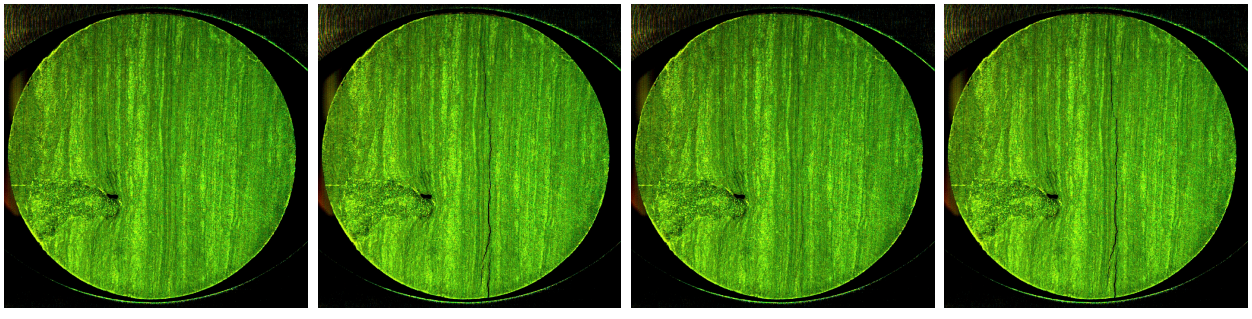

(a) UTS (b) Measured FI (c) Observed Fracture (d) 0.01s after (b)

Figure E.3: *High speed images taken at (a) Measured Ultimate tensile strength (b) the measured fracture initiation point (c) the observed fracture initiation point and (d) Approx 0.01 s (i.e. the next recorded time value) after (b)*

E.3 Mancos Shale (dry) $\beta = 15°$

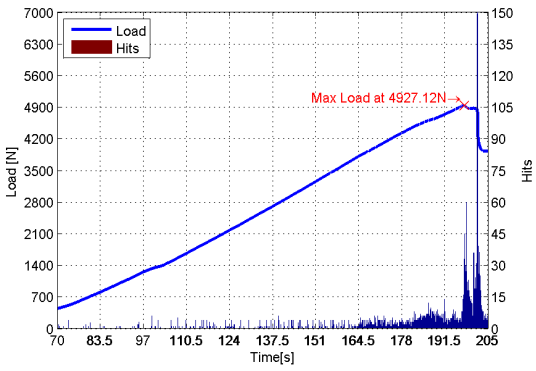

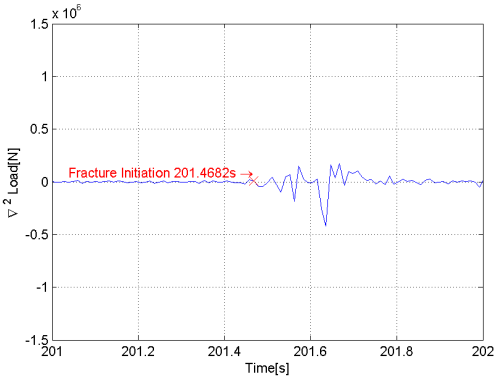

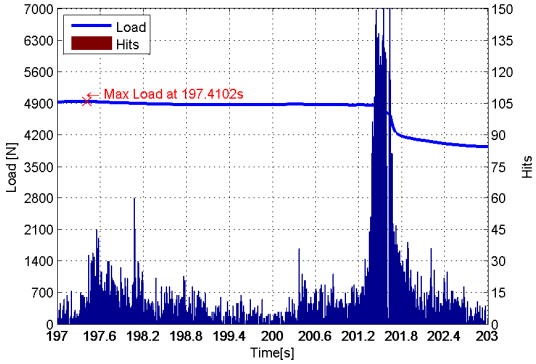

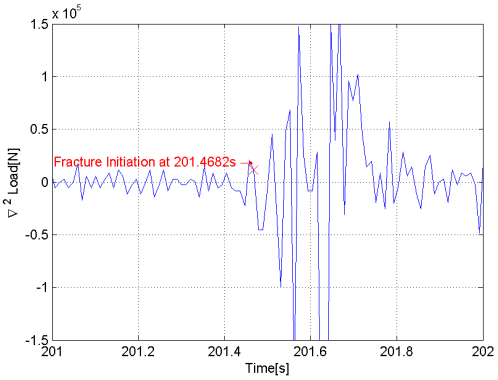

Figure E.4: *The measured time of Ultimate tensile stress has been defined as the point at maximum Load occurs on the Load vs Time curve (this is marked by a red cross)*

Figure E.5: *The measured time of FI has been defined as the first point at which significant deviation occurs on the $\nabla^2 Load$ vs Time curve (this is marked by a red cross)*

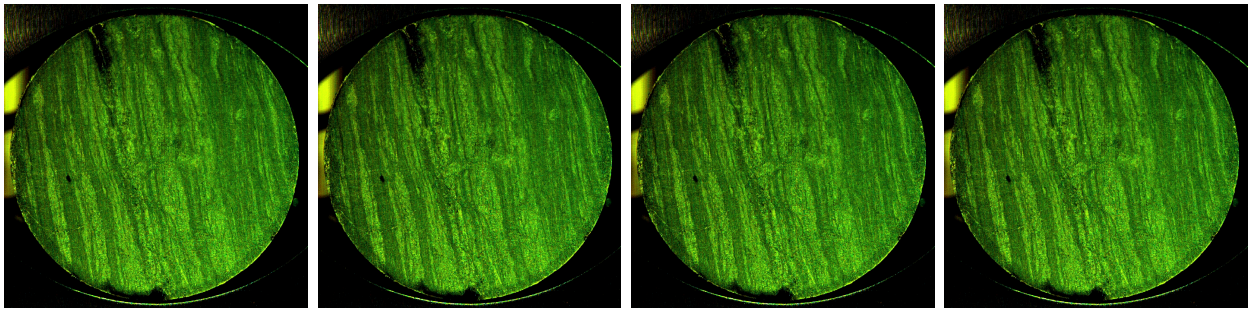

(a) UTS (b) Measured FI (c) Observed Fracture (d) 0.01s after (b)

Figure E.6: *High speed images taken at (a) Measured Ultimate tensile strength (b) the measured fracture initiation point (c) the observed fracture initiation point and (d) Approx 0.01 s (i.e. the next recorded time value) after (b)*

E.4 Mancos Shale (dry) $\beta = 30°$

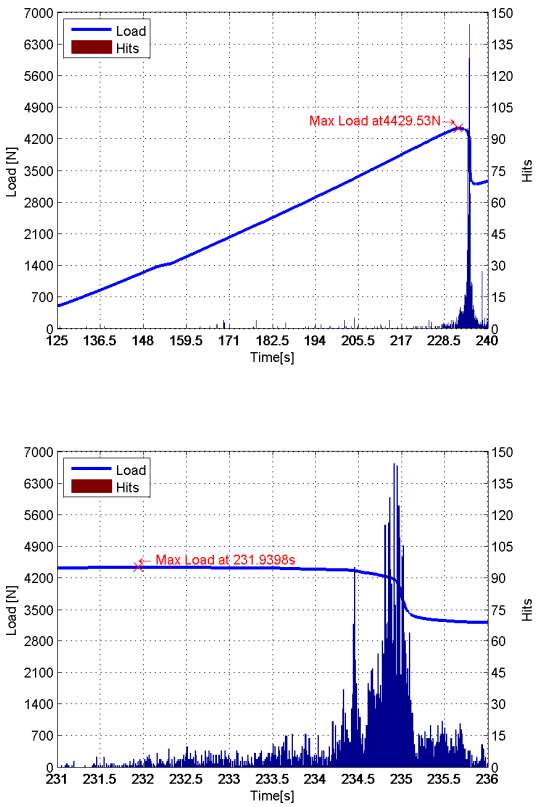

Figure E.7: *The measured time of Ultimate tensile stress has been defined as the point at maximum Load occurs on the Load vs Time curve (this is marked by a red cross)*

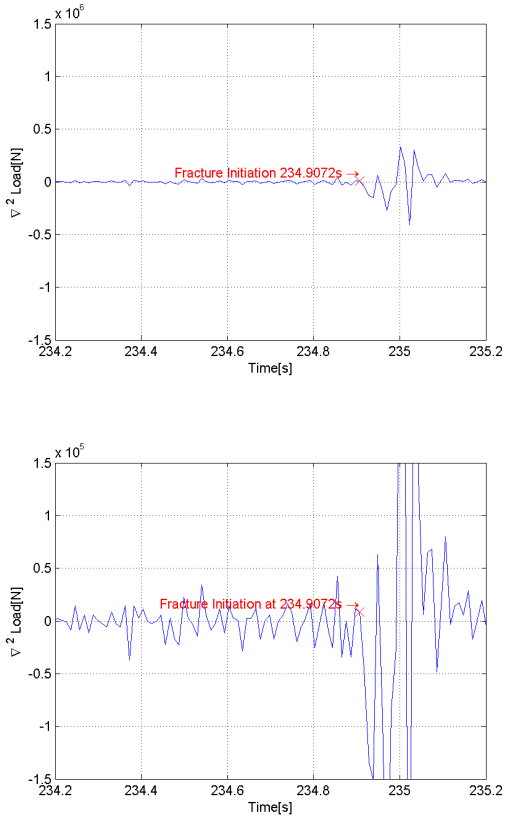

Figure E.8: *The measured time of FI has been defined as the first point at which significant deviation occurs on the $\nabla^2 Load$ vs Time curve (this is marked by a red cross)*

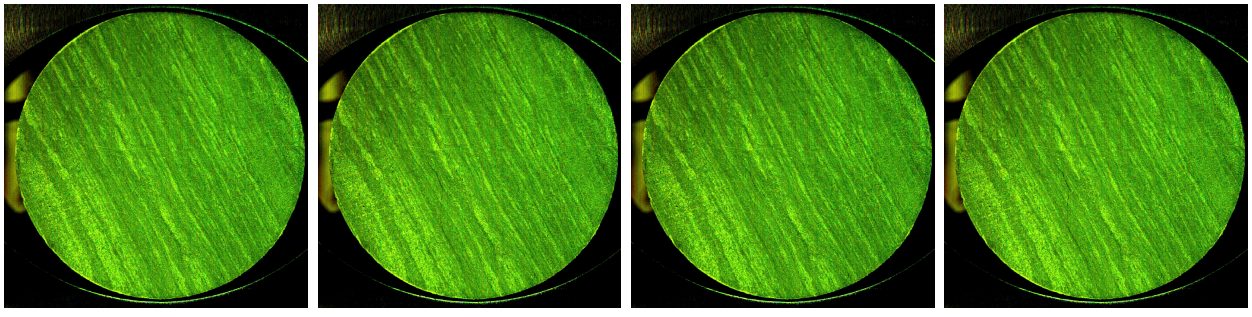

(a) UTS (b) Measured FI (c) Observed Fracture (d) 0.01s after (b)

Figure E.9: *High speed images taken at (a) Measured Ultimate tensile strength (b) the measured fracture initiation point (c) the observed fracture initiation point and (d) Approx 0.01 s (i.e. the next recorded time value) after (b)*

E.5 Mancos Shale (dry) $\beta = 45°$

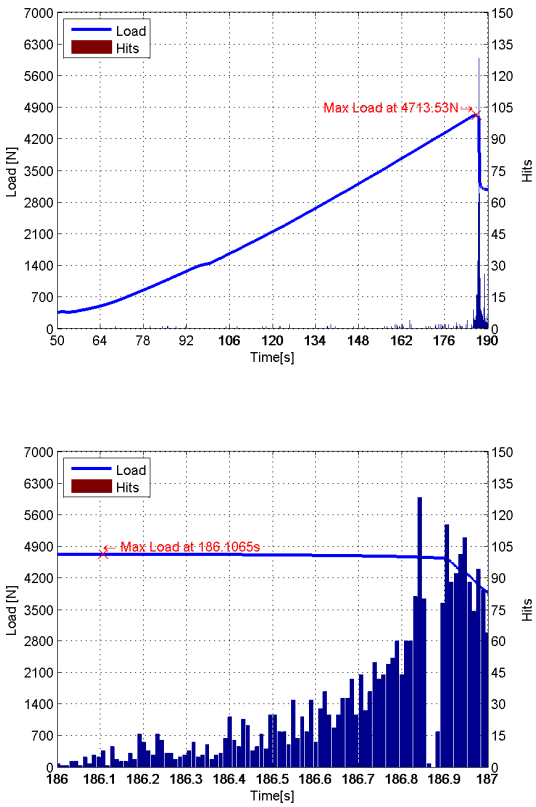

Figure E.10: *The measured time of Ultimate tensile stress has been defined as the point at maximum Load occurs on the Load vs Time curve (this is marked by a red cross)*

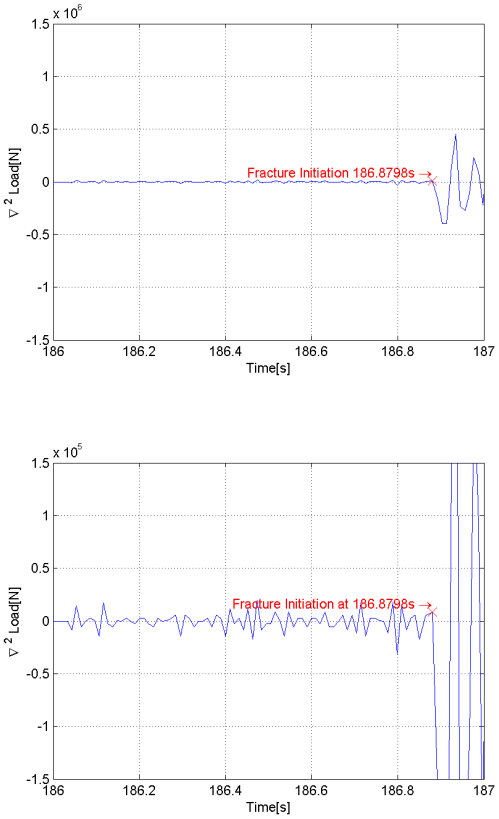

Figure E.11: *The measured time of FI has been defined as the first point at which significant deviation occurs on the $\nabla^2 Load$ vs Time curve (this is marked by a red cross)*

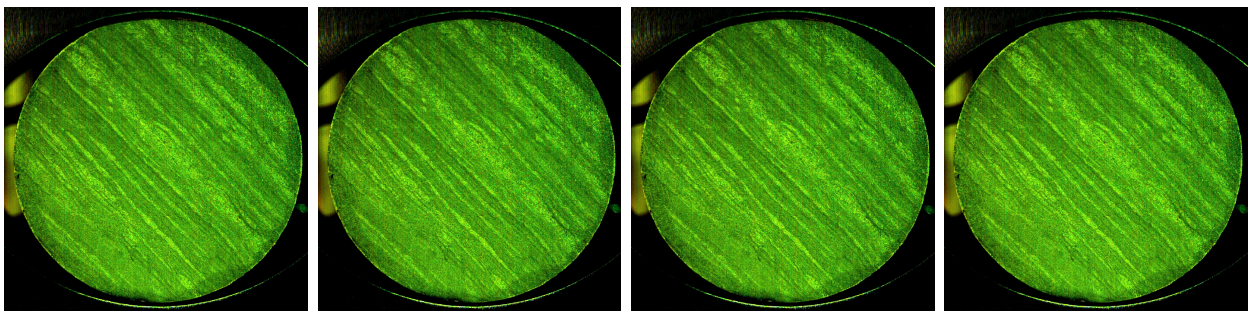

(a) UTS (b) Measured FI (c) Observed Fracture (d) 0.01s after (b)

Figure E.12: *High speed images taken at (a) Measured Ultimate tensile strength (b) the measured fracture initiation point (c) the observed fracture initiation point and (d) Approx 0.01 s (i.e. the next recorded time value) after (b)*

E.6 Mancos Shale (dry) $\beta = 60°$

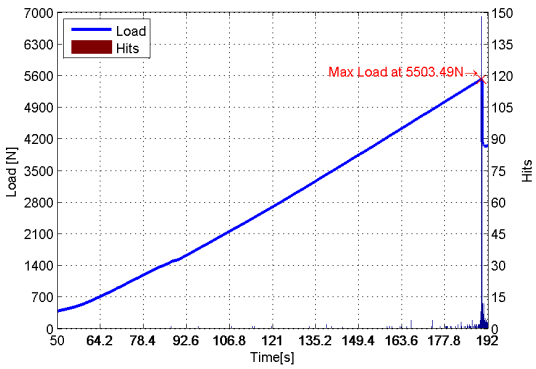

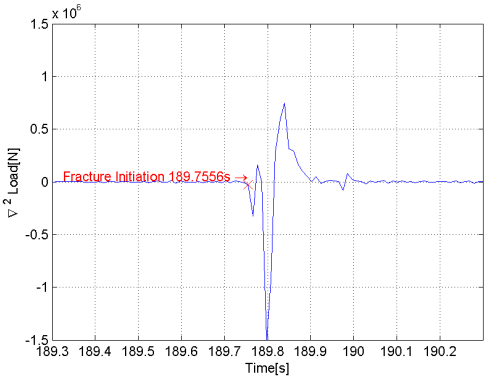

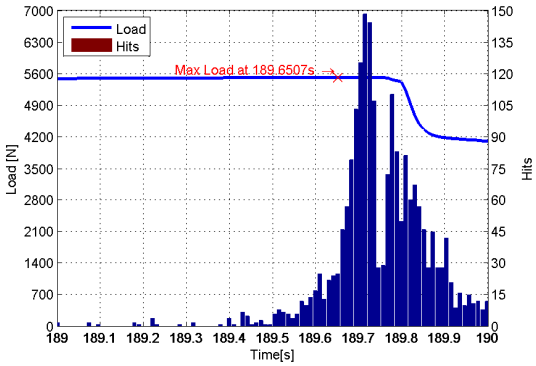

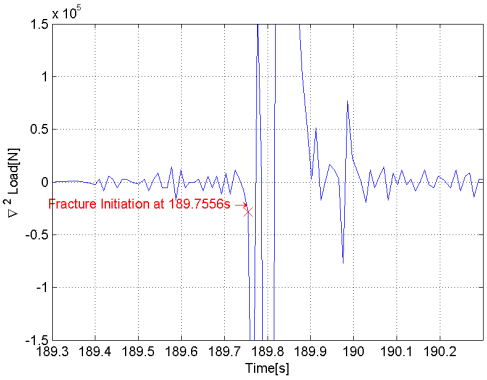

Figure E.13: *The measured time of Ultimate tensile stress has been defined as the point at maximum Load occurs on the Load vs Time curve (this is marked by a red cross)*

Figure E.14: *The measured time of FI has been defined as the first point at which significant deviation occurs on the $\nabla^2 Load$ vs Time curve (this is marked by a red cross)*

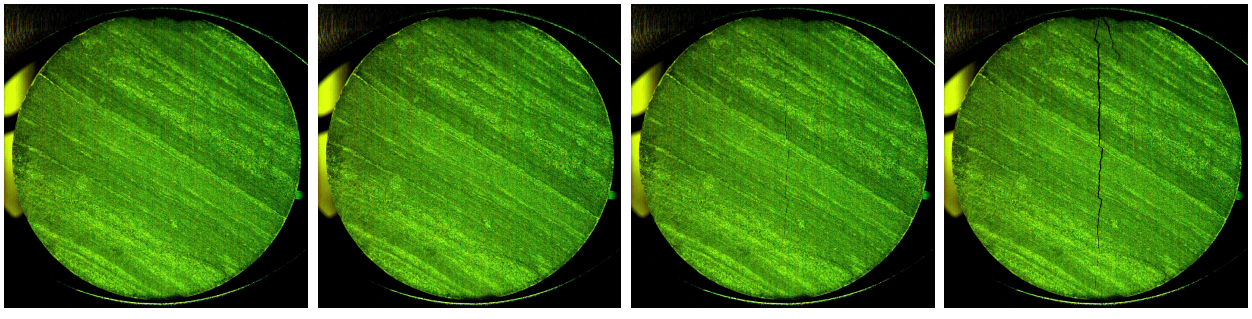

(a) UTS (b) Measured FI (c) Observed Fracture (d) 0.01s after (b)

Figure E.15: *High speed images taken at (a) Measured Ultimate tensile strength (b) the measured fracture initiation point (c) the observed fracture initiation point and (d) Approx 0.01 s (i.e. the next recorded time value) after (b)*

E.7 Mancos Shale (dry) $\beta = 75°$

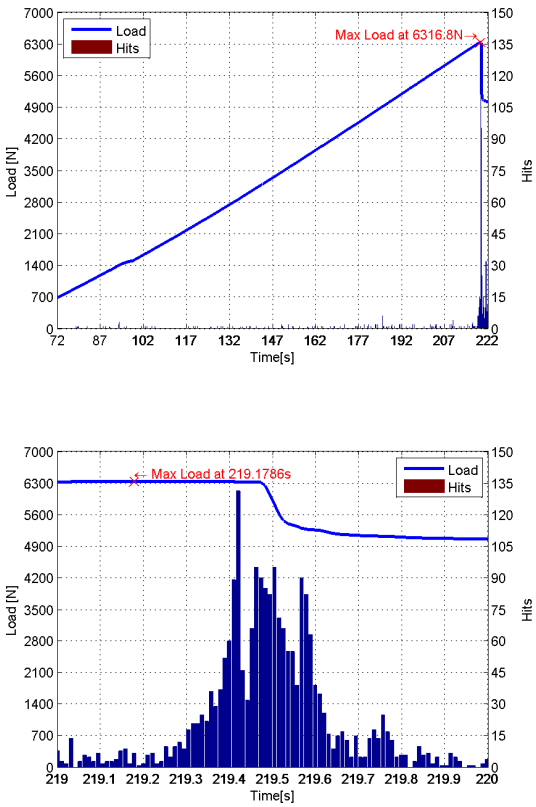

Figure E.16: *The measured time of Ultimate tensile stress has been defined as the point at maximum Load occurs on the Load vs Time curve (this is marked by a red cross)*

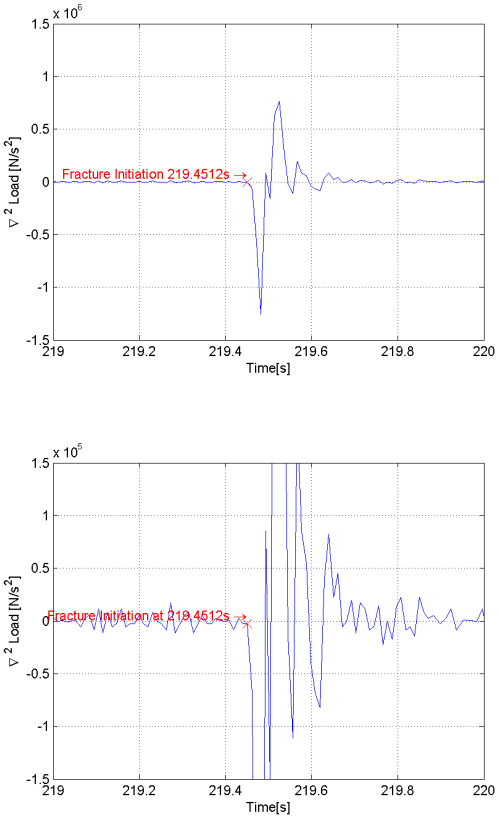

Figure E.17: *The measured time of FI has been defined as the first point at which significant deviation occurs on the $\bigtriangledown^2 Load$ vs Time curve (this is marked by a red cross)*

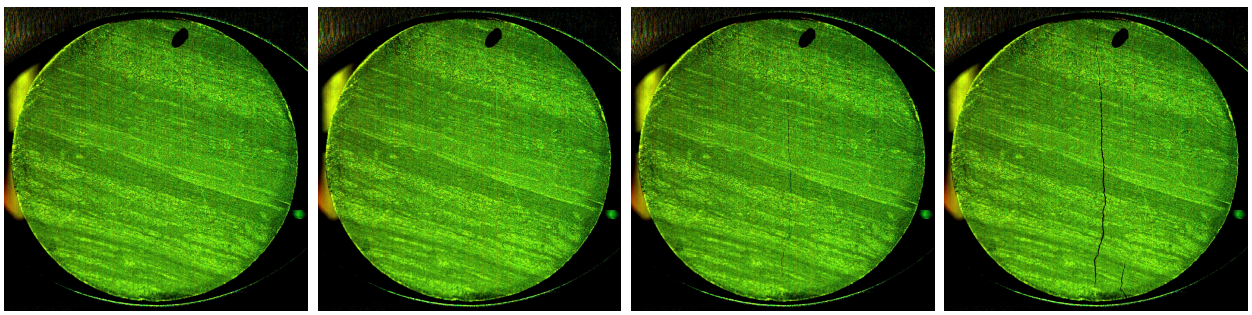

(a) UTS (b) Measured FI (c) Observed Fracture (d) 0.01s after (b)

Figure E.18: *High speed images taken at (a) Measured Ultimate tensile strength (b) the measured fracture initiation point (c) the observed fracture initiation point and (d) Approx 0.01 s (i.e. the next recorded time value) after (b)*

E.8 Mancos Shale (dry) $\beta = 90°$

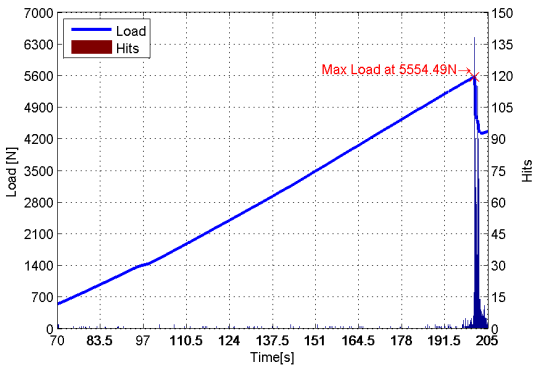

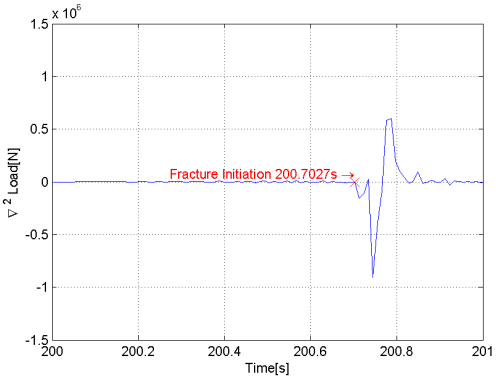

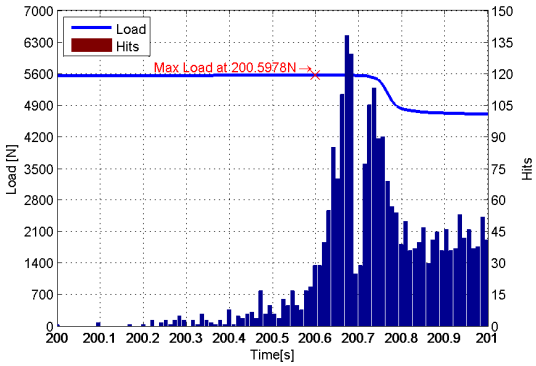

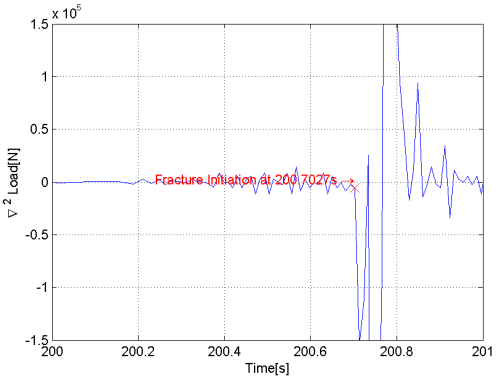

Figure E.19: *The measured time of Ultimate tensile stress has been defined as the point at maximum Load occurs on the Load vs Time curve (this is marked by a red cross)*

Figure E.20: *The measured time of FI has been defined as the first point at which significant deviation occurs on the $\nabla^2 Load$ vs Time curve (this is marked by a red cross)*

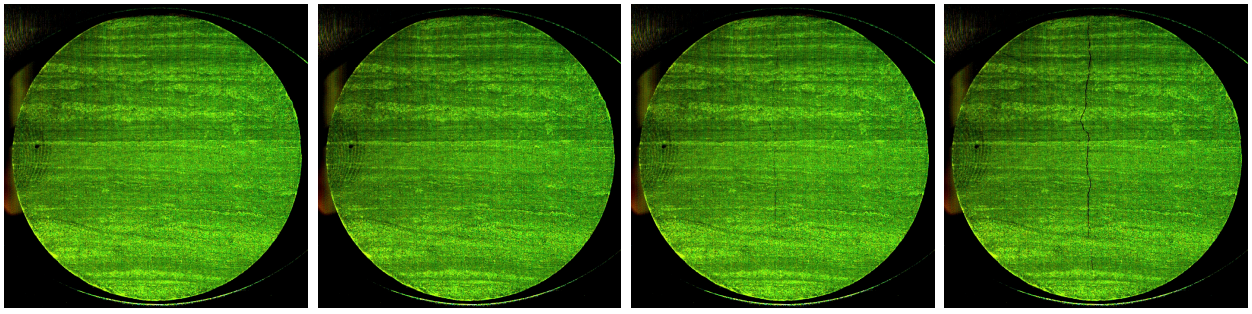

(a) UTS (b) Measured FI (c) Observed Fracture (d) 0.02s after (b)

Figure E.21: *High speed images taken at (a) Measured Ultimate tensile strength (b) the measured fracture initiation point (c) the observed fracture initiation point and (d) Approx 0.02 s (i.e. the second recorded time value) after (b)*

Appendix F

Location Map Results

F.1 Mancos Shale (dry) $\beta = 0°$

Location Map Before UTS

There were no location events generated 0.5 seconds before UTS (calculated using Vallen Software, isotropic model and a velocity of 4059m/s).

Location Map After UTS

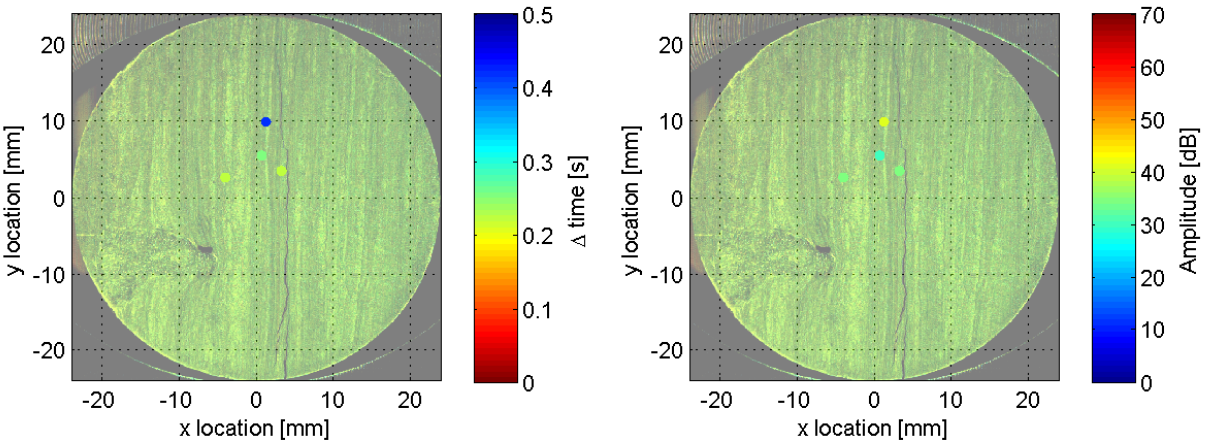

(a) Time Scale

(b) Amplitude Scale

Figure F.1: Location map at 0.5 seconds after UTS (calculated using Vallen Software, isotropic model and a velocity of 4059m/s)

F.2 Mancos Shale (dry) $\beta = 15°$

Location Map Before UTS

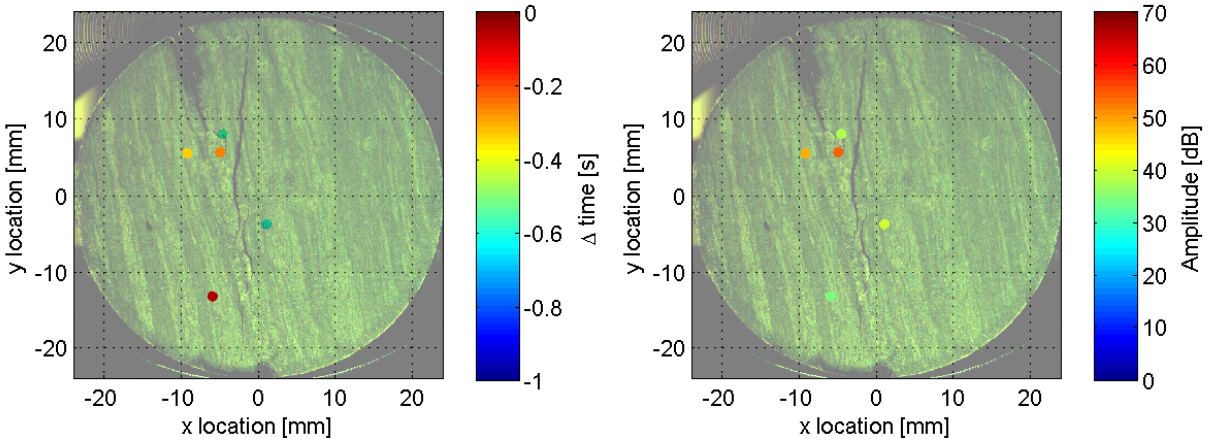

(a) Time Scale (b) Amplitude Scale

Figure F.2: Location map at 1.0 second prior to UTS (calculated using Vallen Software, isotropic model and a velocity of 4309m/s)

Location Map After UTS

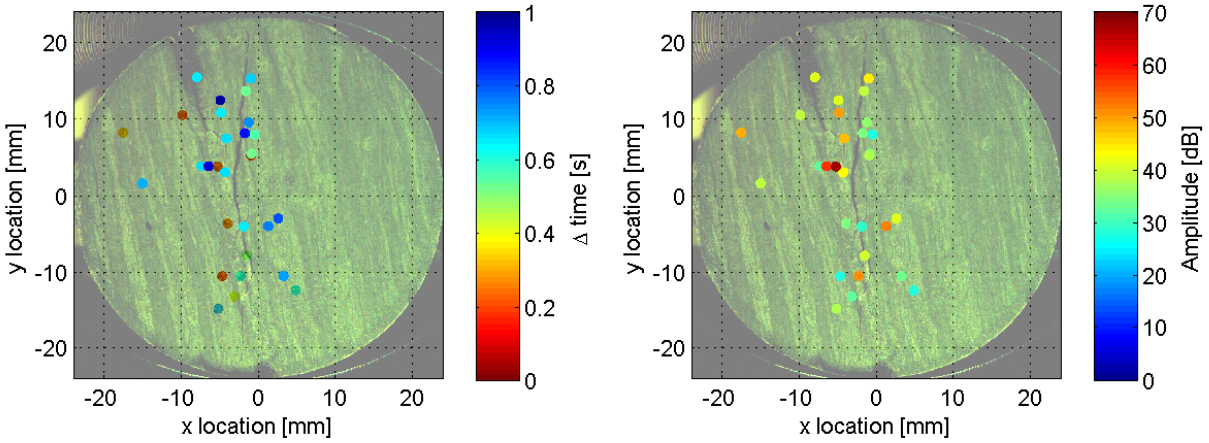

(a) Time Scale (b) Amplitude Scale

Figure F.3: Location map at 1.0 second after UTS (calculated using Vallen Software, isotropic model and a velocity of 4309m/s)

F.3 Mancos Shale (dry) $\beta = 30°$

Location Map Before UTS

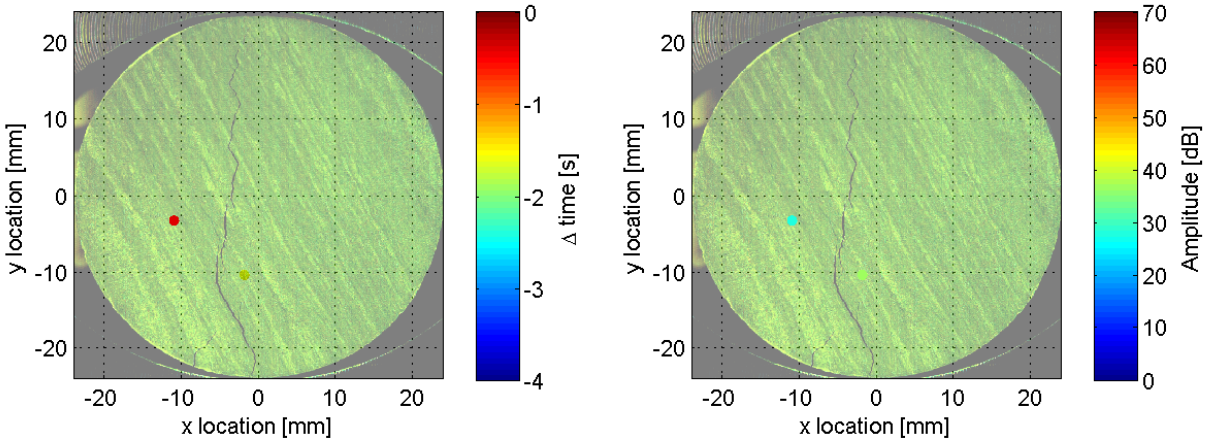

(a) Time Scale (b) Amplitude Scale

Figure F.4: Location map at 4.0 seconds prior to UTS (calculated using Vallen Software, isotropic model and a velocity of 3941m/s)

Location Map After UTS

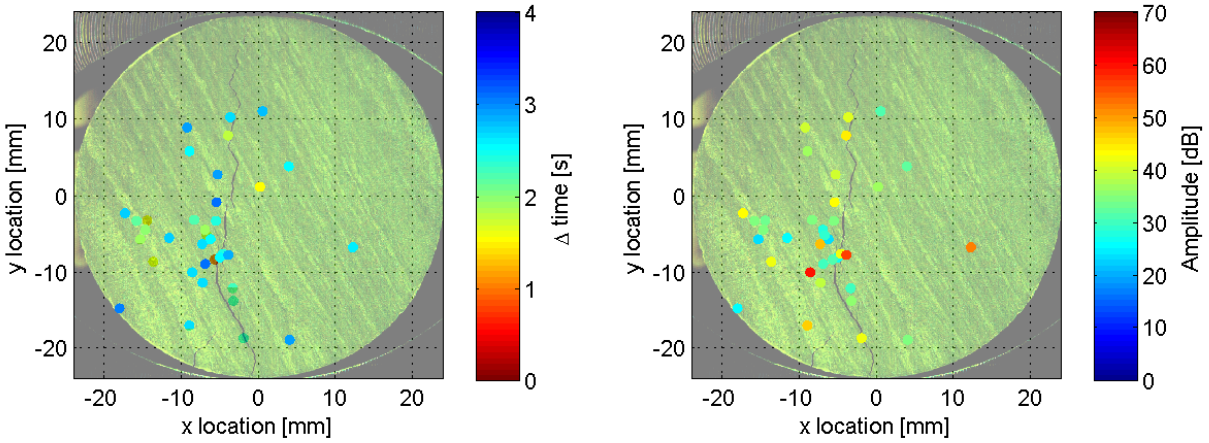

(a) Time Scale (b) Amplitude Scale

Figure F.5: Location map at 4.0 seconds after UTS (calculated using Vallen Software, isotropic model and a velocity of 3941m/s)

F.4 Mancos Shale (dry) $\beta = 45°$

Location Map Before UTS

There were no location events generated 1.0 second before UTS (calculated using Vallen Software, isotropic model and a velocity of 3851m/s).

Location Map After UTS

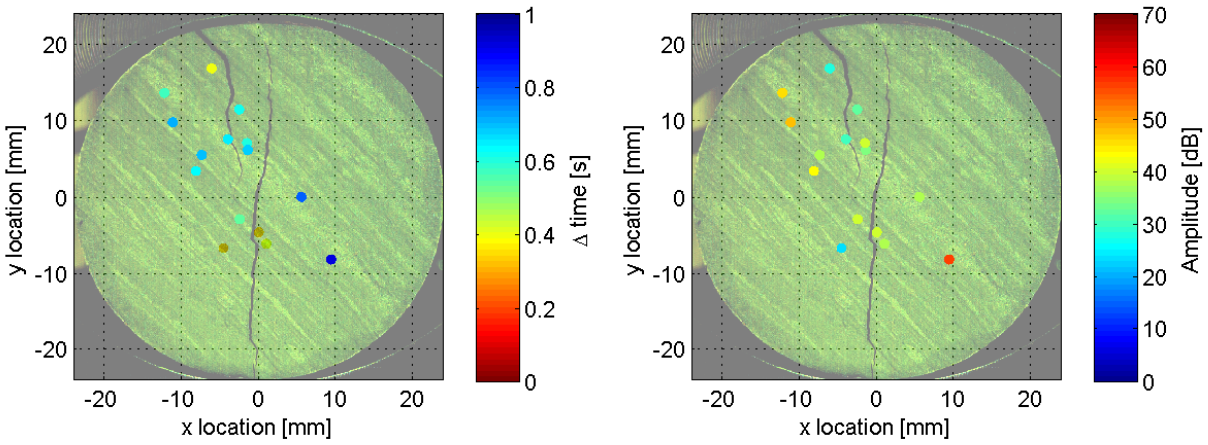

(a) Time Scale (b) Amplitude Scale

Figure F.6: Location map at 1.0 second after UTS (calculated using Vallen Software, isotropic model and a velocity of 3851m/s)

F.5 Mancos Shale (dry) $\beta = 60°$

Location Map Before UTS

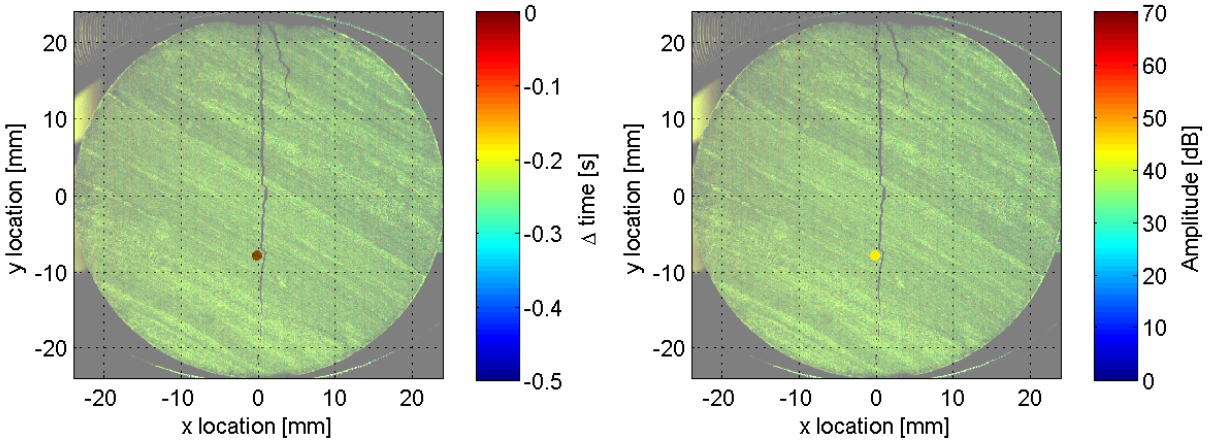

(a) Time Scale (b) Amplitude Scale

Figure F.7: Location map at 0.5 seconds prior to UTS (calculated using Vallen Software, isotropic model and a velocity of 3814m/s)

Location Map After UTS

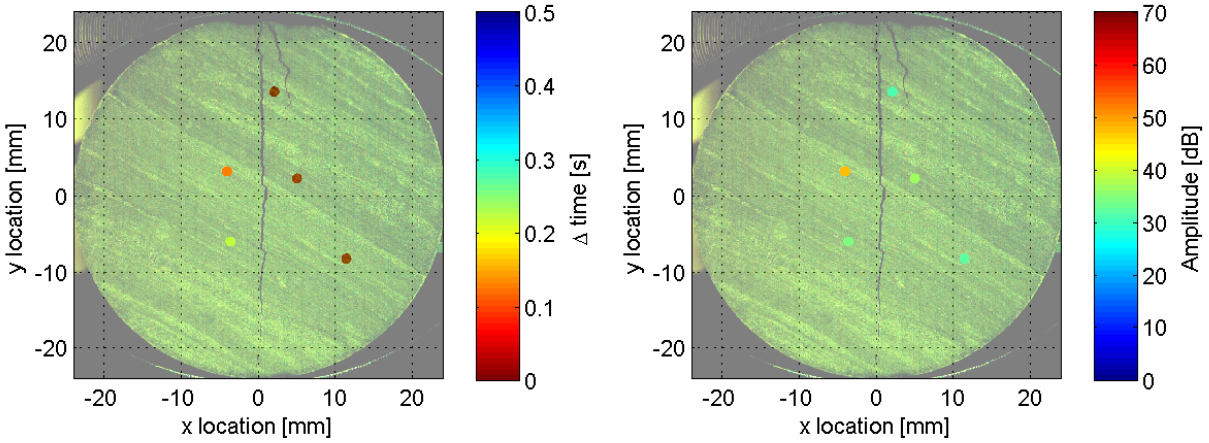

(a) Time Scale (b) Amplitude Scale

Figure F.8: Location map at 0.5 seconds after UTS (calculated using Vallen Software, isotropic model and a velocity of 3814m/s)

F.6 Mancos Shale (dry) $\beta = 75°$

Location Map Before UTS

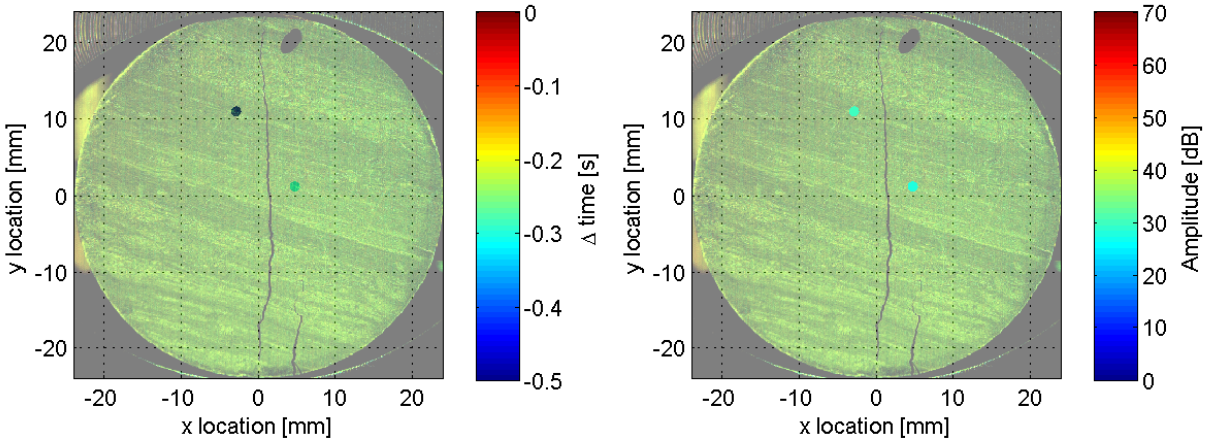

(a) Time Scale (b) Amplitude Scale

Figure F.9: Location map at 0.5 second prior to UTS (calculated using Vallen Software, isotropic model and a velocity of 3840m/s)

Location Map After UTS

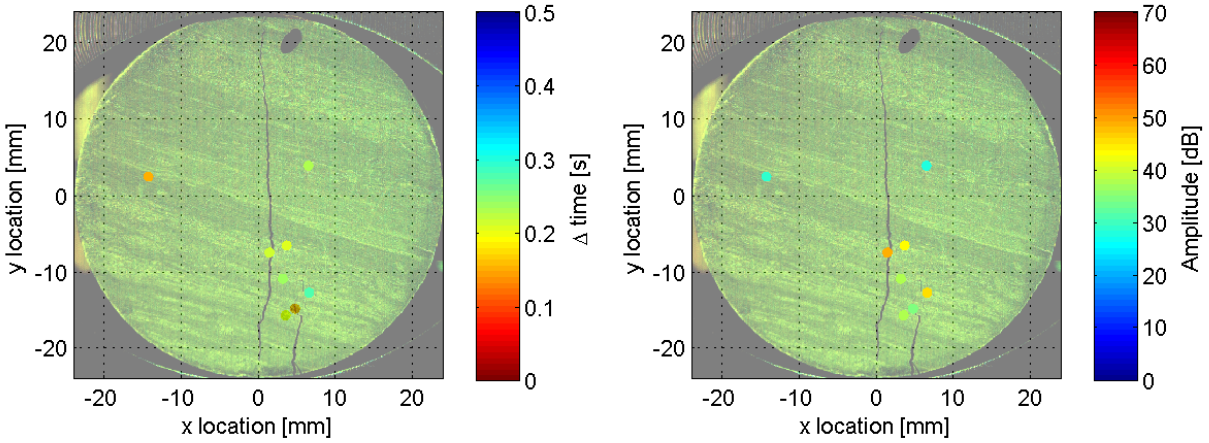

(a) Time Scale (b) Amplitude Scale

Figure F.10: Location map at 0.5 second after UTS (calculated using Vallen Software, isotropic model and a velocity of 3840m/s)

F.7 Mancos Shale (dry) $\beta = 90°$

Location Map Before UTS

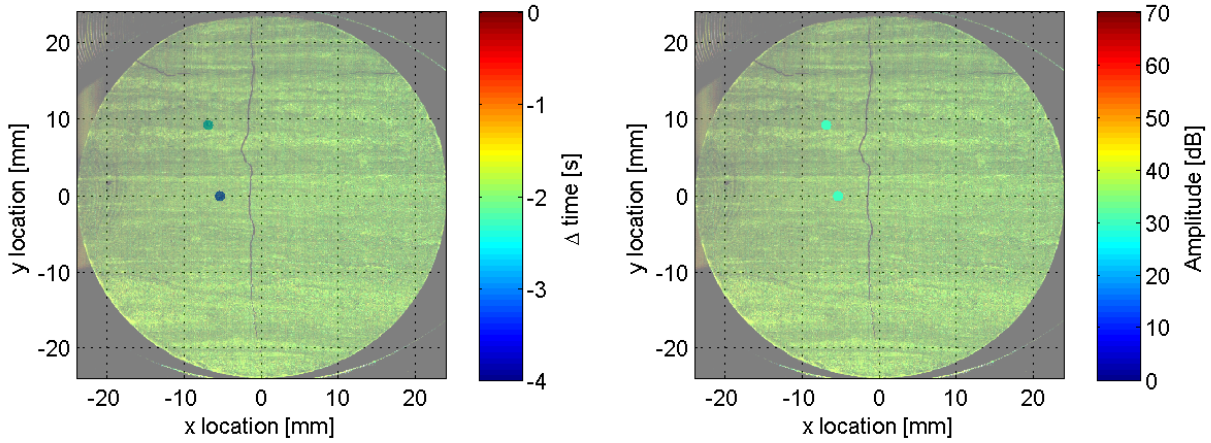

(a) Time Scale (b) Amplitude Scale

Figure F.11: Location map at 0.5 seconds prior to UTS (calculated using Vallen Software, isotropic model and a velocity of 3778m/s)

Location Map After UTS

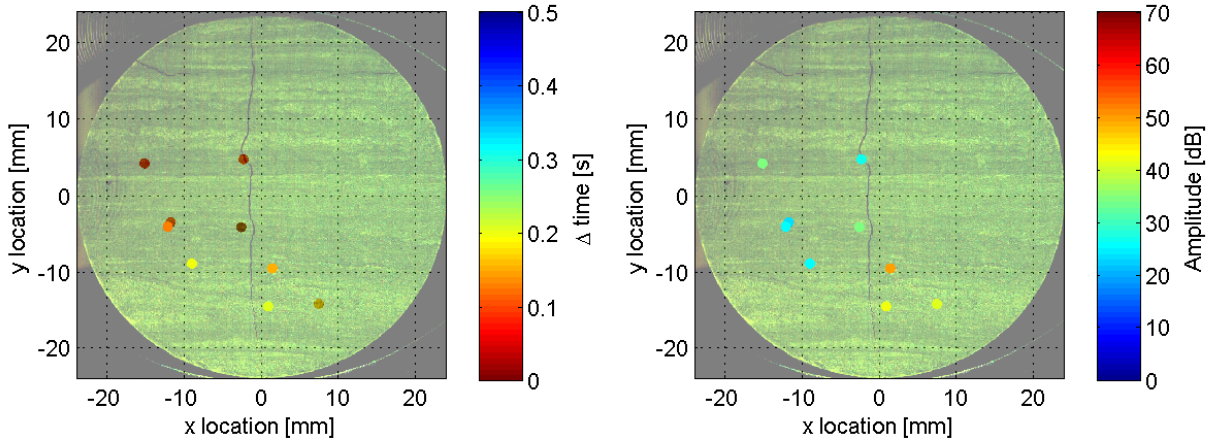

(a) Time Scale (b) Amplitude Scale

Figure F.12: Location map at 0.5 seconds after UTS (calculated using Vallen Software, isotropic model and a velocity of 3778m/s)

F.8 Castlegate Sandstone (dry)

Location Map Before UTS

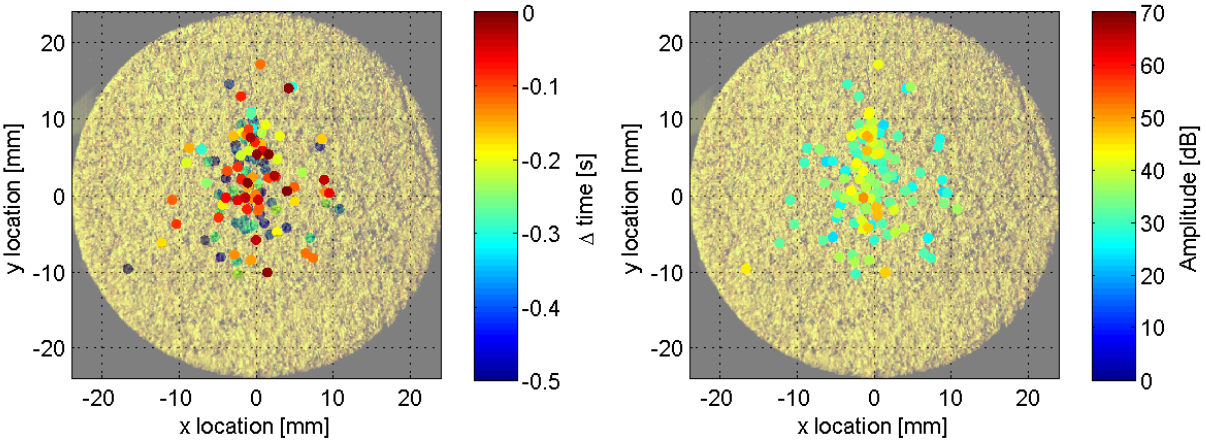

(a) Time Scale (b) Amplitude Scale

Figure F.13: Location map at 0.5 seconds prior to UTS (calculated using Vallen Software, isotropic model and a velocity of 1862m/s)

Location Map After UTS

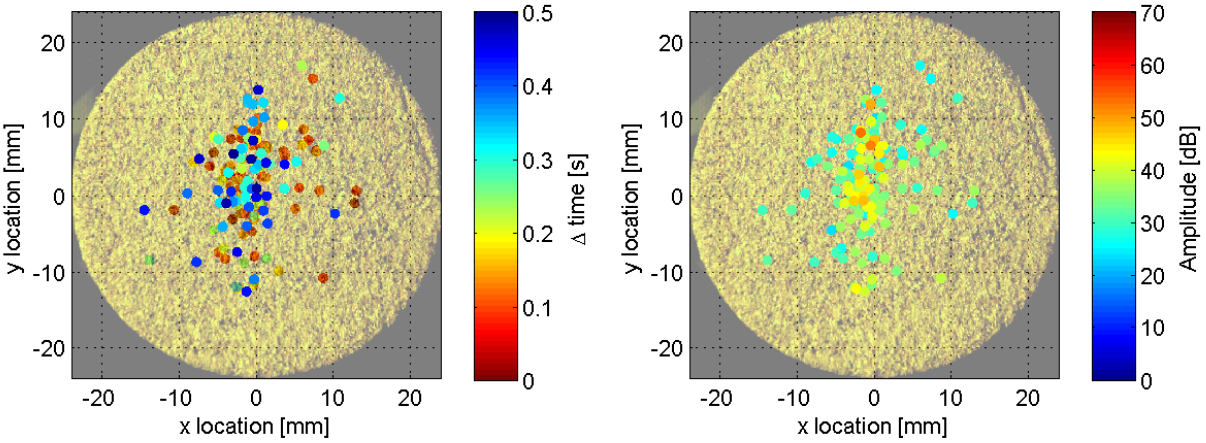

(a) Time Scale (b) Amplitude Scale

Figure F.14: Location map at 0.5 seconds after UTS (calculated using Vallen Software, isotropic model and a velocity of 1862m/s)

F.9 Mons Chalk (dry)

Location Map Before UTS

There were no location events generated 0.5 seconds before UTS (calculated using Vallen Software, isotropic model and a velocity of 2229m/s).

Location Map After UTS

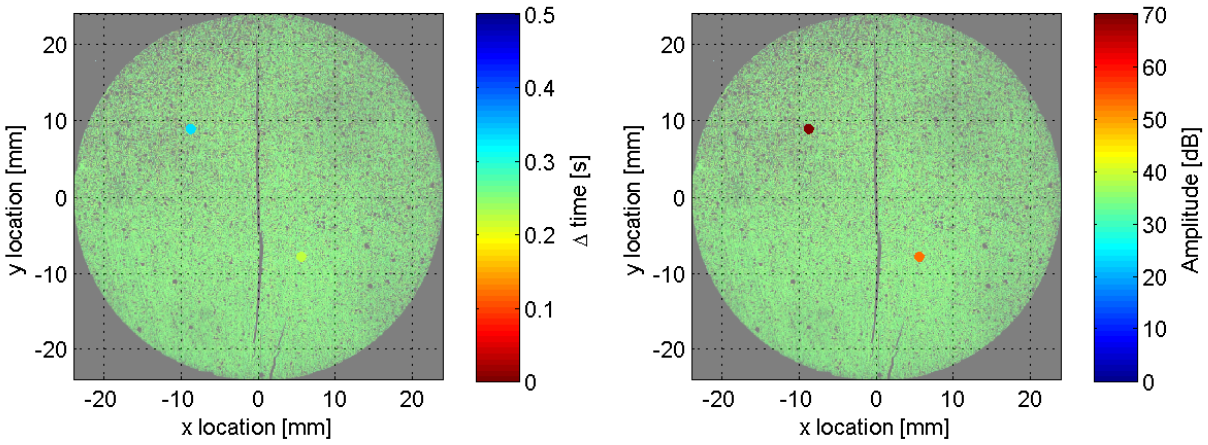

(a) Time Scale

(b) Amplitude Scale

Figure F.15: Location map at 0.5 seconds after UTS (calculated using Vallen Software, isotropic model and a velocity of 2229m/s)

F.10 Mons Chalk (sat)

Location Map Before UTS

There were no location events generated second before UTS (calculated using Vallen Software, isotropic model and a velocity of 1978m/s).

Location Map After UTS

There were no location events generated after UTS (calculated using Vallen Software, isotropic model and a velocity of 1978m/s).

Appendix G

Fracture Propagation Time

G.1 Mancos Shale (dry) $\beta = 0°$

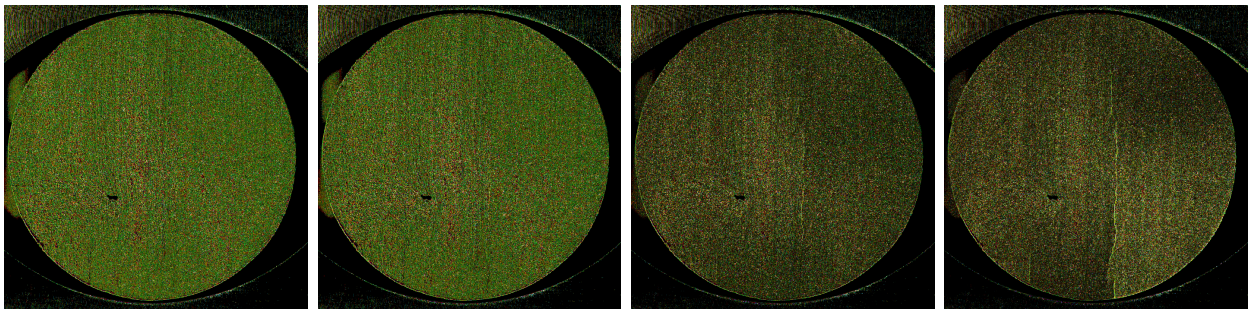

(a) t=0.0000s (b) t=0.0018s (c) t=0.0038s (d) t=0.0058s

Figure G.1: *Fracture propagation sequence for Mancos Shale,* $\beta = 0°$

G.2 Mancos Shale (dry) $\beta = 15°$

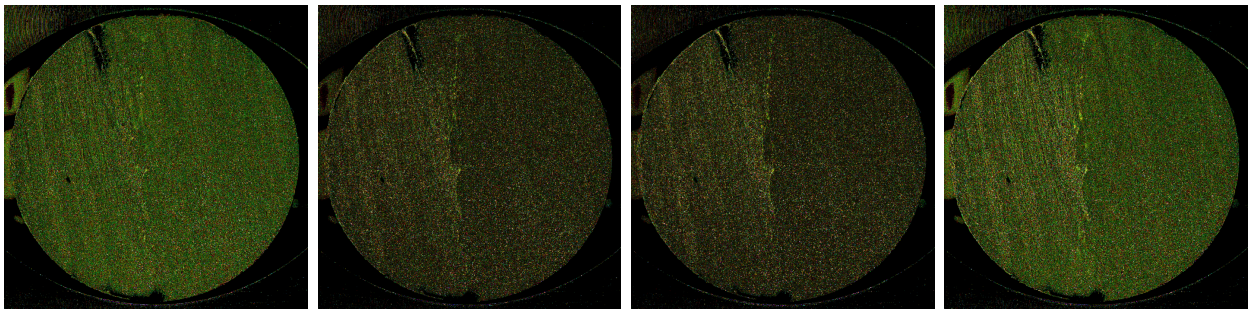

(a) t=0.0000s (b) t=0.0060s (c) t=0.0120s (d) t=0.0200s

Figure G.2: *Fracture propagation sequence for Mancos Shale,* $\beta = 15°$

G.3 Mancos Shale (dry) $\beta = 30°$

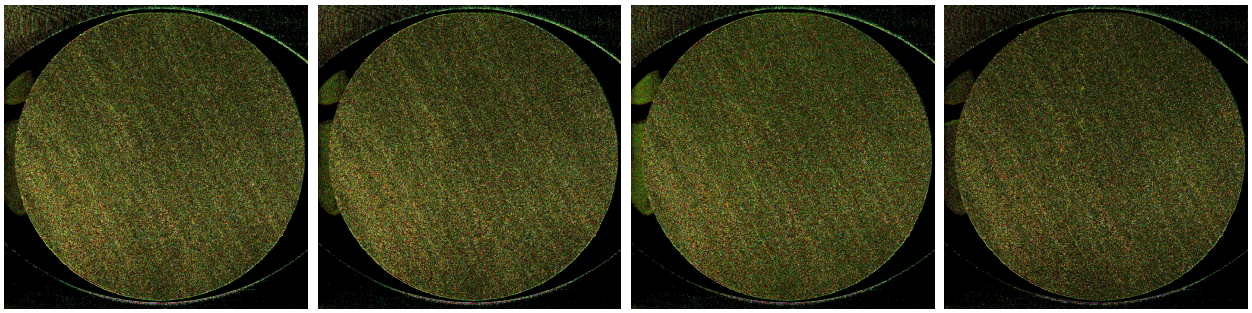

(a) t=0.0000s (b) t=0.0052s (c) t=0.0112s (d) t=0.0172s

Figure G.3: *Fracture propagation sequence for Mancos Shale,* $\beta = 30°$

G.4 Mancos Shale (dry) $\beta = 45°$

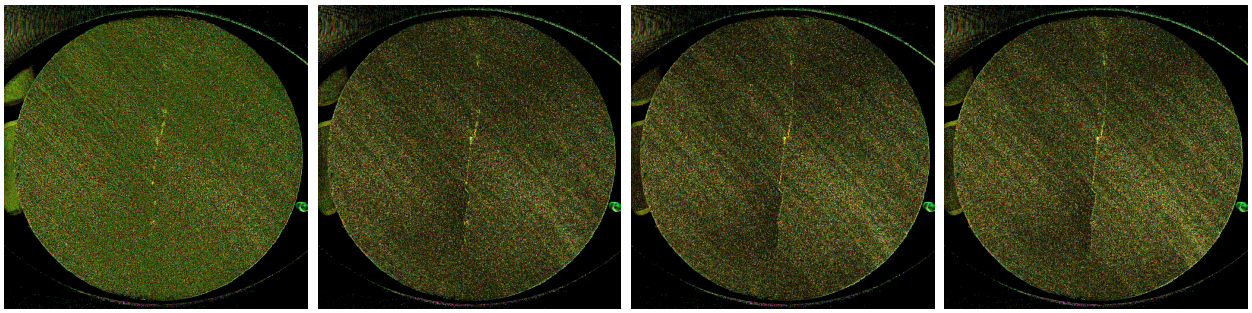

(a) t=0.0000s (b) t=0.0022s (c) t=0.0042s (d) t=0.0062s

Figure G.4: *Fracture propagation sequence for Mancos Shale,* $\beta = 45°$

G.5 Mancos Shale (dry) $\beta = 60°$

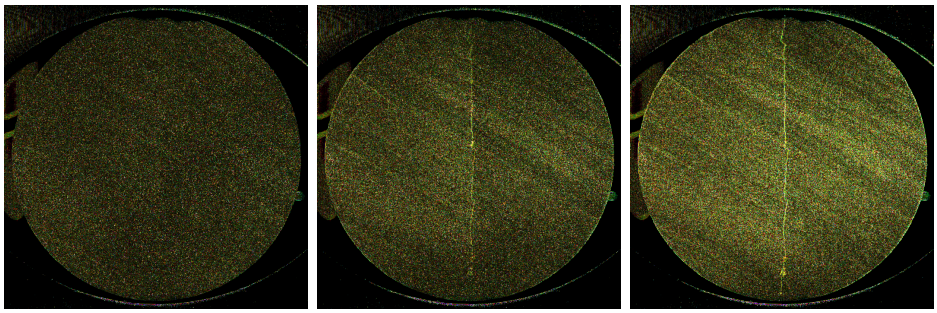

(a) t=0.0000s (b) t=0.0002s (c) t=0.0004s

Figure G.5: *Fracture propagation sequence for Mancos Shale,* $\beta = 60°$

G.6 Mancos Shale (dry) $\beta = 75°$

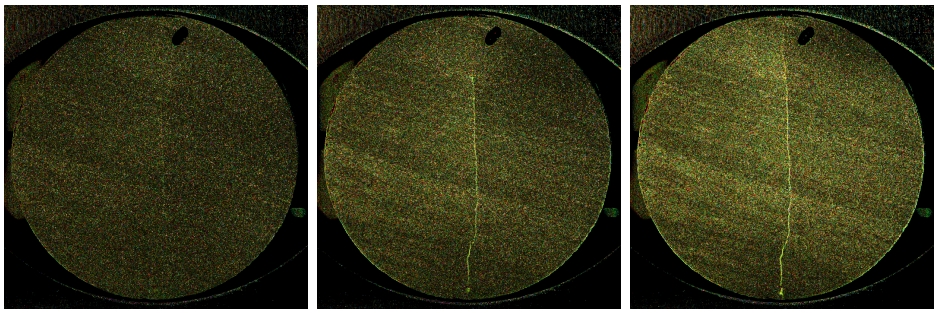

(a) t=0.0000s (b) t=0.0002s (c) t=0.0004s

Figure G.6: *Fracture propagation sequence for Mancos Shale,* $\beta = 75°$

G.7 Mancos Shale (dry) $\beta = 90°$

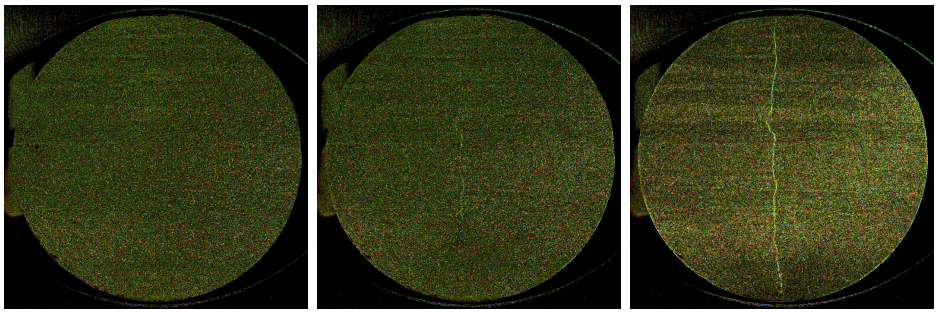

(a) t=0.0000s (b) t=0.0002s (c) t=0.0004s

Figure G.7: *Fracture propagation sequence for Mancos Shale,* $\beta = 90°$

Appendix H

Fracture Patterns Including Images

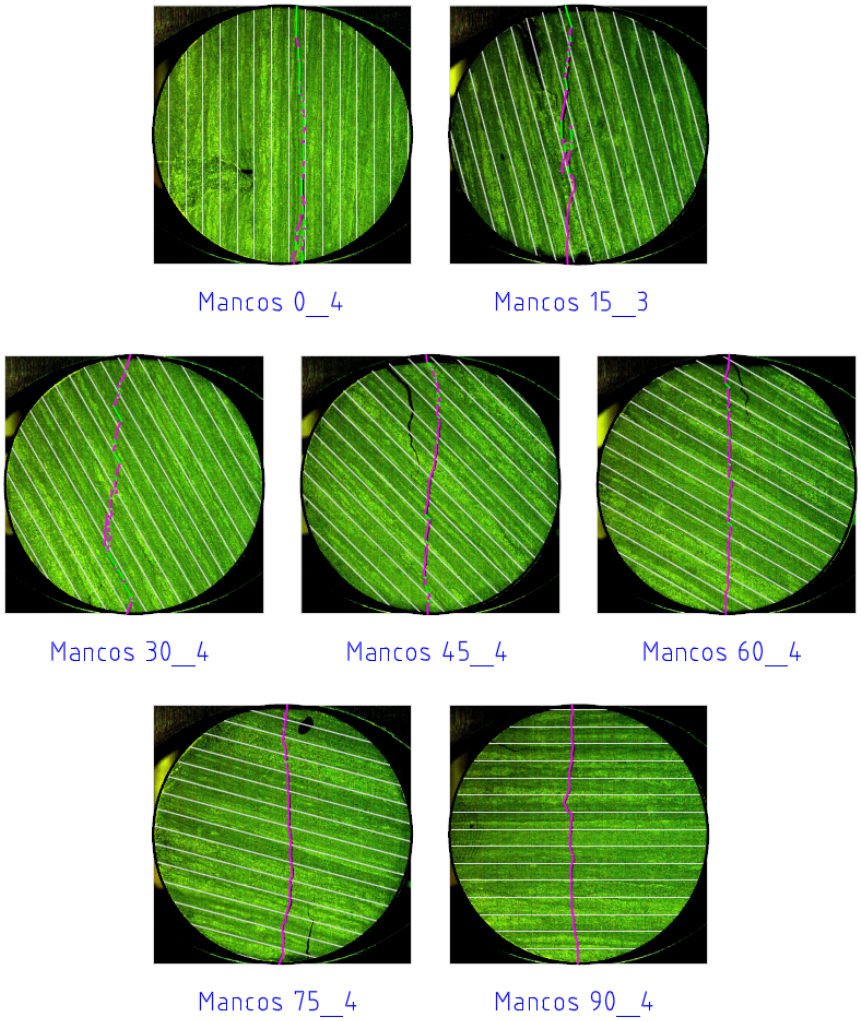

Figure H.1: *Fracture patterns of the 'central region' after diametrical loading of disk shaped Mancos Shale samples for different inclination angles, β. Fracture patterns are overlayed on digital images. The parallel thin grey lines indicate the layer direction (D=48mm), Layer Activation is represented in green and central fractures in magenta. Note that non-central fractures were not investigated in this analysis.*

Bibliography

Adobe. Photoshop C6, 2013. URL http://www.photoshop.com/.

Naser a. Al-Shayea. Crack propagation trajectories for rocks under mixed mode I–II fracture. *Engineering Geology*, 81(1):84–97, September 2005. ISSN 00137952. doi: 10.1016/j.enggeo.2005.07.013. URL http://linkinghub.elsevier.com/retrieve/pii/S0013795205001614.

Alberta Geological Survey. What is Shale Gas?, 2012. URL http://www.ags.gov.ab.ca/energy/shale-gas/.

Dirk Aljets, Alex Chong, Steve Wilcox, and Karen Holford. Acoustic Emission Source Location in Plate-Like Structures Using a Closely Arranged Triangular Sensor Array. *Journal of Acoustic Emission*, 28:85–98, 2010.

R Altindag. Correlation between P-wave velocity and some mechanical properties for sedimentary rocks. *The Journal of The Southern African Institute of Mining and Metallurgy*, 112(March):229–237, 2012.

B. Amadei, J.D. Rogers, and R.E. Goodman. Elastic Constants and Tensile Strength of Anisotropic Rocks. In *5th ISRM Congress*, pages 189–196, Melbourne, Australia, 1983. International Society for Rock Mechanics. URL http://www.onepetro.org/mslib/servlet/onepetropreview?id=ISRM-5CONGRESS-1983-030.

Apple Inc. Quicktime 7, 2013. URL http://www.apple.com/quicktime/.

Phil Armstrong, Bill Chmela, Kevin Dodds, Douglas Miller, Brian Hornby, Scott Leaney, and Heloise Lynn. The Promise of Elastic Anisotropy. Technical report, OilField Review, 1994.

AutoDesk. AutoCAD, 2013. URL http://www.autodesk.com/.

Vivek Bakshi. *Shale Gas and Other Unconventional Resources: A Practitioners Guide*. Globe Law and Business, 2012. ISBN 1905783809.

Nasina Balasubrahmanyam. Numerical Modelling in Geomechanics, 2011. URL http://www.authorstream.com/Presentation/nbalasubrahmanyam-971074-numerical-modelling-geomechanics/.

G. Barla. *Rock anisotropy: Theory and laboratory testing*, volume 13. Springer-Verlag, New York, l. muller edition, 1974.

Nick Barton. *Rock Quality, Seismic Velocity, Attenuation and Anisotropy*. Taylor & Francis, London, illustrate edition, October 2007. ISBN 9780203964453. doi: 10.1201/9780203964453.

M. Cai and P.K. Kaiser. Numerical simulation of the Brazilian test and the tensile strength of anisotropic rocks and rocks with pre-existing cracks. *International Journal of Rock Mechanics and Mining Sciences*, 41(3):450–451, April 2004. ISSN 13651609. doi: 10.1016/j.ijrmms.2003.12.111. URL http://linkinghub.elsevier.com/retrieve/pii/S136516090300220X.

Daniel Casem, Tusit Weerasooriya, and Paul Moy. Brazilian Testing of Brittle Materials. In *2007 SEM Annual Conference & Exposition on Experimental and Applied Mechanics*, pages 1–2, Columbus Ohio, 2007. Society for Experimental Mechanics. URL http://sem-proceedings.com/07s/sem.org-2007-SEM-Ann-Conf-s61p02-Brazilian-Testing-Brittle-Materials.pdf.

Chao-Shi Chen, Ernian Pan, and Bernard Amadei. Determination of deformability and tensile strength of anisotropic rock using Brazilian tests. *International Journal of Rock Mechanics and Mining Sciences*, 35(1):43–61, January 1998a. ISSN 13651609. doi: 10.1016/S0148-9062(97)00329-X. URL http://linkinghub.elsevier.com/retrieve/pii/S014890629700329X.

Chao-Shi Chen, Ernian Pan, and Bernard Amadei. Fracture mechanics analysis of cracked discs of anisotropic rock using the boundary element method. *International Journal of Rock Mechanics and Mining Sciences*, 35(2):195–218, March 1998b. ISSN 13651609. doi: 10.1016/S0148-9062(97)00330-6. URL http://linkinghub.elsevier.com/retrieve/pii/S0148906297003306.

S. Chen, Z.Q. Yue, and L.G. Tham. Digital image-based numerical modeling method for prediction of inhomogeneous rock failure. *International Journal of Rock Mechanics and Mining Sciences*, 41(6):939–957, September 2004. ISSN 13651609. doi: 10.1016/j.ijrmms.2004.03.002. URL http://linkinghub.elsevier.com/retrieve/pii/S1365160904002114.

Jung-Woo Cho, Hanna Kim, Seokwon Jeon, and Ki-Bok Min. Deformation and strength anisotropy of Asan gneiss, Boryeong shale, and Yeoncheon schist. *International Journal of Rock Mechanics and Mining Sciences*, 50:158–169, February 2012. ISSN 13651609. doi: 10.1016/j.ijrmms.2011.12.004. URL http://linkinghub.elsevier.com/retrieve/pii/S1365160911002176.

K.P. Chong, J.L. Chen, G. F. Dana, and J. A. Weber. Indirect and Direct Tensile Behavior of Devonian Oil Shales. Technical report, U.S. Department of Energy, Laramie, 1984.

J Claesson and B Bohloli. Brazilian test: stress field and tensile strength of anisotropic rocks using an analytical solution. *International Journal of Rock Mechanics and Mining Sciences*, 39(8):991–1004, December 2002. ISSN 13651609. doi: 10.1016/S1365-1609(02)00099-0. URL http://linkinghub.elsevier.com/retrieve/pii/S1365160902000990.

P. S. B. Colback. An analysis of brittle fracture initiation and propagation in the Brazilian test. In *1st ISRM Congress*, pages 385–391, Lisbon, 1966. International Society for

Rock Mechanics. URL http://www.onepetro.org/mslib/servlet/onepetropreview?id=ISRM-1CONGRESS-1966-066.

B. Debecker and A. Vervoort. Experimental observation of fracture patterns in layered slate. *International Journal of Fracture*, 159(1):51–62, August 2009. ISSN 0376-9429. doi: 10.1007/s10704-009-9382-z. URL http://link.springer.com/10.1007/s10704-009-9382-z.

Bjorn Debecker and André Vervoort. Localization by Acoustic Emission in Transversely Isotropic Slate. *Advances in Acoustics and Vibration*, pages 1–10, 2011. ISSN 1687-6261. doi: 10.1155/2011/735913. URL http://www.hindawi.com/journals/aav/2011/735913/.

Department of Mines and Petroleum. Gas Fact Sheet: Gas Resource Types, 2012. URL http://www.dmp.wa.gov.au/documents/121982_Gas_Fact_Sheet_Gas_Resources_Type.pdf.

DOE/EIA. Annual Energy Outlook 2012. Technical report, U.S. Energy Information Administration, Washington, 2012. URL http://www.worldenergyoutlook.org/publications/weo-2012/.

E. Fjaer, R.M. Holt, A.M. Raaen, R. Risnes, and P. Horsrud. *Petroleum Related Rock Mechanics*. Elesevier, 2 edition, 2008.

Efunda. Principal Stress, 2013. URL http://www.efunda.com/formulae/solid_mechanics/mat_mechanics/calc_principal_stress.cfm.

EIA. Review of Emerging Resources: U.S. Shale Gas and Shale Oil Plays. Technical Report July, U.S. Energy Information Administration, Washington, 2011a. URL http://www.eia.gov/analysis/studies/usshalegas/pdf/usshaleplays.pdf.

EIA. World Shale Gas Resources : An Initial Assessment of 14 Regions Outside the United States. Technical Report April, U.S. Department of Energy, Washington, 2011b. URL http://www.eia.gov/analysis/studies/worldshalegas/pdf/fullreport.pdf.

C. Fairhurst. On the validity of the 'Brazilian' test for brittle materials. *International Journal of Rock Mechanics and Mining Sciences & Geomechanics Abstracts*, 1(4):535–546, October 1964. ISSN 01489062. doi: 10.1016/0148-9062(64)90060-9. URL http://linkinghub.elsevier.com/retrieve/pii/0148906264900609.

Stephen Holditch. Tight Gas Sands. *Journal of Petroleum Technology*, 58(6):86–93, June 2006. ISSN 0149-2136. doi: 10.2118/103356-MS. URL http://www.onepetro.org/mslib/servlet/onepetropreview?id=SPE-103356-MS\&soc=SPE.

J.A. Hooper. The failure of glass cylinders in diametral compression. *Journal of the Mechanics and Physics of Solids*, 19(4):179–188, August 1971. ISSN 00225096. doi: 10.1016/0022-5096(71)90027-5. URL http://linkinghub.elsevier.com/retrieve/pii/0022509671900275.

C.-T. Hsieh and C.-L. Wang. The measurement of the crack propagation in rock slabs. In Ohnishi & Aoki, editor, *Proceesings of the ISRM International Symposium 3rd ARMS*, Rotterdam, 2004. Millpress.

J.A. Hudson, E.T. Brown, and F. Rummel. The controlled failure of rock discs and rings loaded in diametral compression. *International Journal of Rock Mechanics and Mining Sciences & Geomechanics Abstracts*, 9(2):241–248, March 1972. ISSN 01489062. doi: 10.1016/0148-9062(72)90025-3. URL http://linkinghub.elsevier.com/retrieve/pii/0148906272900253.

ISRM. Suggested methods for determining tensile strength of rock materials. *International Journal of Rock Mechanics and Mining Sciences & Geomechanics Abstracts*, 15 (3):99–103, June 1978. ISSN 01489062. doi: 10.1016/0148-9062(78)90003-7. URL http://linkinghub.elsevier.com/retrieve/pii/0148906278900037.

H. Jasarevic, A. Chudnovsky, J.W. Dudley, and G.K. Wong. Observation and Modeling of Brittle Fracture Initiation in a Micro-Heterogeneous Material. *International Journal of Fracture*, 158(1):73–80, June 2009. ISSN 0376-9429. doi: 10.1007/s10704-009-9365-0. URL http://link.springer.com/10.1007/s10704-009-9365-0.

L. Jing. A review of techniques, advances and outstanding issues in numerical modelling for rock mechanics and rock engineering. *International Journal of Rock Mechanics and Mining Sciences*, 40(3):283–353, April 2003. ISSN 13651609. doi: 10.1016/S1365-1609(03)00013-3. URL http://linkinghub.elsevier.com/retrieve/pii/S1365160903000133.

Chien-chung Ke, Chao-shi Chen, Cheng-yu Ku, and Chih-hao Chen. Modeling crack propagation path of anisotropic rocks using boundary element method. (7):1227–1253, 2009. doi: 10.1002/nag.

Ali Keneti and R. Wong. Investigation of Anisotropic Behavior of Montney Shale Under Indirect Tensile Strength Test. In *Proceedings of Canadian Unconventional Resources and International Petroleum Conference*. Society of Petroleum Engineers, October 2010. ISBN 9781555633127. doi: 10.2118/138104-MS. URL http://www.onepetro.org/mslib/servlet/onepetropreview?id=SPE-138104-MS\&soc=SPE.

Ole Ø ystein Knudsen, Astrid Bjø rgum, and Mario Polanco-Loria. Internal Stress and Mechanical Properties of Paint Films. In *NACE International*, number 07003, pages 1–9, Nashville, Tennessee, 2007. NACE International. URL http://www.onepetro.org/mslib/servlet/onepetropreview?id=NACE-07003.

Flavio Lanaro, Toshinori Sato, and Ove Stephansson. Microcrack modelling of Brazilian tensile tests with the boundary element method. *International Journal of Rock Mechanics and Mining Sciences*, 46(3):450–461, April 2009. ISSN 13651609. doi: 10.1016/j.ijrmms.2008.11.007. URL http://linkinghub.elsevier.com/retrieve/pii/S1365160908001809.

S. Lekhnitskii. *Anisotropic Plates*. Routledge, reprint edition, 1968. ISBN 0677206704.

Diyuan Li and Louis Ngai Yuen Wong. The Brazilian Disc Test for Rock Mechanics Applications: Review and New Insights. *Rock Mechanics and Rock Engineering*, 46(2): 269–287, May 2012. ISSN 0723-2632. doi: 10.1007/s00603-012-0257-7. URL http://link.springer.com/10.1007/s00603-012-0257-7.

Love High Speed. Lighting for High Speed, 2013. URL http://www.lovehighspeed.com/lighting-for-high-speed/.

O K Mahabadi, G Grasselli, and A Munjiza. Numerical modelling of a Brazilian Disc test of layered rocks using the combined finite-discrete element method. In *Proceedings of the 3rd CANUS Rock Mechanics Symposium*, volume 2009, pages 1–9, Toronto, 2009.

J.D. McLennan, J.C. Roegiers, and W.P. Marx. The Mancos Formation: An Evaluation of the Interaction of Geological Conditions. In *SPE/DOE 11606*, Denver, 1983. Society of Petroleum Engineers of AIME.

MHSC. *Updating Numerical Modelling Handbook*. Number March. Mine Health and Safety Council, Gauteng, 2000. URL http://www.mhsc.org.za/css/images/docs/Research/?dir=RockFalls/UpdatingofNumericalModellingHandbook.

G C Naik. Tight Gas Reservoirs – An Unconventional Natural Energy Source for the Future, 2002. URL http://www.pinedaleonline.com/socioeconomic/pdfs/tight_gas.pdf.

Katelyn M. Nash. *Shale Gas Development (Energy Science, Engineering and Technology)*. Nova Science Publishers, Inc., 2010. ISBN 161668545X.

Natural Gas. Unconventional Natural Gas Resources, 2011. URL http://www.naturalgas.org/overview/unconvent_ng_resource.asp.

Gabriel L. Navarro. *Marcellus Shale and Shale Gas: Facts and Considerations (Earth Sciences in the 21st Century-Gases-Characteristics, Types and Properties)*. Nova Science Publishers, Inc., 2012. ISBN 1614701733.

OECD/EIA. Are We Entering A Golden Age of Gas? Technical report, International Energy Agency, Paris, 2011. URL http://www.worldenergyoutlook.org/media/weowebsite/2011/WEO2011_GoldenAgeofGasReport.pdf.

OECD/IEA. Golden Rules for a Golden Age of Gas. Technical report, International Energy Agency, Paris, 2012. URL http://www.worldenergyoutlook.org/media/weowebsite/2012/goldenrules/WEO2012_GoldenRulesReport.pdf.

OECD/IEA. Scenarios and projections, 2013. URL http://www.iea.org/publications/scenariosandprojections/.

William G. Pariseau. *Mechanical properties of intact rock and joints*. CRC Press/Balkema, Leiden, 2nd editio edition, 2011. ISBN 978-0415893398.

B. Park and K.-B. Min. Discrete Element Modeling of Transversely Isotropic Rock. In *47th US Rock Mechanics Symposium*, page 10, San Francisco, 2013. American Rock Mechanics Association.

Ken P.Chong, John Ward Smith, and Eric S. Borgman. Tensile Strengths of Colorado and Utah Oil Shales. *Journal of Energy*, 6(2):81–85, March 1982. ISSN 0146-0412. doi: 10.2514/3.62578. URL http://arc.aiaa.org/doi/abs/10.2514/3.62578.

Petroleum Seismology Network. Anisotropy and heterogeneity, 2013. URL http://petroleumseismology.systekproof.com/images/focus/101.

Dinh Quoc, Heinz Konietzky, and Martin Herbst. Brazilian tensile strength tests on some anisotropic rocks. *International Journal of Rock Mechanics & Mining Sciences*, 58:1–7, 2013.

Reuters. Hydraulic Fracturing (Fracking), 2012. URL http://blog.thomsonreuters.com/index.php/hydraulic-fracturing-fracking-graphic-of-the-day/.

C.D. Rokosh, J.G. Pawlowicz, H. Berhane, S.D.A. Anderson, and A.P. Beaton. What is Shale Gas ? An Introduction to Shale-Gas Geology in Alberta. Technical report, Energy Resources Conservation Board, Edmonton, 2009. URL http://www.ags.gov.ab.ca/publications/OFR/PDF/OFR_2008_08.pdf.

Rituparna Sarker and Mike Batzle. Anisotropic elastic moduli of the Mancos B ShaleâĂŘ An experimental study. January 2010. URL http://library.seg.org/doi/abs/10.1190/1.3513381.

A. Schiavi, G. Niccolini, P. Tarizzo, A. Carpinteri, G. Lacidogna, and A. Manuello. Acoustic Emissions at High and Low Frequencies During Compression Tests in Brittle Materials. *Strain*, 47:105–110, December 2011. ISSN 00392103. doi: 10.1111/j.1475-1305.2010.00745.x. URL http://doi.wiley.com/10.1111/j.1475-1305.2010.00745.xhttp://www.intechopen.com/books/effective-and-sustainable-hydraulic-fracturing.

SINTEF Petroleumsforskning AS. Speedy, 2013. URL http://www.sintef.no/home/SINTEF-Petroleum-Research/.

B. Van De. Steen, a. Vervoort, and J. a. L. Napier. Observed and simulated fracture pattern in diametrically loaded discs of rock material. *International Journal of Fracture*, 131(1):35–52, January 2005. ISSN 0376-9429. doi: 10.1007/s10704-004-3177-z. URL http://link.springer.com/10.1007/s10704-004-3177-z.

Jeffrey J. Swab, Jian Yu, Robert Gamble, and Steve Kilczewski. Analysis of the diametral compression method for determining the tensile strength of transparent magnesium aluminate spinel. *International Journal of Fracture*, 172(2):187–192, December 2011. ISSN 0376-9429. doi: 10.1007/s10704-011-9655-1. URL http://link.springer.com/10.1007/s10704-011-9655-1.

Abbass Tavallali and André Vervoort. Failure of Layered Sandstone under Brazilian Test Conditions: Effect of Micro-Scale Parameters on Macro-Scale Behaviour. *Rock Mechanics and Rock Engineering*, 43(5):641–653, February 2010. ISSN 0723-2632. doi: 10.1007/s00603-010-0084-7. URL http://www.springerlink.com/index/10.1007/s00603-010-0084-7.

The Handbrake Team. HandBrake, 2013. URL http://handbrake.fr/.

The MathWorks Inc. MATLAB, 2013. URL http://www.mathworks.se/.

Malin Torsaeter, Per Vullum, and Olav-Magnar Nes. Nanostructure vs. Macroscopic Properties of Mancos Shale. In *Proceedings of SPE Canadian Unconventional Resources Conference*. Society of Petroleum Engineers, October 2012. ISBN 9781613992470. doi: 10.2118/162737-MS. URL http://www.onepetro.org/mslib/servlet/onepetropreview?id=SPE-162737-MS\&soc=SPE.

F Toussaint, L Tabourot, and P Vacher. Experimental study with a Digital Image Correlation (DIC) method and numerical simulation of an anisotropic elastic-plastic commercially pure titanium. *Archives of Civil and Mechannical Engineering*, VIII(3):13, 2008. URL http://www.acme.pwr.wroc.pl/repository/215/online.pdf.

Catherine Trevethan. Global Shale Gas Basins, 2012. URL http://blog.thomsonreuters.com/index.php/global-shale-gas-basins-graphic-of-the-day/.

T.E. Unander. *Acoustic Emission Measurements in Petroleum-related Rock Mechanics*. Doktor ingeni{ø}ravhandling. Department of Petroleum Engineering and Applied Geophysics, Norwegian University of Science and Technology, 2002. ISBN 9788247154755.

U.S. Energy Information Administration. U.S. Natural Gas Wellhead Price, 2013. URL http://www.eia.gov/dnav/ng/hist/n9190us3a.htm.

P. Vacher, S. Dumoulin, F. Morestin, and S. Mguil-Touchal. Bidimensional strain measurement using digital images. *Proceedings of the Institution of Mechanical Engineers, Part C: Journal of Mechanical Engineering Science*, 213(8):811–817, August 1999. ISSN 0954-4062. doi: 10.1243/0954406991522428. URL http://pic.sagepub.com/lookup/doi/10.1243/0954406991522428.

A Vervoort, B Debecker, and A Tavallali. Fracturing of Transversely Isotropic Rock: An Experimental Study. In *The Southern African Inistitute of Mining and Metallurgy Southern Hemisphere International Rock Mechanics Symposium SHIRMS*, pages 17–32, 2012.

Vision Research. PCC. URL http://www.visionresearch.com/Service--Support/Downloads/Software/.

Barry N. Whittaker, Raghu N. Singh, and Gexin Sun. *Rock Fracture Mechanics: Principles, Design and Applications (Developments in Geotechnical Engineering)*. Elsevier Science Ltd, 1992. ISBN 0444896848.

T Yanagidani, O. Sano, M. Terada, and I. Ito. The observation of cracks propagating in diametrically-compressed rock discs. *International Journal of Rock Mechanics and Mining Sciences & Geomechanics Abstracts*, 15(5):225–235, October 1978. ISSN 01489062. doi: 10.1016/0148-9062(78)90955-5. URL http://linkinghub.elsevier.com/retrieve/pii/0148906278909555.

Younathan Youash. Geological Society of America Bulletin Tension Tests on Layered Rocks. (2), 1969. doi: 10.1130/0016-7606(1969)80.

Yong Yu, Jianmin Yin, and Zouwu Zhong. Shape effects in the Brazilian tensile strength test and a 3D FEM correction. *International Journal of Rock Mechanics and Mining Sciences*, 43(4):623–627, June 2006. ISSN 13651609. doi: 10.1016/j.ijrmms.2005.09.005. URL http://linkinghub.elsevier.com/retrieve/pii/S1365160905001383.

Z.Q. Yue, S. Chen, and L.G. Tham. Finite element modeling of geomaterials using digital image processing. *Computers and Geotechnics*, 30(5):375–397, July 2003. ISSN 0266352X. doi: 10.1016/S0266-352X(03)00015-6. URL `http://linkinghub.elsevier.com/retrieve/pii/S0266352X03000156`.